Quantitative Analysis of the Receptor-Induced Apoptotic Decision Network

by

Bree Beardsley Aldridge

B.S. Computer Engineering
B.S. Molecular and Cellular Biology
University of Arizona, 2002

SUBMITTED TO THE DEPARTMENT OF BIOLOGICAL ENGINEERING IN PARTIAL FULFILLMENT OF THE REQUIREMENTS FOR THE DEGREE OF

DOCTOR OF PHILOSOPHY IN BIOLOGICAL ENGINEERING

AT THE
MASSACHUSETTS INSTITUTE OF TECHNOLOGY

JUNE 2008

Author: _____
Department of Biological Engineering
May 19, 2008

Certified by: _____
Douglas A. Lauffenburger
Whitaker Professor of Biological Engineering, Chemical Engineering, and Biology
Thesis Supervisor

Certified by: _____
Peter K. Sorger
Professor of Biological Engineering (Massachusetts Institute of Technology)
and Professor of Systems Biology (Harvard Medical School)
Thesis Supervisor

Approved by: _____
Alan J. Grodzinsky
Chairman, Department Committee on Graduate Students

Thesis Committee

Accepted by: _____

Bruce Tidor
Professor of Biological Engineering and Computer Science
Thesis Committee Chairman

Accepted by: _____

Douglas A. Lauffenburger
Whitaker Professor of Biological Engineering, Chemical Engineering, and Biology
Thesis Supervisor

Accepted by: _____

Peter K. Sorger
Professor of Biological Engineering (Massachusetts Institute of Technology)
and Professor of Systems Biology (Harvard Medical School)
Thesis Supervisor

Accepted by: _____

Alexander van Oudenaarden
Professor of Physics
Thesis Committee Member

Quantitative Analysis of the Receptor-Induced Apoptotic Decision Network

by
Bree Beardsley Aldridge

Submitted to the Department of Biological Engineering on May 19, 2008 in Partial Fulfillment of the Requirements for the Degree of Doctor of Philosophy in Bioengineering

Abstract

Cells use a complex web of protein signaling pathways to interpret extracellular cues and decide and execute cell fates such as survival, apoptosis, differentiation, and proliferation. Cell decisions can be triggered by subtle, transient signals that are context specific, making them hard to study by conventional experimental methods. In this thesis, we use a systems approach combining quantitative experiments with computational modeling and analysis to understand the regulation of the survival-vs-death decision. A second goal of this thesis was to develop modeling and analysis methods that enable study of signals that are transient or at intermediate activation levels.

We addressed the challenge of balancing mechanistic detail and ease of interpretation in modeling by adapting fuzzy logic to analyze a previously published experimental dataset characterizing the dynamic behavior of kinase pathways governing apoptosis in human colon carcinoma cells. Simulations of our fuzzy logic model recapitulated most features of the data and generated several predictions involving pathway crosstalk and regulation. Fuzzy logic models are flexible, able to incorporate qualitative and noisy data, and powerful enough to generate not only quantitative predictions but also biological insights concerning operation of signaling networks.

To study transient signals in differential-equation based models, we employed direct Lyapunov exponents (DLEs) to identify phase-space domains of high sensitivity to initial conditions. These domains delineate regions exhibiting qualitatively different transient activities that would be indistinguishable using steady-state analysis but which correspond to different outcomes. We combine DLE analysis of a physicochemical model of receptor-mediated apoptosis with single cell data obtained by flow cytometry and FRET-based reporters in live-cell microscopy to classify conditions that alter the usage of two apoptosis pathways (Type I/II apoptosis). While it is generally thought that the control point for Type I/II occurs at the level of initiator caspase activation, we find that Type II cells can be converted to Type I by removal of XIAP, a regulator of effector caspases. Our study suggests that the classification of cells as Type I or II obscures a third variable category of cells that are highly sensitive to changes in the concentrations of key apoptotic network proteins.

Thesis Supervisor: Douglas A. Lauffenburger
Title: Professor of Biological Engineering, Chemical Engineering, and Biology

Thesis Supervisor: Peter K. Sorger
Title: Professor of Biological Engineering

Acknowledgements

I have been immensely lucky to have had the opportunity to complete this thesis in the company of fantastic friends and colleagues. I would especially like to thank my advisors, Doug Lauffenburger and Peter Sorger for giving me the opportunity to join their research groups, and especially for their support and advice during my graduate career. They have gently guided me while giving me freedom to pursue my favorite research topics – as a result, I have learned more than I expected along the way. I thank my committee members, Bruce Tidor and Alexander van Oudenaarden, who have also offered inspiration and useful research and career advice. I would also like to thank Suzanne Gaudet for her mentorship. Her positive outlook, keen scientific insights, and friendship have been invaluable to me.

The work presented in this thesis would not have possible without the help of labmates and collaborators. I would like to thank the members of the Sorger lab and the Cell Decision Process Center, and the DOE Computation Science Graduate Fellows for their help and advice. I would like to acknowledge John Burke, Debbie Flusberg, Suzanne Gaudet, Sabrina Spencer, and especially John Albeck (the "death" group in the Sorger lab) for establishing a creative and helpful working-group to quantitatively study apoptosis. I am grateful to have had the opportunity to work with George Haller and Robert Szalai on the dynamical systems and DLE analysis; Viji Draviam on developing new metrics to study kinetochores; Julio Saez-Rodriguez and Jeremy Muhlich on automatic fitting of logic models; Jaydeep Bardhan, Kevin Chu and Jacob White on model order reduction; and H. Steven Wiley on modeling methods to study signaling.

Finally, I would to thank my support network of family and friends. I am very grateful to be surrounded by BE classmates, many of whom have become very good friends and helped me through the trials and tribulations of both work and play. I would like to thank Reshma Shetty and Kathryn Loving for helping me study for the qualifying exams. I am also thankful for the ongoing support from my childhood friend Megan Boyle. I am thankful to have parents and parents-in-law, Brent and Deeporn Beardsley, and Don and Becky Aldridge, who have been so supportive. I would especially like to thank my husband John for his unwavering love and support, and his ongoing commitment to making sure that I am (outside) having fun.

Table of Contents

List of Figures and Tables

1 Introduction

1.1 Cell Decisions Determined by Receptor-induced Protein Signaling Networks

1.1.1 Introduction

Cells are confronted with changing environmental signals which they interpret to decide their own fate – to survive, die, proliferate, migrate, etc. Protein signaling networks transduce these extracellular cues, process these transient signals in the context of the current cell state, and effect a change in cell behavior. Because alteration to these signals can induce major changes in cell behavior leading to disease, many of these pathways are well studied. Despite the large body of research, a comprehensive understanding of how cells process signals to arrive at decisions has been elusive because of the complexity of these networks. This complexity arises because signaling networks are comprised of intertwined pathways that are each involved in several cell processes and exhibit cell-type and treatment-dependent behaviors. Understanding the cell decision process therefore requires a quantitative and multivariate study of the dynamic signaling response to cues. Mathematical modeling enables these data to be interpreted and evaluated in the context of the *a priori* knowledge about the pathways. This chapter introduces the molecular pathways involved in the death-vs-survival decision in mammalian cells and current mathematical techniques used to model these pathways.

1.1.2 Apoptosis

Apoptosis, or programmed cell death, is the process through which a cell methodically self destructs. This process is essential in multicellular organisms for development and maintenance of healthy tissues. The apoptotic decision is primarily mediated by two pathways that culminate in an irreversible activation of the caspase cascade. A key feature of apoptosis is the rapid "all-or-nothing" activation of the caspases, a family of cysteine proteases. Receptor-mediated apoptosis is typically characterized by activation of effector caspases which make a binary die-or-survive decision. The highly regulated signaling pathways involved in this cell decision process (survival versus apoptosis) are of particular interest because without regulation of the caspases, cells suffering from genomic instability may survive, potentially leading to oncogenesis. In cancer and autoimmune diseases, cells erroneously decide to survive; in degenerative diseases and immunodeficiencies, cells erroneously decide to die [1]. Apoptotic death is deliberate and characterized by altered membrane characteristics, nuclear condensation, blebbing of the membrane, cytoplasm shrinkage, endonucleolytic DNA cleavage, and blebbing of the membrane [2].

The intrinsic (or mitochondrial) pathway responds to stress and cues (such as DNA damage and starvation) and is regulated by the Bcl-2 family of proteins [3-5]. When triggered, the mitochondria outermembrane is permeabilized (MOMP), releasing a variety of proteins including cytochrome c, Smac/DIABLO, and AIF [6, 7]. Their release allows the formation of the apoptosome, a complex of procaspase-9, Apaf-1, and cytochrome c. The apoptosome converts the initiator caspase, caspase-9, to its active form [8].

The extrinsic, receptor-mediated pathway is initiated through activation of death-receptor family members (CD95/Fas, TRAIL-R, and TNF-R) by ligand-receptor complex formation [9-11]. Receptor activation causes formation of a death inducing signaling complex (DISC) which acts as a scaffold for procaspase-8, an initiator caspase, to autoactivate by induced proximity [12-14]. MOMP may be stimulated after DISC formation through truncation and activation of Bid by caspase-8. Positive feedback via caspase-6 amplifies caspase-8 and caspase-3 activity [15]. Cells have been classified as Type II if receptor-mediated apoptosis is dependent on MOMP and Type I if cell death is independent of the mitochondrial pathway [16].

Intrinsic and extrinsic pathways converge at the level of caspase-3 activation by the initiator caspases (-8 and -9) [17-20]. Caspase-3 is an effector capsase that executes the cell by cleaving hundreds of protein substrates such as PARP, lamins, and cytokeratin. Caspase-3 is primarily inhibited by XIAP which acts by binding to active caspase-3, preventing it from binding its substrates. In addition, XIAP is an ubiquitin ligase which is thought to tag active caspase-3 for proteasome-mediated degradation, another mechanism by which XIAP reduces caspase-3 activity. Once released from mitochondira, Smac/DIABLO binds XIAP, thereby releasing XIAPs inhibition of caspase-3 shortly after MOMP. Both instrinsic and extrinsic pathways also share several upstream control mechanisms by kinases such as Akt, ERK, JNK, and IKK [21-35].

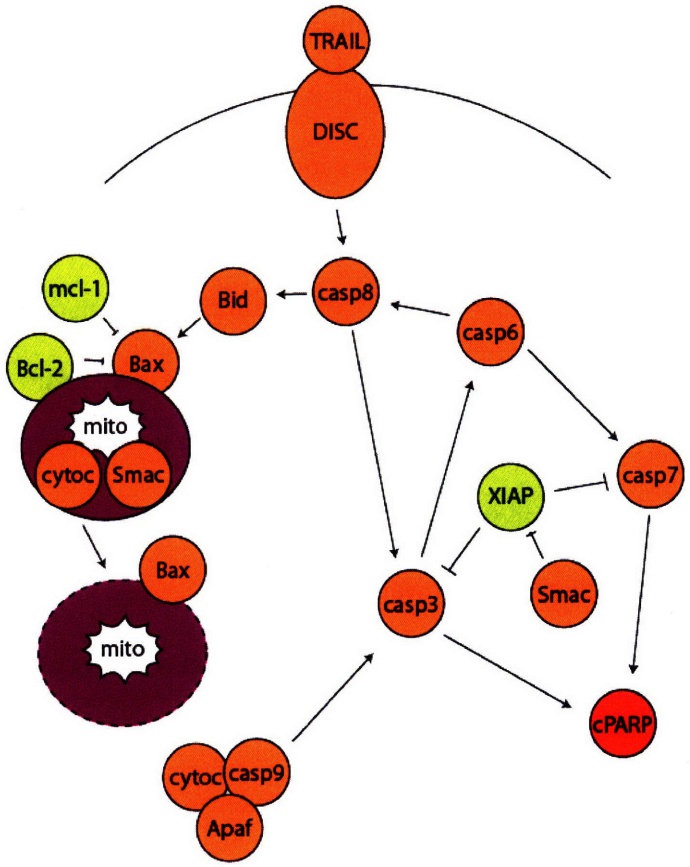

Figure 1-1 Apoptosis signaling pathway
Two pathways control the activation of the caspases. The intrinsic pathway is mediated by the Bcl-2 family of proteins including Bcl-2, Mcl-1, Bid, and Bax. The Bcl-2 proteins mediate mitochondrial outermembrane permeabilization (MOMP) and subsequent release of cytochrome c and Smac. The extrinsic pathway triggers DISC assembly and caspase-8 activation, leading to the activation of caspase-3 which is held in check by XIAP.

1.1.3 Survival

In addition to cellular stresses and death-ligands, the apoptotic decision is influenced by pro-survival signals stimulated by cytokines such as insulin, IGF, TNF, and EGF. Several kinase pathways play a central role in transducing signals from these cytokines. Binding of the ligands to receptor tyrosine kinases induces adaptor proteins such as IRS-1 to effect transient signaling through the canonical ERK, JNK, IKK, p38, and Akt pathways (Figure 2-1). Significant crosstalk among these pathways motivates the use of modeling to unify conflicting responses in different cell types to their activities

The most well studied of these is the ERK pathway. ERK is a MAPK, the last member of a cascade of three kinases. Growth factors and mitogens (EGF and insulin, for example) lead to activation of a MAPKKK (Raf) after binding to small GTP-binding proteins. The MAPKKK phosphorylates and activates a MAPKK, MEK, which subsequently phosphorylates ERK. Once phosphorylated and active, ERK phosphorylates many substrates including several MKs (MAPK-activated protein kinases) and transcription factors to promote proliferation and survival [36].

Other MAPKs, p38 and JNK are triggered by stress and cytokines (such as TNF). Like ERK, p38 and JNK are well studied and have numerous roles in cell decisions [36]. The role of JNK in affecting apoptosis has been debated in the literature – some groups report that JNK is a pro-apoptotic factor while other report the opposite [37]. These conflicting reports suggest that JNK's role is highly context specific and motivates a quantitative, systems-level analysis of these intersecting pathways.

The Akt pathway is strongly induced by prosurvival cytokines, particularly insulin and IGF, which act through IRS-1 [38-40]. Akt is a serine/threonine kinase whose activity is regulated by PI3-kinase (PI3-k). Akt interacts with many signaling pathways including those regulating IKK, JNK, mTOR, FKHR, and ERK to control both cellular metabolism and survival. Though controversial, Akt may also exert anti-apoptotic influence by phosphorylating Bad, thus blocking its ability to competitively bind pro-survival Bcl-2 and Bcl-xL [41].

IKK activation is strongly induced by TNF and DNA damage. When active, IKK phosphorylates IKB. In the phosphorylated state, IKB is tagged for ubiquitination and subsequent degradation, releasing NF-kB which it normally binds and sequesters in the

cytoplasm, and enabling it to relocate to the nucleus [42]. NF-kB is a transcription factor that is both pro-inflammatory and pro-survival; it induces changes in gene expression for key proteins such as the anti-apoptotic factor XIAP.

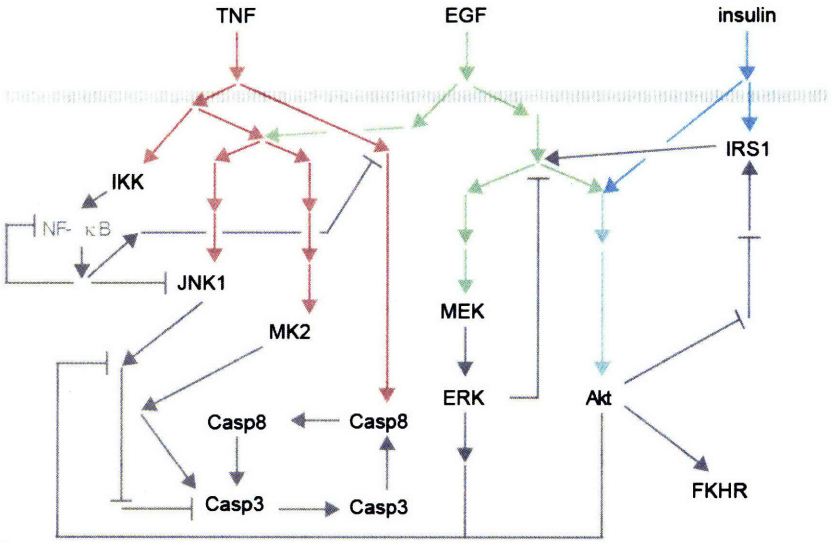

Figure 1-2 Pro-survival signaling pathway
Cytokines such as TNF, EGF, and insulin stimulate the activation of pro-survival (and pro-apoptotic) pathways. These pathways are highly interconnected making it difficult to delineate the role of each pathway in the death-vs-survival decision. This diagram was adapted from [43].

1.2 Modeling/analysis approaches and challenges[1]

1.2.1 Introduction

Molecular, cellular and developmental biology seek to describe physiological processes in terms of biochemical pathways and molecular mechanism. Medicine and drug discovery add the practical goals of understanding disease and developing therapies. Molecular biology has been dominated by attempts to identify key gene products, characterize their loss-of-function phenotypes, and determine their biochemical activities. Genomics does not in and of itself spell an end to this "component identification" phase of modern biology, but the sheer size of the cellular parts list emphasizes the need to

[1] This section contains excerpts and figures from 44. Aldridge, B.B., et al., *Physicochemical modelling of cell signalling pathways.* Nat Cell Biol, 2006. **8**(11): p. 1195-203.

understand genes, disease and pharmaceutical agents quantitatively in terms of pathways and circuits. Much has been written about the limitations of "common sense thinking" as a means to understand the complexity of biological pathways and about the need for integrative approaches such as mathematical modeling [45]. Modeling that builds on empirical data to construct chemically and physically realistic representations of biological pathways has the ability to elucidate molecular and system-wide mechanism, systematize diverse experimental data and generate specific, testable hypothesis.

1.2.2 Physicochemical modeling

Physicochemical modeling combines prior knowledge about cell signaling and regulatory pathways with fundamental principles derived from chemistry and physics to create a powerful tool for formalizing and extending traditional approaches to molecular biology approaches. Physicochemical modeling is a natural counterpart to molecular experimentation and is an extension of the current practice of drawing pathway maps, albeit one with much greater rigor and power. Accurate physicochemical models of cellular pathways aim to explain molecular mechanism in the context of upstream and downstream regulators, reveal pathway design principals and serve as dynamic repositories of data and knowledge.

Physicochemical modeling seeks to describe properties such as covalent modification, intermolecular association, and intracellular localizations, of biomolecules in terms of equations derived from established physical and chemical theory [46-50]. The power of physicochemical modeling lies in its ability to encapsulate prior knowledge and make specific predictions. Physicochemical modeling works best with pathways in which components and connectivity are relatively well established. When prior knowledge is

sparse, data-driven statistical models are generally more appropriate [51]. Equations in physicochemical models refer to identifiable entities and parameters have chemical meaning (concentration, binding affinity, rate of reaction etc). A physicochemical model can therefore be viewed as a mathematical translation of a pathway map, and, thus, as a logical extension of current practice. Moreover, adoption of recently developed schematic standards for pathway mapping should help the translation process [52].

The correct mathematical form for a physicochemical model depends on the properties of the system under study and the goals of the modeling effort. Ordinary and partial differential equations (ODEs and PDEs) are used most commonly and both can be cast in either deterministic or stochastic forms. Deterministic differential equations are continuous in time (or time and space) whereas stochastic differential equations are discrete and include effects arising from random fluctuation around the mean behavior. Currently, the most common means of representing biochemical pathways is via a set of coupled deterministic ODEs. Coupled sets of ODEs (ODE networks) cast mass action kinetics in terms of the rates of production and consumption of individual biomolecular species ($d[X_i]/dt$). Provided that reasonable values for the initial concentrations of species can be obtained (the initial conditions), time integration of ODEs yields the concentrations of each species at any subsequent point in time, thereby facilitating comparison of the model to experimental data. ODE networks are amenable to a wide variety of analytic techniques, some of which are difficult if not impossible with more complex mathematical forms.

In an ODE network, each biochemical transformation is an elementary reaction with forward and reverse rate constants (Figure 1-3). Changes in localization, a central

feature of biological pathways, are represented by compartmentalization. Each species is allowed to inhabit one or more compartments and to move among the compartments via elementary reactions. Compartments are also used to represent assembly of macromolecular complexes and other changes of state not usually associated with enzymatic action. Two fundamental assumptions of the compartmentalized ODE formalism are that, within a compartment, the concentration of each species is high and uniform such that transport is essentially instantaneous (that is, the compartment is well-mixed). Between compartments, transport is slower and is therefore associated with an observable rate. If these assumptions are not satisfied, then it is necessary to model explicitly changes in species concentrations with respect to space (typically using PDEs).

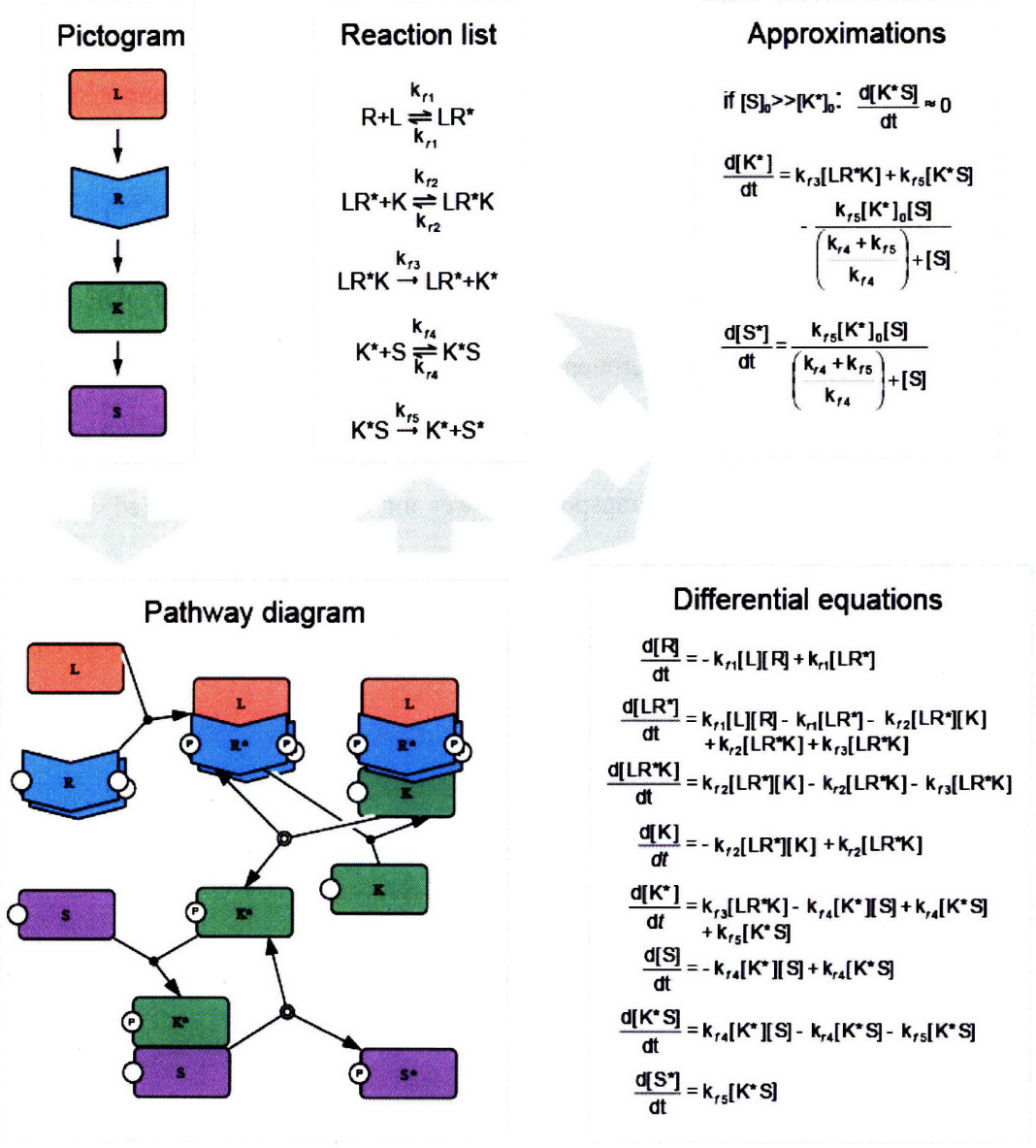

Figure 1-3 Steps in physicochemical modeling

Current Practice – Pictograms: A pictogram is a highly abstracted representation depicting components of a pathway and their interaction. Here, a simple linear Ligand-Receptor-Kinase-Substrate pathway is depicted. While the pictogram nicely conveys the general information flow in the network, mechanistic details required for mathematical modeling is absent.

Formal Pathway Diagram: A pathway diagram drawn with CellDesigner details the reaction network [53]. Instead of representing the kinase as one object (as in the pictogram), each form of the kinase, either in complex or alone, must be depicted (K, K*, LR*K, and K*S). A key challenge in developing a pathway diagram is making choices about granularity in species and reactions. In this example, the receptor is a dimer and each subunit has two phosphorylation sites, yielding 64 possible ligand-receptor dimer complexes. However, this complexity is represented simply by two species: non-active and unphosphorylated (R) and ligand-bound, fully phosphorylated (LR*). It should be noted that approaches such as rules-based modeling may be preferred to the use of pathway diagrams (see text for details)

Reaction List: A complete list of reactions is generated based from the pathway diagram. This list can be automatically produced with several specialized software tools [54]. For reversible reactions, both forward and backward rate constants must be indicated.
Differential Equations: From the list of reactions, a system of differential equations can be enumerated using appropriate rate laws. A highly effective basis for rate laws is mass-action kinetics, which uses the product of a rate constant and the concentrations of the reactants to calculate the rate of formation of product and elimination of reactants (in the continuum approximation).
Simplifying Assumptions: Simplifying assumptions can be made to reduce the complexity or size of a model. The Michaelis-Menten approximation to enzyme-substrate kinetics is often applied. This particular rate form assumes rapid equilibrium of an intermediate complex (K*S), so a quasi-steady-state approximation is imposed (d[K*S]/dt=0), thus reducing the number of species in the model. Because this is an approximation to mass-action kinetics, its use can alter model behavior, particularly when the intermediate complex does not reach equilibrium or the reaction is tightly coupled to other processes [55-57].

1.2.3 Graph-based modeling

Mechanistic, ODE-based models cannot be used when the knowledge describing molecular mechanisms are not well defined. Instead, other modeling techniques ranging from projection methods to statistical and logic-based models may be applied. These methods, while more abstract than physicochemical modeling, can be well-suited for straightforward interpretation and incorporation of granular data. The choice of modeling method depends on the level of quantitation of the experiment data, prior knowledge of the pathways under study, and types of questions posed. Data projection methods such as principal component analysis (PCA) and partial least-squares regression (PLSR) are the most abstract and are especially useful for linking signaling factors to different cell responses. These methods cannot incorporate prior knowledge about the signaling pathways, except for helping the modeler design which signaling metric (normalization, integration, peak intensity, etc) to include in the analysis. A recent set of studies using PCA and PLSR modeling on a data-compendium detailing the signaling and apoptotic response the EGF, TNF, and insulin in human colon carcinoma cells has established standards for data normalization and identified novel autocrine and pro-survival signaling events [43, 58, 59].

Graph-based models using Bayesian and Boolean logic networks have been used to quantify signaling species interactions to each other and to phenotypic response [60, 61]. Bayesian networks and dynamic Bayesian networks (Markov models) are used as a reverse engineering approach to quantify the strength of influence among signals using Bayesian statistics. These models have the advantage that they can be easily derived from data to identify candidate network topologies, though this process requires a dataset rich in perturbations to individual network species. Because Bayesian models are constrained to be acyclic, a major disadvantage of these models is their inability to encode positive and negative feedback. To find cycles, it may be possible to compile an ensemble of high-ranking acyclic models.

Like Bayesian networks, Boolean logic models use an edge-node graph representation where each edge carries signals to nodes, which specify the activity or concentration of a network species given the state of the input signals. In Boolean logic, signals are classified as being either low or high (at edges) and logic gates define the interactions between the input and output signals (at nodes). Because these rules can be written as if-else statements, they are intuitive to read and write, making logic-based methodology attractive for modeling protein signaling networks, which are often depicted as graphs with arrows marked as being either activating or inhibitory. Due to the simplified formalism, Boolean logic models can be built gradually and can therefore incorporate a priori knowledge, hypothesis, and experimental data about network topology and species interactions. Logic-based models are simple to build, manipulate, and interpret, making them appealing because they don't require specific computational or mathematical skills. However, these advantages are counter-balanced by the abstract

representations of molecular interactions and dynamics in signaling as compared to physicochemical modeling. Both Boolean logic and Bayesian models discretize biological information (protein concentration, state, or activity) which is often inherently continuous. Using multi-step discretization may mitigate the loss of information from a two-step discretization, and their ability to capture dynamic and intermediate signaling events as compared to continuous methods has yet to be comprehensively addressed.

1.3 Challenges in combining models and experiments[2]

1.3.1 Introduction

To quantitatively understand signaling networks, an iterative approach of mathematical modeling and experimental measurement is required [62]. It remains challenging to construct models that represent real biological pathways and to establish rigorous links between models and experimental data: in many cases, the underlying experimental data are simply too incomplete. Current challenges in building pathway models include more efficient and transparent ways to summarize prior knowledge, fit parameters, specify model structure, and analyze models.

1.3.2 Model construction

The construction and calibration of biochemical pathway models will continue to generate controversy among both physical scientists and traditional molecular biologists. It is often presumed that complex models have sufficient degrees of freedom to fit any piece of data. In the oft-misquoted perspective of Gauss "Give me four parameters, and I

[2] This section contains excerpts and figures from 44. Aldridge, B.B., et al., *Physicochemical modelling of cell signalling pathways.* Nat Cell Biol, 2006. **8**(11): p. 1195-203.

will draw an elephant for you; with five I will have him raise and lower his trunk and his tail" [63]. Clearly models should be formulated with as few species and free parameters as possible. However, if model granularity is too low to make predictions at the level of individual gene products, molecular biology, pharmacology, and genetics are less useful in model verification. Pathway models in biology therefore represent a compromise between excessive complexity and too many degrees of freedom and excessive simplification and loss of mechanistic insight. As with mesoscale engineering models, biological models are likely to become hybrids with varying levels of detail. This will most likely involve a merger of differential equations with logic based approaches.

Assuming that a model with correct components and connectivity has been constructed, the next critical step is determining the values of variables including rate constants and initial conditions (concentrations at time=0). Variables can be measured directly (or obtained from the literature) particularly in the case of protein and mRNA concentrations. Rate constants can also be measured in vitro, although it is often unclear how these rates compare to rates in cells. It is common however, for many parameters in biological models to remain unmeasured and to therefore require estimation. This is accomplished by fitting the model to data in via regression. That is, even if the value of particular parameter cannot be measured directly or, derived independently it can be estimated by computing the range of values over which the model most closely matches experimental observation, given uncertainty in the data.

The difficulty and reliability of model regression is closely tied to the number of free parameters and to the amount and quality of training data. Models of intracellular pathways typically have large numbers of free parameters that must be estimated using

noisy, incomplete data. In the noise-free case, $2n+1$ observations are needed to estimate n parameters in an ODE model, but the presence of noise makes regression more complex [64]. Regression with noisy data proceeds via a series of statistical tests whose power is proportional to the amount of data and inversely proportional to the noise. For each parameter, model calibration has the potential to yield correct values, incorrect values and weakly determined values. By weakly determined we mean that the variable can take on a wide range of values without altering the goodness of fit to observation. In these cases, it is often assumed that the model is "robust" to changes in the parameter. However, parameters in large models can be tightly coupled so that uncertainly in some parameters can affect all parameters. Thus, unconstrained parameters are correctly regarded as ones about which modeling and experiment provide little insight.

Two critical decisions in the design of models are specifying the scope and level of detail. As a practical matter, models must concentrate on a small subset of the totality of reactions that take place in a cell (Figure 1-3). Thus, assumptions must be made about the extent to which species included in the model evolve independently from species excluded from the model. The issue of model scope is usually cast in terms of modules – subsets of cellular reactions assumed to work together in the execution of discrete physiological functions [65]. Models published to date are relatively limited in scope and their size is typically set by prior practice in the field or by the availability of experimental reagents. Little exists in the way of rigorous theoretical or empirical evidence for modularity in cell signaling pathways, but it is an assumption implicit in all molecular approaches, not just physicochemical modeling. Indeed, uncertainty as to the components, connectivity and properties of a pathway is a key motivation for undertaking

rigorous, quantitative modeling. For the foreseeable future *ad hoc* assumptions are likely to determine the scope of most models. However, as models grow in complexity and size, and as understanding of network architecture increases, we can expect much greater insight into modularity.

A second design decision in assembling a model is the degree of detail (that is, model granularity). It is not possible to derive the functional properties of proteins and other biomolecules directly from their chemical structures and pathway models are therefore not detailed molecule-level representations. Conversely, relatively little insight is obtained when molecular processes are lumped together to produce few species and equations. Physicochemical modeling, for example, aims to make experimentally testable predictions at the levels of genes and proteins, and this therefore determines their granularity. Pathway models are therefore mesoscale models in which the number of species is similar to the number of unique gene products.

The correct granularity for pathway models is complicated by the fact that proteins assemble into large multi-component complexes, undergo extensive post-translational modification and partition among multiple cellular compartments. If these processes are to be represented in a model, the number of species increases dramatically relative to the number of gene products. In the case of the epidermal growth factor receptor (EGFR), a membrane-bound receptor tyrosine kinase that forms dimers with one of three other family members, 276 distinct homodimeric species can arise from three binding partners and two phospho-forms ([66]; actually EGFR has more than eight binding partners and ten phosphorylation sites, 10). The "combinatorial explosion" in biochemical species relative to gene products represents a formidable problem for model

generation and analysis, topics that have recently been discussed in detail [67]. It is therefore common to limit models to a subset of possible species. If data are available demonstrating the equivalence of biochemical forms then lumping them together is clearly warranted. Similarly, if assembly or multi-site modification is rapid and processive, then intermediate states can be ignored. In some situations, including EGFR signaling, the significance of different biochemical states is not known and the level of detail that yields the most accurate model remains unknown.

The multiplicity of biochemical species arising from processes such as receptor activation argues in favor of models with many species. However, the larger the number of species and free parameters, the greater the arbitrary adjustability of a model, and the greater the chance that parameters will be indeterminable. In the absence of countervailing evidence, the best model is the one that is most parsimonious in species and parameters. Thus, a balance must be struck between too few species and insufficient molecular detail and too many species and model indeterminability. Even in highly granular physicochemical models it is rarely necessary to include detailed representations of core metabolic and synthetic processes such as protein synthesis, energy production, gene transcription etc. Instead, these processes can be introduced as simplified "lumped" rates. Metabolic and synthetic processes are themselves being subjected to quantitative modeling and hybrid models will therefore develop in which biological processes are alternately modeled in detail or in aggregate. For example, a highly simplified "lumped rate" representation of a detailed synthesis model could be embedded in a physicochemical model of signal transduction to yield a hybrid. Realistic regulation could be reproduced by including an adjustable parameter in the lumped reaction that makes

translation dependent on signal levels; in the hybrid model, it is not necessary to include the synthesis model in its entirety.

The issue of model granularity also arises in formulating equations that represent elementary reactions. For example when a reaction is very fast as compared to other reactions (by a factor of $\geq$100x), it can be assumed that the fast process operates in quasi-equilibrium. A combination of fast processes can also be assumed to operate at quasi-steady-state. Differential equations can then be substituted by time-independent algebraic relations [68, 69]. The result is a model with fewer species, equations and parameters but more complex rate terms. A specific and common example of algebraic substitution is replacement of mass-action kinetics with Michaelis-Menten kinetics. In this case, differential equations representing enzyme-substrate intermediates are substituted by differential algebraic equations slightly more complex than an ODE in mathematical form but with fewer free parameters (Figure 1-3). A second example of algebraic substitution involves representing a series of reactions as a "transfer function" in which inputs (such as the concentrations of substrates) are translated into outputs (rate of formation of a product) via an assumed or fitted algebraic function. A common example of a biological transfer function is a Hill function (itself derived from the Michaelis-Menten equation), which captures the cooperative behavior of an enzyme cascade or protein multimerizatioin in a single exponential function with an adjustable Hill coefficient [46, 70]. Substitution of ODEs by transfer functions and other algebraic terms constitutes a very simple example of model order reduction [71]. However, in all model order reductions it is important to ascertain whether the implied assumptions are valid. It is not always appreciated, for example, that Michaelis-Menten kinetics represents a

simplification of mass action kinetics valid in the quasi-steady-state, but not necessarily in the case of rapidly evolving reactions. [55-57].

Once a preliminary model has been constructed it must be subjected to verification, calibration and validation. Verification is the process of determining how accurately prior knowledge and underlying assumptions have been translated into mathematical form (that is, whether the model structure is correct [72, 73]). Calibration (also known as regression or training) is the process by which parameters in a model are estimated so that the model matches experimental data. Finally, model validation is the process of evaluating the match between model performance and the primary design goal. In the case of biological models, this is usually a close match between model and experimental data. Robustness and bistability are sometimes introduced as additional validation criteria; but their relevance as general constraints on model behavior is not clear.

Most physicochemical models, particularly those of eukaryotic networks, await rigorous regression, and parameter values are therefore largely unconstrained. A useful starting assumption is to set parameter values within physically plausible ranges and conservative catalytic rates, which for physicochemical models are $k_f \sim 10^{-6}$ (number/cell)$^{-1}$ sec^{-1}, $k_r \sim 10^{-2}$ to 10^{-3} sec^{-1}, $k_{cat} \sim 1\text{-}10$ sec^{-1}, K_d (for complexes) $\sim 10^{-8}$ M and concentrations in the range of 10^3 to 10^6 molecules per 10^{-12} L cell. Uncalibrated or partly calibrated models are useful for simulating results but definitive conclusions cannot be drawn about the rates of specific reactions. In addition, different models, or models with the same structures but regressed against different sets of data, cannot be rigorously compared. The quality of calibration is also related to the issue of model uniqueness. That

is, is a particular model structure and set of parameter values the only way to model the data? Unfortunately this is typically a very difficult question to answer conclusively [62]. The extent to which incomplete calibration is a serious issue depends critically on the hypotheses one hopes to derive from the model.

1.3.3 Model Analysis

Physicochemical models of biological pathways are attractive because the mathematics provides a means to merge prior knowledge with experimental data and underlying physical principles. Pathway models make it possible to examine in detail the effects of protein dysregulation and pharmacological intervention. Formal analysis of pathways should also help to uncover design features and common motifs as well as reveal the extent to which pathways are truly modular. An additional, and less appreciated aspect of models is their ability to serve as transmittable repositories of knowledge.

Once model structure is set and initial conditions and rates have been determined or estimated, mathematical exploration and analysis can begin. Simulation is a simple but powerful tool for exploring network behavior and for guiding experimental verification. With little effort, time-dependent concentrations of key species can be compared over a range of protein concentrations, network topologies, and rate parameters. To simulate the effects of RNAi, for example, a model is run with new, experimentally-derived, concentrations for the depleted protein. To simulate the effects of a kinase inhibitor, the catalytic rate constant or level of bound ATP are reduced. In each case, simulated data can be compared to data such as flow-cytometry, quantitative Western blotting and time-lapse microscopy. For example, six models with different

structures for Mdm2-p53 interaction were recently compared to live-cell imaging data so as to select the best model [74]. An interesting aspect of this work was the inclusion of experimental noise in the simulated data so as to facilitate comparison to real data.

Sensitivity analysis is a powerful method for systematically determining which concentrations and rate constants (or other parameters) in a model influence overall behavior (Figure 1-4). Insensitivity of a model to parameter variation has been equated with robustness, but robustness is probably better defined with respect to the sensitivity of network behavior to noise, either in the experimental data or in stochastic reactions (in product engineering, robustness in design involves searching the space of adjustable parameters for values that minimize the influence of noise system behavior [75]; Figure 1-4). Both the objective functions (such as maximum integrated output, rate of change of output etc) and the set of variables over which the sensitivity analysis is performed can be defined, as can the range of values to be evaluated. Because the objective function is typically sensitive to changes in multiple parameters, multidimensional sensitivity analysis is the preferred approach [44, 76, 77]. Sensitivity is often visualized as a landscape of "hills" and "valleys" representing areas of parameter space in which small changes have a significant effect on behavior. In addition to revealing key parameters in a network, sensitivity analysis is valuable in ascertaining which parameters should be the focus of direct measurement or where perturbations of the system will be most informative.

A second approach to analyzing physicochemical models is qualitative and based on determining the classes of behavior it can produce, such as bistability, oscillation etc. Sets of differential equations can be solved for their stable and unstable steady states (that

is, sets of parameter values at which the model does or does not return to the steady state upon perturbation) by setting the rate of change to zero (representing the steady state). Bifurcation analysis makes it possible to determine whether different trajectories through parameter space lead to different qualitative behaviors about the steady-state. However, in the case of transient processes typical of cell signaling and regulatory pathways, techniques from dynamical systems theory need to be adapted to physicochemical models. These methods will need to determine, without looking at steady-state behavior, how the output of a model will change over time (or time and space) when initial conditions or parameter values change.

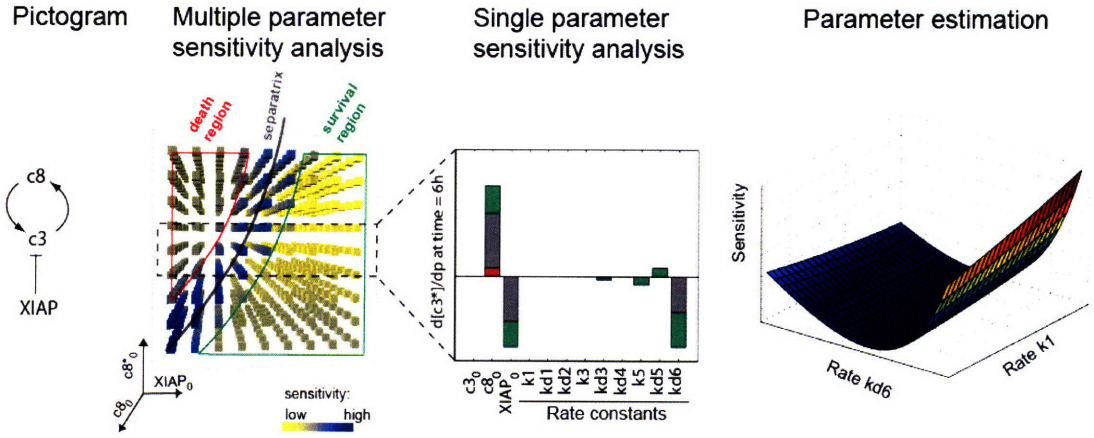

Figure 1-4 Sensitivity analysis and parameter estimation
Parameter estimation: Parameter estimation uses an objective function to optimize parameter sets, with the goal of fitting model to data. The results of parameter estimation are context specific (dependent on time, the parameters of the model, and the objective function) and many methods exist (such as Monte Carlo simulations) to ensure that the estimation does not end in a local minimum of the objective function [78]. The shape of minimum is reflection of parameter sensitivity – long, thin valleys are sensitive to some, but not all parameters.
Sensitivity analysis: The relative importance of the various network species and reactions can be investigated by using sensitivity analysis. This analysis is frequently performed in terms of individual parameter (rate constants or initial concentrations) changes. However, sensitivity is context-specific, and calculating sensitivity while multiple parameter change simultaneously provides a more global view of network behavior. A challenge lies in choosing appropriate objective function and parameters for evaluation analyze. Typically, a sensitivity objective function is d[one parameter]/d[another parameter] evaluated at a finite time, or integrated over time.
As one example, consider the last step in the apoptosis decision network: prolonged activation of caspase-3 (c3) resulting in degradation of key cellular components. In receptor-mediated apoptosis, caspase-8 is activated by a death receptor. Positive feedback is achieved by a caspase cascade (caspase-8 (c8) and caspase-3 activating each other). Caspase-3 activation (c3*) is inhibited by binding and ubiquitination by

X-linked inhibitor of apoptosis (XIAP). This small pathway and model is specified in detail in Chapter 3 and [77]. Parameter estimation can help identify the best fit parameters according to an objective function (f_{obj}), such as the least squared difference between the model and experimental data. As with sensitivity analysis, parameter estimation can elucidate which parameters should be measured experimentally (here, more care is required in measuring k_{d6} than k_1). Multiple parameter sensitivity (illustrated here as finite-time Lyapunov exponents, see Chapter 2) is highest in the phase-space region separating life or death signals – accordingly, this region (blue) is called a separatrix (see Chapter 3). We observe that the separatrix is invariant to the initial amount of inactive caspase-8, but not the active form or XIAP. The critical amount of caspase-8 or XIAP needed to alter behavior is dependent on the initial conditions of the other network species. Individual parameter sensitivity analysis was performed from three different locales of phase-space: low, medium, and high initial concentrations of XIAP (red, gray, and green, respectively). Sensitivity is measured as d[active c3]/d[parameter] at six hours after simulating a spike of caspase-8 activation. The system is most sensitive to caspase-8, XIAP, and the rate constant involved in the ubiquitination of caspase-3 by XIAP. As expected, single parameter sensitivity is most remarkable when calculated at a medium level of XIAP, lying on the separatrix.

1.4 Thesis Aims

This thesis focuses on combining mathematical modeling and experimental data to better understand how cancer cells arrive at a cell death decision. My particular interest was in developing new modeling and analysis methodologies that help us more effectively derive new understanding from experimental data and also drive the design of new experiments. Chapter 2 describes an improvement to discrete, logic-based modeling methods by using fuzzy logic to model a dataset characterizing the signaling response to conflicting pro-death and pro-survival cytokines. Chapters 3 and 4 focus on the apoptotic decision in the context of a single death ligand. In Chapter 3, a novel analysis methodology is described to analyze transient signaling in physicochemical modeling. It is based on direct Lyapunov exponents and applied to a small model describing caspase-3 activation. In Chapter 4, a model of TRAIL-induced apoptosis is analyzed using Lyapunov exponents with the goal of characterizing conditions leading to Type I vs Type II apoptosis. The analysis predicts that the ratio of XIAP to caspase-3 can influence which pathway is used in the apoptotic decision; we confirm this hypothesis experimentally.

2 Fuzzy Logic Analysis of Pathway Crosstalk in TNF/EGF/Insulin Signaling

2.1 Introduction

A variety of modeling methods can be applied to understanding protein signaling networks and the links between signals and phenotypes [51]. The choice of modeling method depends on the questions being posed (e.g. mechanistic or phenotypic), the quality and type of experimental data (quantitative or qualitative), and the state of prior knowledge about the network (interaction map or detailed biochemical pathway; Figure 2-1). Abstract techniques are largely data-driven and aim to discover correlations among signals and between signals and cellular phenotypes [51]; these methods include principal component analysis (PCA) and partial least-squares regression (PLSR). Differential equation-based models, in contrast, are highly specified and dependent on extensive prior knowledge of components and their interactions, but have the advantage that they capture temporal and spatial dynamics at the level of individual reactions [44]. Between these extremes, modeling methods such as Bayesian statistics, hidden Markov models, and logic-based models have been used to construct graph-based representations of influences and dependencies among signals and phenotypes based on experimental data [60, 79-83]. An advantage of these methods is their applicability to situations in which mechanistic information is incomplete or fragmentary but the notion of a pathway or network of interacting species nonetheless informative. Moreover, logic-based models use natural language to encode common logical statements such as "if the kinase is not active or the phosphatase is overexpressed, the substrate is not phosphorylated". Logic-based models

are commonly depicted as edge-node graphs in which interactions among species occur at nodes, with gates specifying the logic of the interactions based on a set of specified rules. The identities of the gates are typically determined based on prior knowledge or experimental observables and the input-output relationships of each gate inferred from experimental data [61, 82-87].

Among logic-based methods, Boolean modeling is the most common. For example, a discrete-state representation of the phosphorylation of insulin receptor substrate 1 (IRS-1) at serine 636 (IRS(S)) might use three input edges for time, TNF and EGF (see below), one output edge for IRS(S), and one logic gate (Figure 2-2A). In Boolean logic, the interactions among these inputs involves a combination of elementary "AND", "OR", and "NOT" gates that connect to create logic such as "(EGF OR TNF) AND (NOT(time))" that is most conveniently specified by truth tables (Figure 2-2B-C). Truth tables consist of lookup values for the outputs (consequent value) based on all possible combinations of input values (antecedents; 1 for on and 0 for off). Despite the appeal of Boolean models as a simple way to encode interactions among species, the two-state "on-off" representation of biological signals is unrealistic [88]. In this chapter we propose fuzzy logic (FL) as an approach to logic-based modeling with the simplicity of Boolean approaches but with several significant advantages [89], among which the ability to encode intermediate values for inputs and outputs is the most important. FL can encode probabilistic and dynamic transitions between network states so as to create realistic and easy to understand depictions of cell signaling networks [61, 85-87, 90-92].

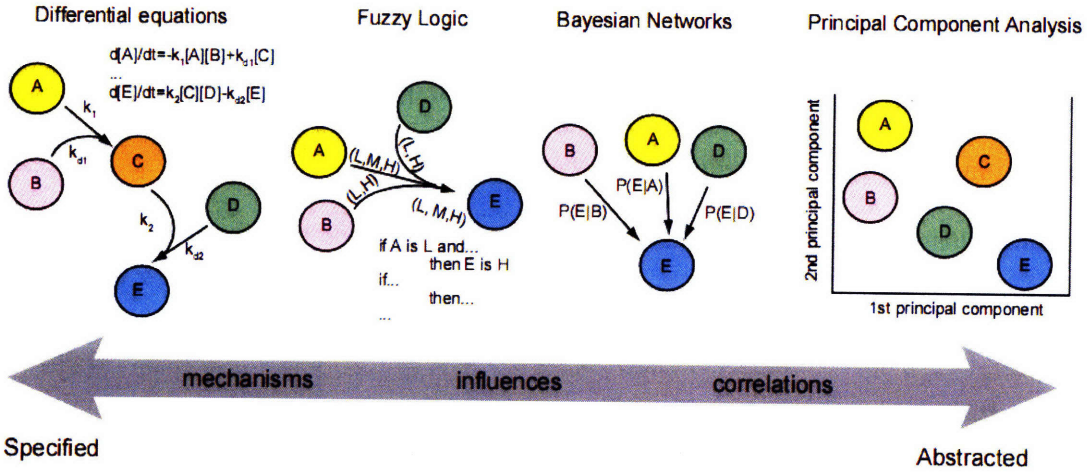

Figure 2-1 Spectrum of modeling methods
Modeling techniques balance specificity and complexity. Principal component analysis elucidates correlations among network components (A-E) by a linear transformation of the data, resulting in orthogonal principal components. Bayesian networks use conditional probabilities to associate correlations and influences between network components. Fuzzy logic uses rule-based gates and probabilistic representation of input variables to quantify influences and mechanism that regulate network species. Differential-equations models using mass-action kinetics are highly specified defining regulatory mechanism by defining rates of change in network species concentrations.

The death-survival decisions in mammalian cells that are examined in this chapter are mediated by the joint action of multiple receptor-dependent and cell-intrinsic processes that coordinate opposing pro- and anti-apoptotic signals. We have previously described a "cue-signal-response" (CSR) compendium of protein signals and phenotypic responses in HT-29 human colon carcinoma cells treated with combinations of tumor necrosis factor-α (TNF), epidermal growth factor (EGF), and insulin [58]. The compendium includes ten measurements of protein modification states (phosphorylation and cleavage) and kinase activities for four proteins downstream of TNF, EGF and insulin receptors collected over a 24 hr time period in biological triplicate (see Figure 2-4A and Figure 2-5A). To date we have used PLSR to predict the phenotypic consequence of perturbing the signaling network [43] and PCA to identify autocrine feedback circuits [59]. Here we ask whether the application of FL to this data can

accurately encode important aspects of network dynamics. We also compare FL and Boolean models directly and observe a superior fit by the former to data. Finally, we use our FL model to generate predictions concerning mechanisms of mitogen-activated protein kinase-activated protein kinase 2 (MK2) activation and regulation of IkB kinase (IKK) by EGF.

2.2 Results

To assemble a FL model, we first determined local interactions in the network with FL gates based on relationships among particular subsets of the signals based on prior knowledge of which signals regulate the activities of others. This was accomplished using an adaptation of the FL toolbox in Matlab. Once gates were determined, we constructed a global model by connecting the FL gates together. We analyzed the behavior of the global model in terms of the overall dynamics of signaling proteins under various combinations of stimulation by TNF, EGF, and insulin.

Working with FL models involves manipulating logic gates based on several adjustable parameters: (i) *Membership functions* (MFs) are used to map the values appearing at inputs to membership in a pre-specified input state (such as "low", "medium", and "high"). (ii) *Degree of membership* (DOM) is the quantification of the mapping of inputs to MFs and is always between 0 (no membership) and 1 (full membership). Fuzzy logic is so-named because inputs can have non-zero DOM in different MFs, unlike discrete-state logic in which MFs and DOMs only takes on the values 0 or 1 [89, 93]. Figure 2-2D illustrates example MFs for Boolean and fuzzy logic models. (iii) Once the logic rules are established, a FL gate is generated by first *fuzzifying* the inputs, a step that computes the DOM of each input state over the current input values

and the pre-specified MFs. (iv) The *degree of firing* (DOF), then quantifies whether a rule should be used (1) or not (0) as determined from the lowest DOM amongst the antecedents and the *rule weight*, a value between 0 and 1 that allows additional tuning of a rule's importance. (v) In contrast to Boolean logic (BL) gates in which only one rule can fire for any set of input values (that is, only one row in the truth table is applied), FL gates allow multiple rules to fire to varying degrees (defined by the DOF). *Defuzzification* is a final step in which the superposition of multiple rules is resolved to determine the output value for the gate. Because of this flexibility, FL can model intermediate levels of activity using a network similar in structure to a purely "on-off" BL network (Figure 2-2E).

2.2.1 Data for simulation

Gates for the CSR dataset were constructed by inference working from a normalized heat map of the 0-24 hr data and a network diagram, both adapted from the work of Gaudet and Janes et al. (Figures 2-3, 2-4, and 2-5) [43, 58]. FL gates were constructed to represent the responses of signals such as phosphorylation, activation, or total levels of MK2, c-jun N-terminal kinase (JNK), extracellular signal-regulated kinase (ERK), Akt, IKK, Forkhead transcription factor (FKHR), mitogen-activated protein kinase kinase (MEK), IRS-1, cleaved caspase-8 (Casp8), and pro-caspase-3 (ProC3) to cues corresponding to TNF, EGF, or insulin treatment (Figure 2-3, Figure 2-4B). The first five measurements characterize central nodes in five canonical kinase pathways governing epithelial cell death; FKHR is a transcription factor downstream of Akt, MEK is a kinase directly upstream of ERK, IRS(S) and IRS(Y) represent modifications of insulin receptor substrate (IRS) by insulin receptor, and cleaved-caspase-8 is the active

form of the initiator caspase that cleaves caspase-3, an effector caspase responsible for degrading essential cellular proteins, activating CAD nucleases and killing cells.

2.2.2 Assembling a fuzzy logic gate

To illustrate the method by which FL was adapted to model control of an intracellular signaling protein, consider a gate describing control of IRS-1 phosphorylation at serine 636 (IRS(S)) by EGF and TNF (Figure 2-2F-H). For IRS(S), the inputs were TNF concentration, EGF concentration, and time, and the output was the level of IRS(S) phosphorylation. Time was explicitly included as an input to model dynamics and rates. Membership functions were defined to relate input values to the DOM for each input state. For IRS(S), the EGF input variable has low (L) and high (H) states (Figure 2-2F). When normalized EGF activity was ~0, there was a high (~1) DOM to L and low (~0) DOM to H. As the EGF activity increases to 0.5, DOM=0.5 for both L and H. Output variable levels were treated as constants (see Figure 2-2F and Section 2.4); MFs were unnecessary here because gradation of the output is obtained during defuzzification (see below). Once the membership functions were defined, the logic rules were listed as "if A (the antecedent), then B (the consequent)" statements using the inputs and output states as descriptors; e.g., rule 2: if TNF is H and time is L then IRS(S) is H (Figure 2-2F). Each rule had an associated weight factor between 0 and 1, which could be used to quantitatively represent the relative importance of the rules.

The input and output activities were normalized between 0 and 1 for simplicity. For example, in the IRS(S) gate, TNF concentrations of 0, 5, and 100 ng/mL were normalized to 0, 0.5, and 1 as input values to the FL gate (see Section 2.4). To compute the output of a gate for a given set of input values, the first step was the fuzzification of

the input variables (see two examples in Figure 2-2G-H and described in text below). Next, each rule was evaluated, and a degree of firing was calculated as the minimum of the DOMs for the inputs and the rule weight [89, 93]. Finally, the outcomes of each rule fired were resolved into a net output value by defuzzification (see Section 2.4). By way of illustration, consider the two input scenarios in Figures 2-2G-H. In scenario 1 (Figure 2-2G), EGF=1 (DOM to H=1), TNF=0 (DOM to L=1), and time=0.27 (DOM to L=0.4 and H=0.6). Rule 1 fired entirely (output IRS(S) was L) while rules 5 and 6 fired partially because time had partial membership to L and H (antecedents for rules 6 and 5, respectively); rules 2, 3, and 4 did not fire to a meaningful extent. Combining all these, the aggregate gate output was ~0.2, an intermediate value between the full L output from rule 1 and the partial H output from rules 5 and 6. In contrast, scenario 2 (Figure 2-2H) shows a condition (EGF=0, TNF=1, time=0.19) that led to full firing of rule 4 (though this rule has a weight of 0.25), partial firing of rules 2 and 3, and negligible firing of rules 1, 5, and 6. The aggregate gate output in this case was ~0.5.

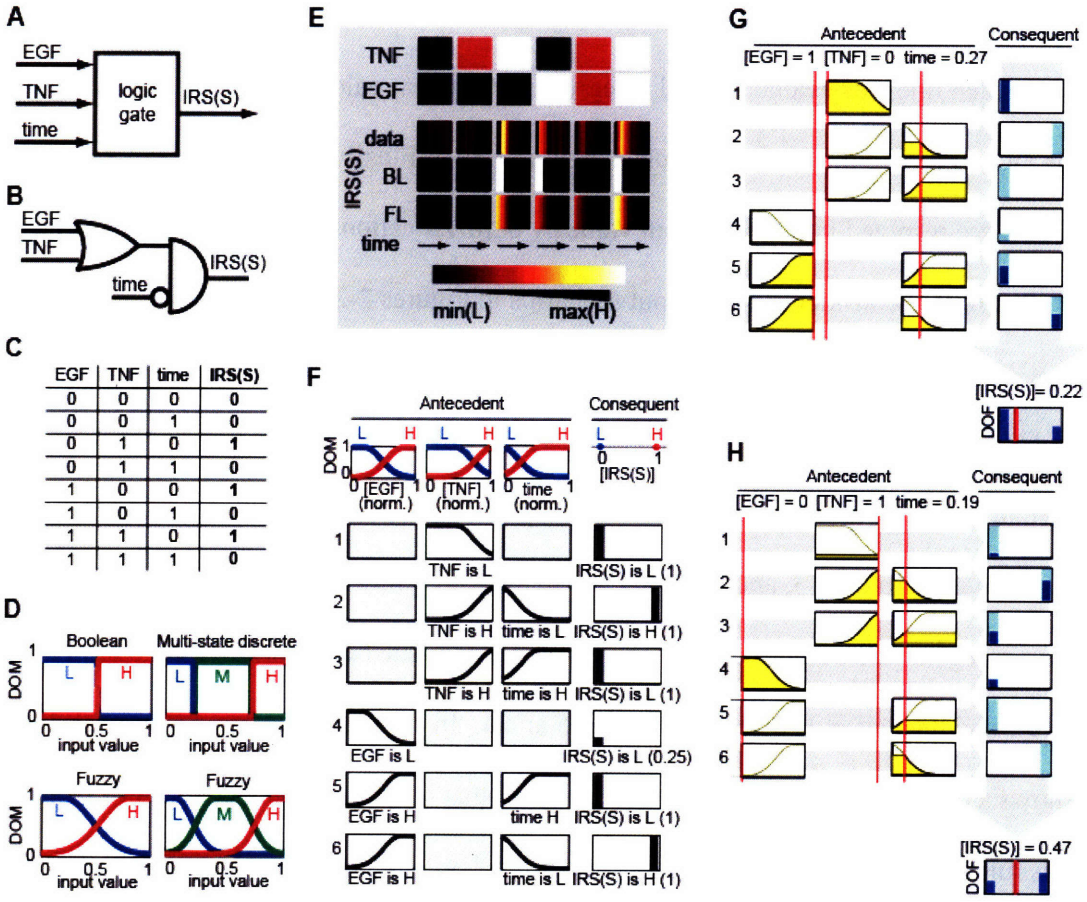

Figure 2-2 Fuzzy logic modeling process

As an example, local logic gate construction is illustrated for IRS(S) (IRS phosphorylation at serine 636). (A) Logic-based models use incoming edges to contain activity level of input or regulatory network species (for IRS(S), the inputs were TNF, EGF, and time) with the logic gate at the node that performs the logic operation to update output signal (IRS(S)). (B) A Boolean logic gate for IRS(S) could be represented in terms of the logic statement "(TNF or EGF) and (NOT(time))", represented here in schematic form where the top shape is an "OR-gate" the circle is a "NOT" operation, and the lower left shape is an "AND-gate"). (C) The truth table for the logic in (B) states the output of IRS(S) (0 for off or 1 for on, in bold) based on the input state. (D) To set up a FL gate, the first step is to assign membership functions (MFs) to the input variables ("TNF", "EGF", and "time"). In this example, each input variable have two or three membership functions ("L", "M", and "H" representing low, medium, and high states, respectively). An MF relates an input value to that state's degree of membership (DOM). MFs for Fuzzy and Boolean (2 MFs)/discrete multi-state (>2 MFs) logic forms are illustrated with the same state thresholds. (E) The simulations from the Boolean logic gate shown in B-C is compared to experimental data and the Fuzzy logic gates specified in F below (see Figure 2-5A for the experimental and simulation conditions). The BL gate is not able to model intermediate state for smooth transitions, and simulations of the FL gate better fit the data as compared to the BL gate. (F) To set up a FL gate, the MFs for the inputs and the constant values for the outputs are defined. For simplicity, we use normalized input and output values. Next, logic rules are listed as "if A (the antecedent), then B (the consequent)" using the input and output states as descriptors. Weights between 0 and 1 are assigned to each rule (indicated in parentheses), which is helpful for rules that should have minor influence (e.g. rule 4). The rules for IRS(S) are each graphically listed with the outline of the membership functions specified for that rule's antecedent. Inputs not considered for an antecedent are indicated by a light gray box. The consequent for each rule is indicated by a bar whose height is proportional to the rule weight. (G-H) Two input scenarios are presented to illustrate FL gate computation

(horizontal gray arrows) and defuzzification (vertical gray arrow). The amount of color filled in (yellow for inputs and blue for output) is representative of the DOM (for inputs) or degree of firing (DOF) given the input values (for outputs). The input values are listed on the top and indicated graphically by the vertical red lines. For example in scenario 1, rule 1 fires (full dark blue bar) because the antecedent (TNF is H) has a high DOM (filled in yellow). The firing strength of the rule is the minimum of the antecedents; therefore, rule 2 does not fire because while time has low DOM to L (~.4) and the DOM of time to H is near zero. To defuzzify (resolve the output value given a set of firing rules), an average is computed from the output values of each rule weighted according to both firing strength and rule weight. The bottom row in the consequent column shows the aggregated outputs and the small red line is the defuzzified or final, value. The scenario illustrations were adapted from the "rule viewer" in Matlab's Fuzzy Logic Toolbox.

2.2.3 Features of various logic gates

To model the experimental compendium data [58], eleven gates were constructed using 2-4 input variables, 2-4 MFs per input, and 2-3 outputs per gate (see Figure 2-3). Each is like a local model characterizing the regulation of the network species. Prior knowledge in the form of a network diagram was used to choose the initial gates and their inputs (Figure 2-4A). We aimed for numbers of inputs, rules, and MFs that were as few and simple as possible while still fitting the data. The MFs and rules were manually fit to the data, though future implementation of machine learning algorithms or automated fitting should improve the speed and quality of the process (see below). By way of illustration consider the JNK and MK2 pathways, which are activated by stress and cytokine treatment and are thought to be co-regulated following EGF or TNF treatment (Figure 2-4A, [36]). During the course of constructing gates for JNK and MK2, we found that the data could be modeled without knowing whether or not EGF had been added, suggesting that activation if JNK and MK2 in our data set was independent of EGF-treatment (Figure 2-3B-C).

For some gates, tweaking of the MFs and rules was not sufficient to give a reasonable fit and changes were required to the types and number of inputs. For example, IRS-1 is the canonical adapter protein downstream of the insulin receptor,

though some of its many phosphorylation sites are also substrates of other receptor kinases, including EGFR [94]. In modeling IRS-1 phosphorylation at two sites, tyrosine 896 (IRS(Y)) and serine 636 (IRS(S)), we found that both were regulated by TNF and EGF but not by insulin (Figure 2-3F and 2-3J). The rules indicate that both TNF and EGF treatment positively affect S636 phosphorylation while TNF inhibits EGF-induced phosphorylation at Y896 (see Section 6.1.1).

During the formulation of the Akt gate, we included inhibitory crosstalk from ERK to Akt because it has been observed in several experimental systems [95-97]. The introduction of crosstalk greatly simplified the rule-base of the Akt gate, suggesting that this crosstalk exists in HT-29 cells (Figure 2-3I). The mechanistic basis for this crosstalk is not understood in the literature, and our most effective model includes a short time delay from ERK to the Akt gate input. Negative crosstalk from the ERK to Akt pathways may be the mechanism by which TNF inhibits Akt phosphorylation upon insulin treatment, as observed by Gaudet et al. [58].

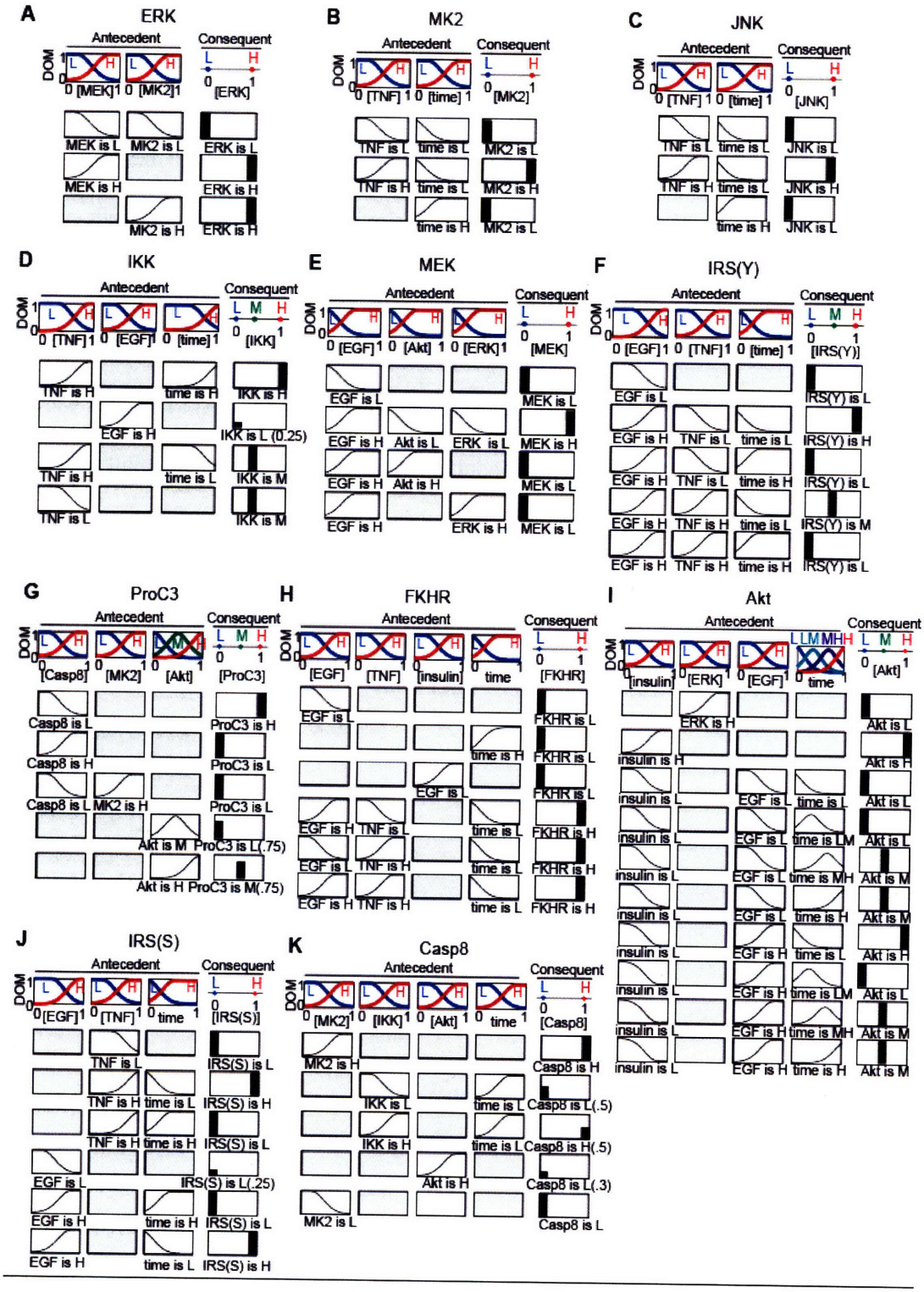

Figure 2-3 Fuzzy logic gate specifications
Each subfigure depicts the MFs and logic rules for the FL gates. The notation is identical to Figure 2-2, except that rule weights are specified only when they are not 1 and input and output concentrations are normalized (arbitrary units).

2.2.4 FL network modeling

An integrated model was constructed by joining together gates and four "inputs" (TNF, EGF, insulin, and time). The signals produced by the FL gates are the model outputs. Time delays were incorporated to model slow processes such as the induction of autocrine transforming growth factor-α [TGF-α] following TNF stimulation [59]. A maximization function was used to unite EGF and TGF-α (not shown) inputs because they bind the same receptor and their contributions to the MEK and Akt FL gates were similar (Figure 2-4B). To execute the model, a simulator stepped though small time steps, updating the gates at each time step (see Section 2.4). The simulation results were evaluated at twelve equal time intervals corresponding to experimental time points.

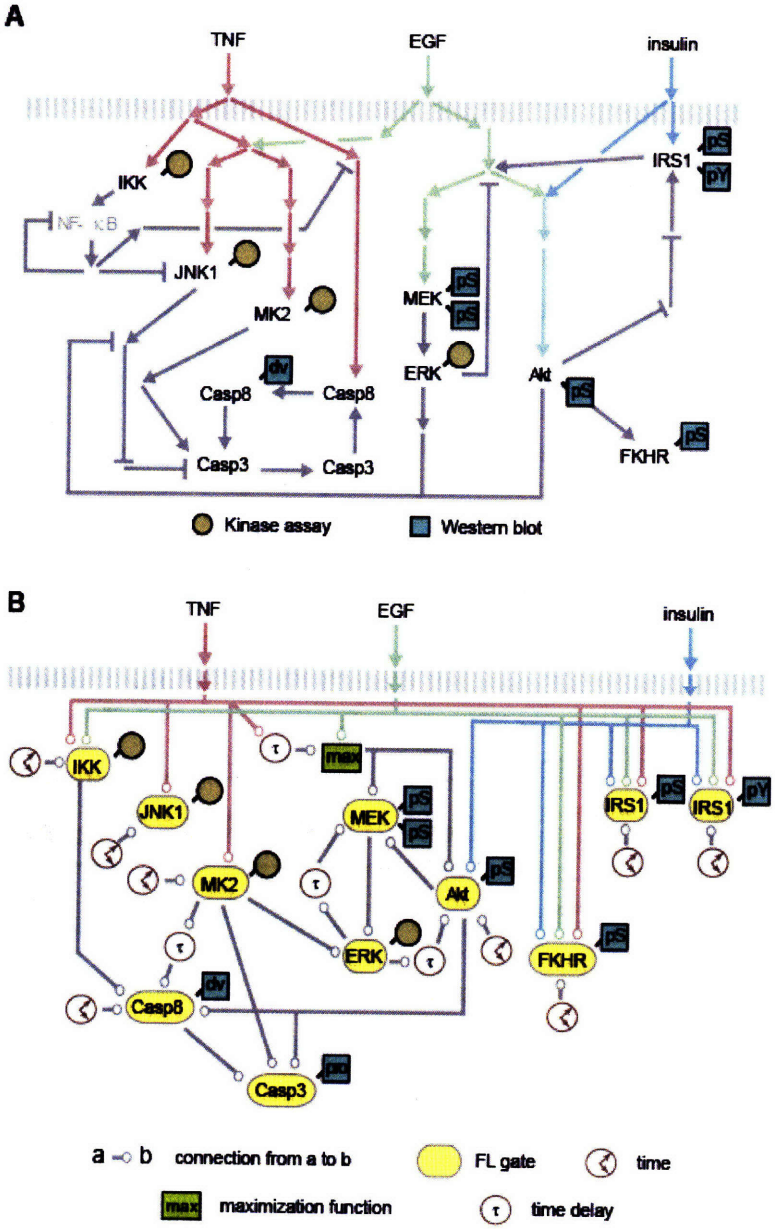

Figure 2-4 Network diagrams
(A) The original network diagram is adapted from Janes et al. [59] and was used as a starting point to construct the FL gates. "T", "E", "I", and "A" signals refer to signals associated with TNF, EGF, insulin, and apoptotic signaling, respectively. Network species whose concentration was measured by Western blot in the data-compendium are notated with an orange square ("pS" for phospho-serine, "pY" for phospho-tyrosine specific antibodies, "clv" for the cleaved form, and "pro" for the uncleaved form). Purple circles mark data compendium proteins measured by kinase assay. (B) This diagram depicts the global FL model, comprised of the 11 local FL gates with time delay and maximization functions. The network topology of the model differs from that of the original diagram.

We observed that our FL model recapitulated major features of the CSR dataset across ten cytokine combinations (Figure 2-5A). For most signals, the differences

between the prediction and the data were minor with respect to signal amplitude and timing. Common to all predicted signals was the absence of the activation lag at the beginning of the time course. To model this lag would require an additional MF for several gates, a feature we omitted for simplicity. It was also challenging to model FKHR phosphorylation. Even though Akt is known to regulate FKHR [98], we could not incorporate it as an input signal to the FKHR gate; instead, we modeled FKHR with inputs of TNF, EGF, insulin, and time (Figure 2-3H). This suggests that in HT-29 cells, FHKR is subject to more complex regulation than simply modification and activation by Akt.

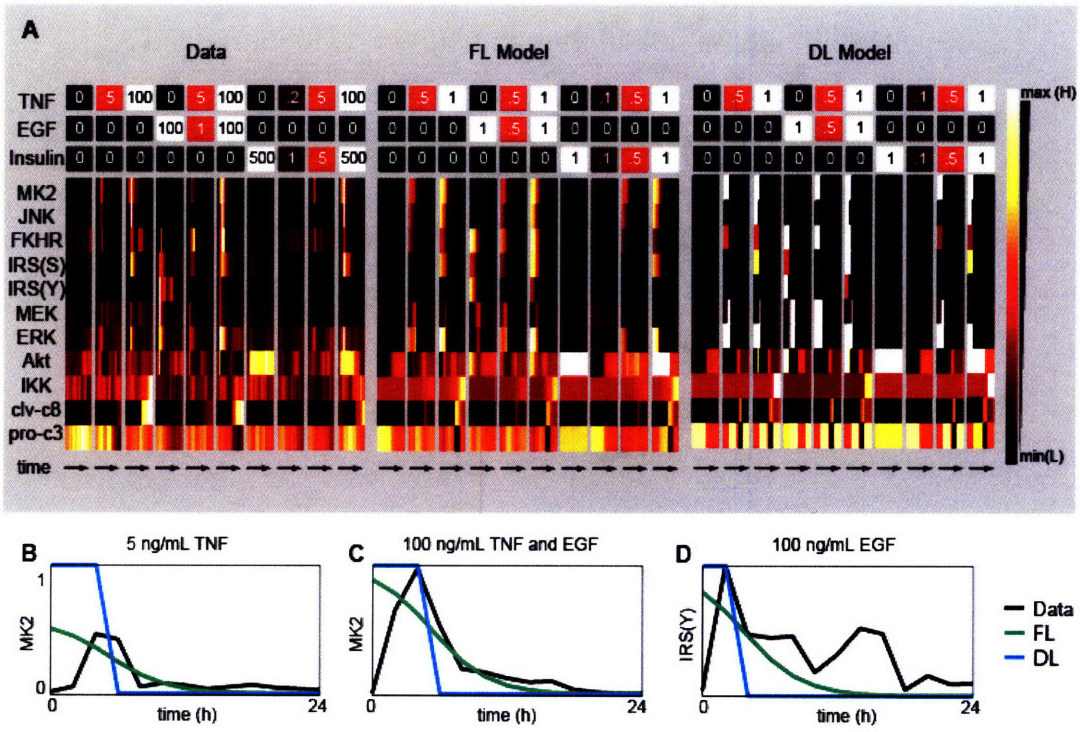

Figure 2-5 The experimental data compendium and simulation of the global FL model
(A) The left heatmap portrays the averaged normalized data from the experimental compendium [58]. Ten stimulation conditions with TNF, EGF, and insulin (top) are shown with the measurements at 0, 5, 15, 30, 60, 90,120, 240, 480, 720, 960, 1200, and 1440 minutes below. Measurement types (western blot or kinase assay) are indicated in Figure 2-4A and are described in detail in Gaudet et al [58]. In the middle, the heatmap shows the results of simulation using the global model under normalized treatment conditions, corresponding with the data compendium shown on the right. Identical simulations of an equivalent discrete logic model (DL, built by changing only the degree of fuzziness from the FL model and leaving the rules and MF thresholds unchanged) are shown on the left (see Section 2.4). The cytokine treatment

concentrations are marked directly on the heatmap in ng/mL for the data and arbitrary units for the models. See Figure 6-2 in the Appendices for an alternative depiction of the data and simulation results. (B-D) Simulation and data time courses are plotted for three treatment conditions to highlight cases where the FL model fit the data better than the DL model (B), where both models have similar performance (C), and both models fail (D).

2.2.5 Comparison of fuzzy and discrete logic

To ascertain whether our FL model was superior to a BL model containing similar gates and connectivity, the FL model was converted into a multi-state discrete model (DL) by leaving the rules and rule weights intact and changing the degree of fuzziness in the MFs to make them discrete (Figure 2-2D, Methods). Under these conditions, the membership thresholds were the same in both the FL and DL models. The discretized model was not a traditional Boolean model however, because the rules were overlapping, making it possible for more than one to fire at the same time. Defuzzification was still required to resolve the firing of multiple rules (see Figure 6-1 in the Appendices). We chose this approach because we wanted to compare fuzzy and discrete models having the same rule base. We anticipate that a more traditional Boolean model would, if anything, be less adjustable and have poorer performance than the discrete model studied here (see Figure 2-2E, Section 2.3, and Section 2.4).

To compare the FL and DL models to data quantitatively, we computed the fitness as a normalized sum of squared differences (see below and Section 2.4). Over all simulations, the FL model was a better fit to the data than the DL model (0.0312 and 0.0676, respectively). In evaluating fits to individual signals, we noticed patterns in the types of data that FL and DL models were able to represent; three examples are shown in Figures 2-5B-D. As expected, the DL model is not as capable as the FL model of recapitulating intermediate activity levels (Figure 2-2B), and ERK activity in the DL

model alternated between low and high while the FL model more accurately reflects graded ERK activities (Figure 2-5A). More striking breakdown between the DL model and data was observed for Akt, IRS(S), and JNK (Figure 2-5A). For IRS(S) and JNK, transient activation was not reproduced in 3 of 6 and 1 of 5 cytokine conditions, At early times, the DL Akt gate was unable to replicate the intermediate activity levels. However, because DL models generate step functions, they are well suited to sharp transient signals (Figure 2-5C). In these cases, both the FL and DL models produced similar results. We also observed cases where both models failed to fit the data, especially where there were both early and late activation peaks (Figure 2-5D). This failure to fit data could be remedied by adding more input states for time and altering the rules (Figure 6-2).

2.2.6 Towards a method for global rule fitting

In the work described above, logic rules and membership functions in the CSR FL model were manually adjusted one gate at a time, but it would be preferable to perform this adjustment automatically. We therefore developed an algorithm that optimizes the weights of all possible rules for a gate by minimizing the sum of the squared differences between the data and the model (see Section 2.4). Following optimization, logic rules that are supported by the data should have weights near 1, while poorly-supported rules should have weights near 0.

We tested the fitting algorithm with the MK2 gate. Using 2 MFs each for the two inputs (TNF and time) and the output (MK2 activity), the gate has $2^3 = 8$ possible explicit rules. MK2 data from the 10 cytokine treatment conditions were used to optimize a vector containing the 8 rule weights. Our initial fitting attempt failed because we were using typical MFs for both inputs, including the time variable (not shown). This was

problematic because the time MFs were not parameterized to model the brief and rapid increase in activation following cytokine treatment. While the difference was minor when the data and the original model simulations are visually compared, the difference was significant when quantified using the sum of squared differences. To account for the lag, an additional MF for time was included to represent this immediate early response, increasing the number of candidate rules to 12. Figure 2-6A shows simulated MK2 activity for the new MFs over time. The fitted gate reproduced the major features of the data using 6 rules with weights near 1. The trained rules with weights near 1 matched our manually determined rules (except for the rules describing the initial time lag, which was not considered in the untrained gate, Figure 2-6B). To test FL gate regression with more rules, we applied the algorithm to the same data using one additional membership function (for medium activity levels) and compared it to an untrained model using the same MFs. The trained rules were very similar to the untrained rules, and identified applicable logic rules that we miss when writing the untrained gate (see Appendices, Figure 6-4). The MK2 test case suggests that it is possible to optimize rule weights as a means to fit logic rules without bias and is a first step towards a more rigorous approach to logic-based modeling.

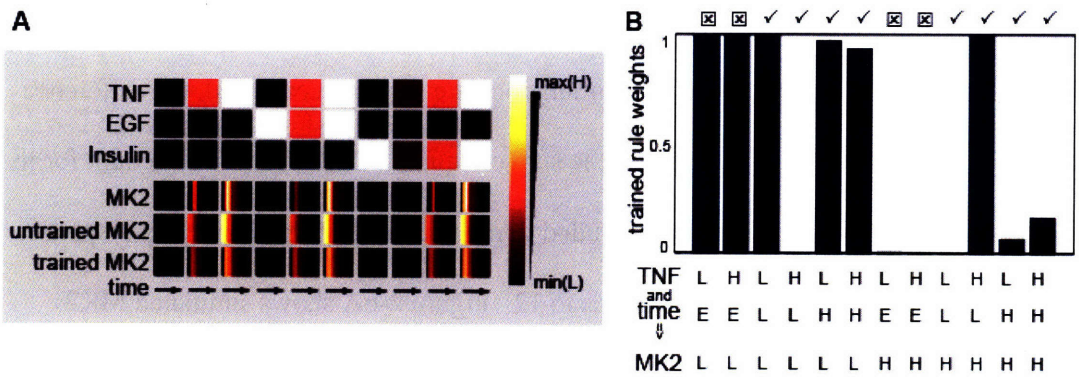

Figure 2-6 Fitting MK2 rule weights
(A) A heatmap depicts the data, untrained model (Figure 2-3B), and trained model time courses for MK2. (B) The regressed rule weights are plotted for the 12 candidate rules. The rules are indicated in tabular format; the first two rows describe the state of the inputs, TNF and time, and the last row is the output MK2 state. L and H represent low and high states, and E is the state describing the early response lag. Symbols above the plot show whether the rules were present (✓) or not applicable (☒) in the untrained model.

2.2.7 Biological predictions

As a second means to evaluate the FL model, we looked for new and potentially testable biological insights (see also the Appendices, Section 6.1). Because each gate effectively represents a local model of cell signaling, it is worth examining the membership functions and the logic rules of gates themselves as their interconnectivity.

2.2.7.1 Mk2 and Erk co-regulation

The dataset includes measurements from three MAPK pathways: JNK, p38 (via MK2), and ERK (with MEK). JNK and p38 respond to stress cues and, following cytokine treatment, are jointly regulated by the upstream kinase MEKK5 [36]. Since MK2 is a substrate of p38, it was not surprising to see a close correlation in the FL model between JNK and MK2. MEK is the immediate upstream activator of ERK [36], but the fit to ERK dynamics was much better if both MEK and MK2 were included as inputs to the ERK gate; under these circumstances, only five simple rules were required to capture

ERK dynamics (Figure 2-3A, Figure 2-5A). Moreover, we judged MK2 to be superior as an input to the ERK gate than TNF, EGF, and insulin because the rule-base was smaller. In the final formulation, MK2 "OR" MEK positively influence ERK. The unexpected involvement of MK2 in ERK regulation suggests either that MK2 regulates ERK in an indirect or direct manner, or that MK2 is tightly correlated with an as-yet unidentified ERK regulator. In previous PLSR modeling, we had observed a role for MK2 in cell survival and the current data suggest that ERK may be an effector for the MK2 survival function [43]. MK2 has previously been reported to regulate TNF and TGF-β expression, two ligands that regulate ERK by engaging cell-surface receptors [99-102], and it is possible that the action of MK2 on ERK is autocrine-indirect; however the time-independence of the interaction in FL model is suggestive of a more direct link.

2.2.7.2 EGF-stimulated inhibition of IKK

In general, TNF (but not EGF) is thought to be an upstream member of the canonical pathway leading to IKK activation (Figure 2-4A, [103, 104]). However, there is evidence that IKK is activated though the EGF receptor following EGF treatment in other cell types (e.g. estrogen receptor negative breast cancer cells) [105]. In building the FL gate for IKK activity, we were surprised to find that the gate's performance was improved by adding a simple rule: "If EGF is H then IKK is L (weight 0.25)" (Figure 2-3D). The necessity of this rule suggests that EGF is a weak, but not insignificant *inhibitor* of TNF-mediated IKK activity.

We have previously reported that in HT-29 cells, TNF induces a complex autocrine cascade in which TNF-induced TGF-α release acts through the EGF receptor to stimulate release of interleukin-1α [IL-1α] [59]. IL-1α was found to have an anti-

apoptotic effect via IKK ~18 hr after TNF treatment. Because activated EGF receptors are known to be down-regulated rapidly [106, 107], we hypothesize that in HT-29 cells, EGF inhibits IKK activity following TNF stimulation by inducing EGF receptor down-regulation. This in turn decreases the number of EGF receptors available to transduce autocrine TGFα signaling, a necessity for IKK activation mediated by IL-1α.

From these and similar examples described in Appendices (Section 6.1), we conclude that potentially interesting biological insights can be drawn from the logic and connectivity of FL gates including insights that were not apparent from simple inspection of the data.

2.3 Discussion

In this chapter we describe the construction and evaluation of a fuzzy logic model of mammalian signaling networks induced by TNF, EGF, and insulin. The logic gates and their associated membership functions, which encode input-out relationships for interactions among various species in the model, were generated based on study of cellular responses to different cytokine treatments. The gates were then linked together based on prior knowledge of network topology and DOFs fitted to data using either induction or a more rigorous fitting process (based on minimizing the difference between simulated and experimental trajectories). The resulting model was interpretable with respect to interactions among species known, from the literature, to act in concert and it generated dynamic trajectories for various species that were similar to those in actual data. We can therefore conclude that efficient assembly of a FL network able to encode complex experimental data is possible.

By building different versions of a FL gate, we were able to intuit potential influences among data points in the data that had gone unnoticed during data-mining with other analytic tools. For example, one biological hypothesis that arose from FL model analysis is that MK2 and MEK are both co-regulators of ERK. This offers a novel potential explanation for the previously published observation that MK2 activity has pro-survival effects [43]. A second observation linking EGF treatment to IKK inhibition led us to hypothesize that EGF-induced downregulation of the EGF receptor might interfere with IKK activation by inhibiting TGF-α induced IL-1α autocrine signaling, which requires the EGF receptor. Thus, the FL model yields predictions about the strength and logic of both direct and autocrine-indirect processes. In the future, the process of choosing the best FL model could be made more rigorous by automating the fit of rules and membership function; this would make the process of hypothesis generation based on model structure considerably more rigorous.

As a starting point to automated fitting of FL models to data, we show that FL rules can be generated by regression to data. The potential for rule fitting opens a plethora of possibilities for improving the capabilities of logic-based modeling and exploring the effects of parameterization and imposed model constraints [108, 109]. Optimization algorithms such as genetic algorithms and Monte Carlo simulations could be used fit membership functions and rule weight simultaneously. However, key to developing an automated methodology for FL modeling would be the creation of a metric to evaluate the performance of FL (and BL) models that balances the complexity of model (and the associated degrees of freedom) with goodness of fit to data: incorporating more gates and MFs usually improves the fit, but also increases significantly the number

of free parameters. For example, we observed that the capacity of multi-state discrete logic gates to more effectively capture quantitative data features can be increased by including a greater number of memberships (states) (see the Appendices, Figure 6-3). Therefore, either fuzzification or inclusion of additional states can strengthen a DL model. A solid metric of model quality would make it possible to compare FL and BL models rigorously as well as evaluate models of the same processes that differ in topology or MFs.

In conclusion, the current FL model of TNF/EGF/insulin-induced signaling in HT-29 cells begins to explore the potential of FL methods to model cell signaling networks. In the future, the introduction of automated model fitting, a graphical-user interface tailored to biological applications, and better means to mine and incorporate literature data should facilitate the application of FL modeling methods. Moreover, FL models can be merged with differential equation models to form hybrid models with particular utility in cases in which some process are well described, receptor-ligand binding and immediate early signaling for example, but the biochemical details of downstream processes such as induced gene transcription are less well specified. One approach to such model fusion would be to reverse engineer part of a differential-equation model to generate the look-up tables necessary for construction of various logic gates. We are currently exploring these and other approaches to expanding the areas of application of FL logic from industrial control to interpretation of complex biological data.

2.4 Materials and Methods

2.4.1 Computational programming

The model was written and run using Matlab R2007a. Individual FL gates were constructed and tested using the Matlab Fuzzy Logic Toolbox using the Sugeno inference method. To parameterize the "gauss2mf" membership function shape, a Python script was used to coordinate the MF slope (.250 for FL and .0001 for BL models) with intersections at a 0.5 DOM. Input and output values ranged from 0 to 1 for simplicity and were empirically normalized. For example, each of the twelve time-steps in the data compendium were equally spaced as inputs to the FL gates even though they were not evenly spaced in real time. We used a default of two states (membership functions) for each variable and the number was increased as needed (heuristically). We decreased the number of free parameters by imposing a single degree of fuzziness on the model and constants for output memberships. The global model was built and run in Simulink, using its standard libraries for maximization functions, time, and time delays.

2.4.2 Model fitness

Model fitness was calculated by dividing the sum of the squared difference between a model and the data by the number of data points. For the whole set of simulations, there were 1430 data points.

2.4.3 Global logic gate regression

Rule weight optimization was achieved by using non-linear least squares regression between the model and the dynamic data under the ten treatment conditions.

Because a gate's output is defuzzified by using a weighted average of the rules fired, sets of firing rules can all have low weights without altering the final output. To highlight firing rules in any circumstance, rule weights were normalized at each iteration of optimization so that the weights of rules with the same antecedents sum to 1. Our manually assembled gates were similar to the fitted gates, but necessarily contain condensed and simpler rules sets. For example, we would write the rules "If TNF is L and time is H then MK2 is L" and "If TNF is H and time is H then MK2 is L" in a condensed form: "If time is H then MK2 is L". For rule fitting, we started by generating full description versions of each possible rule. The optimization procedure was scripted in Matlab R2007a and used the Matlab Optimization toolbox (lsqcurvefit).

3 Direct Lyapunov Exponent Analysis Enables Parametric Study of Transient Signaling Governing Cell Behavior[3]

3.1 Introduction

Reaction models employing differential equations are frequently used as tools for computational exploration of complex biomolecular networks, such as those involved in signal transduction of extracellular stimuli governing cell fate. These models, generally based on mass-action kinetics, incorporate network topology and quantitatively describe the kinetics of interactions between network components [46, 50, 110-116]. Because these mechanistic models are large and complicated, quantitative analysis is necessary to extract understanding [114, 117]. A typical objective of model analysis is to comprehensively characterize the response of the signaling network to changes in system parameters. By altering network behavior, changes to protein levels or reaction rates may lead to different cell fates following exogenous stimulation [118-121]. As an example, activation of the small GTP-binding protein Ras can induce a variety of cell responses including cell proliferation and differentiation, depending on the cell type and extracellular conditions. Perturbations to the Ras-mediated regulatory network can promote pathological cell behavior; mutations that affect Ras levels or binding or reaction rates are often linked to cancer [122]. Numerous similar examples may be found underlying cell behavioral dysregulation; thus, illuminating how changes in molecular interactions alter signaling network behavior is key to understanding the molecular basis of disease. Simulations can be used to inspect signaling behavior arising from network

[3] This chapter is a postprint of the article 77. Aldridge, B.B., et al., *Direct Lyapunov exponent analysis enables parametric study of transient signalling governing cell behaviour.* Syst Biol (Stevenage), 2006. **153**(6): p. 425-432.

perturbations of potential interest – perhaps a genetic mutation or pharmacological intervention [68, 114]. By simulating a mechanistic model, predictions can be made about how specific changes to parameters such as stimulation or drug inhibition conditions, initial concentrations, and reaction rates will affect signaling [47, 50, 123-127]. To link different cell responses to complex signaling interactions, however, more systematic, comprehensive analysis methods need to be applied.

Common systematic tools for studying the behavior of differential equation models for signaling networks include parameter sensitivity analysis and steady-state analysis. Determining sensitivity to rate constants and initial conditions (*i.e.*, protein levels at the initial time point) is useful for finding reactions and species that are particularly important in the overall reaction scheme [76, 128, 129]. However, the local sensitivities that may arise from intertwined multivariate interactions cannot be revealed by single-parameter sensitivity analysis. A comprehensive analysis, where several parameters are changed simultaneously, is often computationally impractical and the results intractable. The analysis method presented in this work is based on direct Lyapunov exponents (DLEs), which is a comprehensive local sensitivity analysis of model initial conditions. The DLE approach can be interpreted in a manner that is analogous to steady-state analysis of metabolic networks. Our analysis goal is to understand how the qualitative network behavior (essentially, the biological fate) depends on the quantitative combinations of network component parameters (essentially, the network state).

Steady-state analysis methods have been established in dynamical systems as powerful methods for analyzing models of a variety of physicochemical processes, including fluid flow and chemical reactions. These techniques, including fixed-point

bifurcation methods, have been successfully used to study several biological network models. These methods delineate how changes in initial conditions and rate parameters affect the biological outcomes associated with different equilibria. Good candidates for this analysis are systems with multiple steady steady-states, where each phenotypic behavior is associated with a particular steady-state. Examples include metabolic networks, the cell cycle, and engineered gene networks [49, 110, 113, 130, 131]. In contrast, many signal transduction networks affect cell fate through transient, pre-steady-state signals. Here, we will refer to these systems as "transient response networks". In transient response networks, rapidly-changing signals, or transients, induce changes in other signals that propagate through the pathways [47, 58, 118, 126]. In these systems, the time-evolution of transient signals, not steady-state signals, influences cell behavior. For this reason, transient response systems may not be good candidates for steady-state analysis. To understand these systems, we require methods that analyze transient signals, such as DLE analysis described here.

The transient response system that we analyze in this work is a core sub-network of the signal transduction cascade regulating the programmed cell death (apoptosis)-versus-survival phenotypic decision. Apoptosis has in some previous work been modeled as a bistable system where death and survival are distinct stable steady-states [132, 133]. However, this is not the only way, nor necessarily the most appropriate way, to cast a problem that appears to involve a transient response network [43, 58]. In fact, models focusing on the later stages of the apoptotic decision such as ours as well as one of the alternative models developed by Eissing et al. do not exhibit bistablity [132, 133]. In response to apoptotic stimuli, this network produces a transient response that is

dependent on the stimuli and the state of the cell. The transient signals will either lead to apoptosis (where the network does not reset because the cell dies) or survival (where the network resets).

Apoptosis is induced by extrinsic (receptor-dependent) and intrinsic (intracellular) pathways. Common to both pathways is the activation of caspases, a family of proteases that execute the cell death decision by cleaving protein targets. The caspases activate each other to form a protease cascade and are themselves subject to regulation by many other proteins [1, 17, 29]. Caspases are synthesized in an inactive state (pro-caspases or zymogens) and become active when dimerized or cleaved by other caspases. Intracellular or extracellular pro-death stimuli lead to dimerization and cleavage of initiator caspases such as caspase-8. Once activated, these initiator caspases in turn cleave and activate effector caspases such as caspase-3 (Figure 3-1). Activation of initiator by effector caspases generates positive feedback that can amplify this cascade [17, 18]. Prolonged activation of effector caspases leads to programmed cell death. A critical inhibitor is X-linked inhibitor of apoptosis (XIAP), which negatively regulates the enzymatic activity of caspase-3. Additionally, XIAP tags active caspase-3 for ubiquitination. This modification promotes caspase-3 degradation and causes caspase-3 activity to be transient [27, 134].

Analogous to the application of steady-state analyses to signaling networks where equilibria correspond to cell response, we describe direct finite-time Lyapunov exponent (DLE) analysis as a method to study transient response signaling networks. We use DLEs to analyze how transient signaling dynamics are affected as different parameters change individually or simultaneously in multidimensional phase-space (the set of initial

chemical species concentrations). DLE analysis is not the first method to measure local sensitivity analysis, but is distinguished from previously applied techniques because DLEs are calculated as parameters change simultaneously, not individually [76]. DLEs were originally used to find invariant manifolds in dynamical systems and fluid flows [135-138]. Similarly, we use DLEs to find separatrices, or sensitive regions in phase-space that separate signals giving rise to different responses. Separatrices are useful because they quantitatively identify points at which continuous change in species concentration lead to dramatic, discontinuous change in response. As an example of current interest in molecular cell biology, we used DLEs to analyze a small, mechanistic model of a transient response network describing caspase-3 activation in the network described above. We were able to characterize initial conditions (concentrations of protein species) leading to survival and apoptosis with the DLE-defined separatrix, but not by examining steady-states. We thereby gained conceptual insight into the integrated effects of multiple components in this network.

3.2 Methods

3.2.1 Caspase-3 activation model

A system of ordinary differential equations describing the activation of caspase-3 by caspase-8 was constructed using mass-action kinetics and the known topology of this portion of the apoptosis regulatory network (Figure 3-1). We have made the following central assumptions: [a] chemical species are present at spatially-uniform concentrations; [b] caspase-6 is not involved in the feedback between active caspase-3 and caspase-8; [c] ubiquitination can be represented by a single lumped reaction; and [d] caspase activation

is achieved after an inactive caspase interacts with an active caspase. The differential equation describing the concentration of active caspase-3 tagged for ubiquitination (x_9) was removed from the model because it does not affect the network. Values for the rate constants are listed in Table 3-1. The equations defining the model are as follows:

$$\dot{x}_1 = -k_1 x_4 x_1 + k_{d1} x_5 \quad (1)$$

$$\dot{x}_2 = k_{d2} x_5 - k_3 x_2 x_3 + k_{d3} x_6 + k_{d4} x_6 \quad (2)$$

$$\dot{x}_3 = -k_3 x_2 x_3 + k_{d3} x_6 \quad (3)$$

$$\dot{x}_4 = k_{d4} x_6 - k_1 x_4 x_1 + k_{d1} x_5 - k_5 x_7 x_4 + k_{d5} x_8 + k_{d2} x_5 \quad (4)$$

$$\dot{x}_5 = -k_{d2} x_5 + k_1 x_4 x_1 - k_{d1} x_5 \quad (5)$$

$$\dot{x}_6 = -k_{d4} x_6 + k_3 x_2 x_3 - k_{d3} x_6 \quad (6)$$

$$\dot{x}_7 = -k_5 x_7 x_4 + k_{d5} x_8 + k_{d6} x_8 \quad (7)$$

$$\dot{x}_8 = k_5 x_7 x_4 - k_{d5} x_8 - k_{d6} x_8 \quad (8)$$

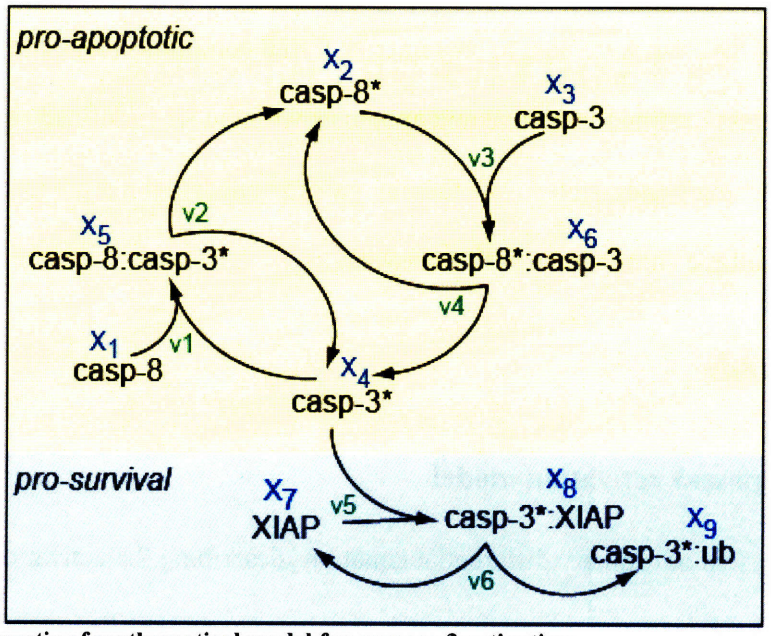

Figure 3-1 Schemstic of mathematical model for caspase-3 activation
Caspase-3 (casp-3) activity is regulated by caspase-8 (casp-8) and XIAP. Caspase-8 (an initiator caspase) activates caspase-3 (an effector caspase) after forming a complex. Positive feedback is similarly accomplished through activation of caspase-8 by caspase-3. XIAP inhibits active caspase-3 by tagging it for ubiquitination and degradation. Here, a star indicates the active form of the caspases, a colon indicates a complex, and 'ub' indicates ubiquitination tagging. Labels in blue and green correspond with species and reaction numbers, respectively.

Parameter	Value	Units
k_1	2.67×10^{-9}	$cell*(s*molec)^{-1}$
k_{d1}	1×10^{-2}	s^{-1}
k_{d2}	8×10^{-3}	s^{-1}
k_3	6.8×10^{-8}	$cell*(s*molec)^{-1}$
k_{d3}	5×10^{-2}	s^{-1}
k_{d4}	1×10^{-3}	s^{-1}
k_5	7×10^{-5}	$cell*(s*molec)^{-1}$
k_{d5}	1.67×10^{-5}	s^{-1}
k_{d6}	1.67×10^{-4}	s^{-1}

Table 3-1 Parameter values and units
Parameter names include the reaction number and "d" for dissociation constants. All parameters except for k_{d5} and k_{d6} were derived from a physico-chemical model fit to quantitative data from time courses of HT-29 human colon carcinoma cells treated with TNF [B. Schoeberl, S. Gaudet, D. Lauffenburger, and P. Sorger, unpublished results]. k_{d5} was derived using parameters in [21]. The ubiquitination rate, k_{d6}, was assumed to correlate with an average delay of 100 minutes between ubiquitination tagging and degradation.

3.2.2 Direct finite-time Lyapunov exponent (DLE)

The DLE is a measure of local sensitivity to changes in initial conditions, evaluated multidimensionally at a finite-time, as depicted for one dimension in Figure 3-2. First, for a selected trajectory, the derivative of the current trajectory position with respect to its initial location is calculated in all independent directions at each finite time instant of interest. These directional derivatives are in turn assembled into a time-dependent gradient matrix, whose entries are indicative of the rate at which neighboring trajectories separate in the corresponding directions. The spectral norm (or largest singular value) of the gradient matrix gives the instantaneous maximal rate of local trajectory separation over all directions. The DLE associated with the selected trajectory is then defined as the time-averaged logarithm of the above norm, measuring the maximal rate of exponential separation between the underlying trajectory and nearby trajectories. By definition, large DLE values reveal large local sensitivity in the flow with respect to changes in initial conditions.

In numerical computations, we select a sufficiently dense grid of initial conditions for which numerical differentiation gives meaningful results. We then launch trajectories from each grid point and calculate the DLE value defined above for each trajectory. We plot the resulting DLEs over the initial grid to identify locations of highly sensitive initial conditions. Regions of phase-space exhibiting different qualitative behaviors are necessarily separated by sensitive initial conditions, and hence their boundaries (separatrices) will appear as local maximizers of the DLE field. The accuracy of separatrix locations obtained in this fashion will increase as the initial grid size is refined. By the continuous dependence of trajectories on initial conditions, separatrices are captured by our procedure even if they do not exactly intersect the initial grid. This is because separatrices have whole neighborhoods of increased sensitivity, which are captured by a dense enough initial grid.

DLEs, apart from their application described here, are particularly useful in finding repelling and attracting surfaces and have been used in fluid mechanics [137, 138] and rigid body dynamics [138]. In [135, 136], we proved that DLEs robustly identify the locations of maximum stretching (divergence between nearby trajectories). We use the maximum stretching among all dimensions to measure the rate of exponential separation for a finite-time between two neighboring trajectories (Figure 3-2).

To quantify the degree of stretching at particular initial conditions, first we define the separation (9) and approximate it by linearization (10).

$$\zeta(t) = \mathbf{x}(t, t_0, \mathbf{x}_0 + \zeta_0) - \mathbf{x}(t, t_0, \mathbf{x}_0) = \frac{\partial \mathbf{x}(t, t_0, \mathbf{x}_0)}{\partial \mathbf{x}_0}\zeta_0 + \mathrm{O}(|\zeta_0|^2) \qquad (9)$$

$$\zeta(t) \cong \frac{\partial \mathbf{x}(t)}{\partial \mathbf{x}_0}\zeta_0 \qquad (10)$$

Here $\mathbf{x}$ and ζ are vectors describing species concentration and trajectory separation, respectively. Next, we define stretching as the matrix (spectral) norm of the deformation gradient $\frac{\partial \mathbf{x}(t)}{\partial \mathbf{x}_0}$. Recalling

$$\|\mathbf{A}\| = \left(\lambda_{\max}\left(\mathbf{A}^T\mathbf{A}\right)\right)^{1/2} \tag{11}$$

for a square matrix $\mathbf{A}$ (where $\lambda_{\max}(\mathbf{X})$ denotes the maximum eigenvalue of $\mathbf{X}$), we obtain

$$\left\|\frac{\partial \mathbf{x}(t)}{\partial \mathbf{x}_0}\right\|^2 = \lambda_{\max}\left(\left(\frac{\partial \mathbf{x}(t)}{\partial \mathbf{x}_0}\right)^T\left(\frac{\partial \mathbf{x}(t)}{\partial \mathbf{x}_0}\right)\right). \tag{12}$$

We then define the finite-time maximal (over all directions) stretching rate experienced along the trajectory $\mathbf{x}(t, t_0, \mathbf{x}_0)$ as

$$\frac{1}{t-t_0}\log\left\|\frac{\partial \mathbf{x}(t)}{\partial \mathbf{x}_0}\right\| = \frac{1}{2(t-t_0)}\log\left[\lambda_{\max}\left(\left(\frac{\partial \mathbf{x}(t)}{\partial \mathbf{x}_0}\right)^T\left(\frac{\partial \mathbf{x}(t)}{\partial \mathbf{x}_0}\right)\right)\right]. \tag{13}$$

Note that we can treat $\frac{1}{2(t-t_0)}$ as a constant because the stretching rates are compared at a particular time t. Therefore, we can further simplify (13) to define the DLE by factoring out this constant:

$$DLE(t, \mathbf{x}_0) = \log\left[\lambda_{\max}\left(\left(\frac{\partial \mathbf{x}(t)}{\partial \mathbf{x}_0}\right)^T\left(\frac{\partial \mathbf{x}(t)}{\partial \mathbf{x}_0}\right)\right)\right]. \tag{14}$$

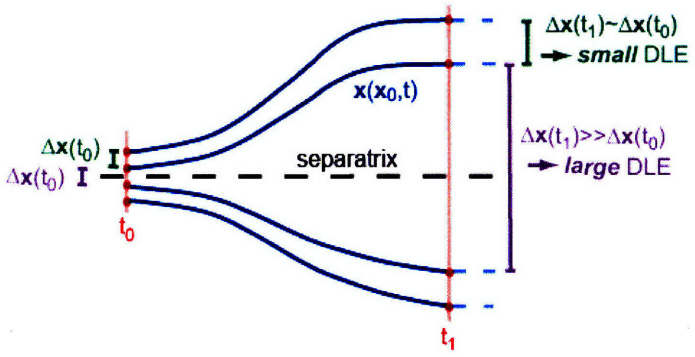

Figure 3-2 Large DLEs identify the location of maximum separation between trajectories, defining a separatrix.
Direct finite-time Lyapunov exponents (DLEs) measure local sensitivity to initial conditions. Relative to the time point used in the calculation of the exponent, small DLEs indicate little sensitivity (green). Large exponents indicate high sensitivity near the initial conditions (purple).

3.2.3 DLE computation and visualization

Classical finite-time Lyapunov exponents are typically computed for

$$\dot{\mathbf{x}} = \mathbf{f}(\mathbf{x}, t) \tag{15}$$

by numerically solving the linear system

$$\dot{\zeta} = \frac{\partial \mathbf{f}}{\partial \mathbf{x}}\left(\mathbf{x}(t, t_0, \mathbf{x}_0), t\right)\zeta, \tag{16}$$

obtained from differentiating (10) in time. By contrast, DLEs are computed directly from (10), without the laborious solution of (16) along all trajectories. Specifically, we compute finite-time Lyapunov exponents directly by differentiating final trajectory positions with respect to their initial condition (hence the terminology "direct" Lyapunov exponent).

To compute DLEs, a grid of initial conditions sampling phase-space was chosen, and each set of initial conditions was integrated with respect to time using the ode15s solver in MATLAB 7.0 (The Mathworks, Natick, Massachusetts). The deformation

gradient $\frac{\partial \mathbf{x}(t)}{\partial \mathbf{x}_0}$ was then obtained from a numerical differentiation of final trajectory position with respect to their initial conditions. Next, the natural log of the maximum eigenvalue of the strain tensor $\left(\frac{\partial \mathbf{x}(t)}{\partial \mathbf{x}_0}\right)^T \left(\frac{\partial \mathbf{x}(t)}{\partial \mathbf{x}_0}\right)$ was computed to find the DLE, as defined in (14), at each initial condition.

For a grid of approximately 1.6×10^6 points, the entire computation (including trajectory integration) was completed in approximately 85 hours on a Linux workstation with 2 GB of memory and dual 2.80 GHz Intel Xeon processors. The points on the grid were linearly spaced along each direction. The MATLAB code performing the computation is provided at http://cdp.mit.edu/. The resulting DLEs were visualized using Spotfire DecisionSite (Spotfire, Somerville, Massachusetts).

3.3 Results

3.3.1 The cell phenotypic response of apoptotic death is governed by transient signals in a caspase-mediated network

As a test case of a biologically-important transient response network, we explored a mechanistic, differential equation-based model of caspase-3 activation depicted in Figure 3-1. This network includes both pro-apoptotic elements (caspase-8 and caspase-3) and a pro-survival factor (XIAP). While it has only eight distinct species (and dimensions), our caspase-3 activation model is complex enough to be obscure without analysis.

In the presence of active caspase-8, this network produces a transient response that is dependent on the initial conditions (concentrations) of the eight network species

(Figures 3-3A-B). In cells, apoptosis is triggered by elevated and prolonged caspase-3 (or effector caspase) activation. Figure 3-3 shows simulated time courses (trajectories) from our model, where apoptotic cells are categorized as exhibiting a relatively tall and wide pulse of active caspase-3, while surviving cells are characterized by short and narrow spikes of active caspase-3. As expected in a transient response system, we observe that after loss of the transient signal, pro- and anti-apoptotic time courses eventually reach the same type of steady-state (Figures 3-3C and 3-3D). A careful look at the time-scale shows that it takes nearly a week for the pro-death signal to reach equilibrium. In reality, such a cell would have died before the end of two days, and this steady-state would never be reached. For simplification, this model does not include protein turnover. We observed that the introduction of turnover into our model did not significantly change its response (see the Appendices, Section 6.2).

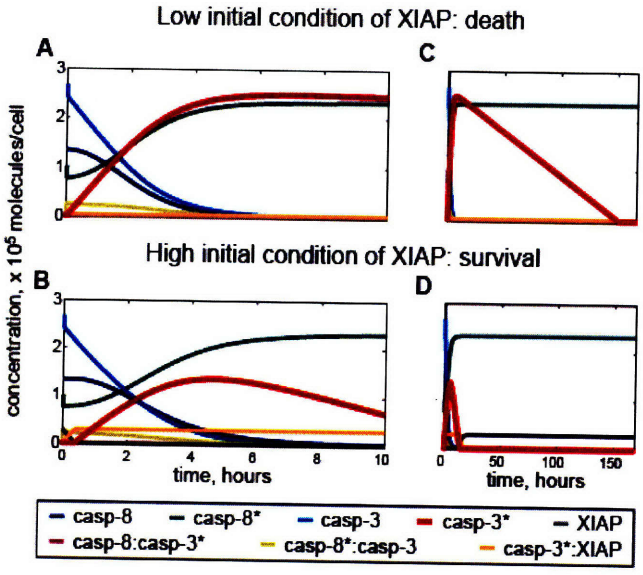

Figure 3-3 Time-course simulations show transient death and survival responses under two different initial conditions of XIAP.
(A) With little XIAP (2.9 x 10^3 molecules/cell) to inhibit activation of caspase-3, caspase-3 activation is sustained and destines this cell for death. In these time courses, the initial conditions were 0 molecules/cell for intermediate complexes and active caspase-3, 1 x 10^5 molecules/cell for active caspase-8, 1.34 x 10^5 molecules/cell for inactive caspase-8, and 2.67 x 10^5 molecules/cell for inactive caspase-3.

(B) With more XIAP (2.9 x10^4 molecules/cell), the pulse of caspase-3 activity is small and destines this cell for survival.
(C,D) A longer time course shows that both apoptotic and non-apoptotic signals arrive at the same type of fixed point. The simulation conditions are the same as in (A) and (B), respectively.

This preliminary inspection of the caspase-3 activation model demonstrates that transient signals for pro- and anti-apoptotic conditions differ qualitatively. These two types of trajectories separate from one another before reaching steady-state. Furthermore, the behavior of the network is dependent on initial conditions. By increasing the initial concentration of XIAP, the transient signal changes from a pro-apoptotic to a pro-survival signal (Figure 3-3). We anticipate that there is a sensitive initial condition of XIAP at which the behavior of the network changes, and that this sensitive point will shift according to initial conditions of the active and inactive caspases.

3.3.2 Large DLEs define a separatrix separating phase-space into pro- and anti-apoptotic regions

As described in the Introduction and Methods sections, we employ direct Lyapunov exponents (DLEs) to search our model phase-space for regions delineating diverse behavior of transient network signals related to different cell phenotypic responses (see Figure 3-2). Neighboring trajectories in these regions will veer away from each other, thus exhibiting large DLEs that effectively define separatrices dividing the phase-space into regions possessing different trajectory behaviors. Because DLEs are calculated for the endpoint of the trajectories, they depend on the specific time-point at which the trajectory separation is measured. This feature is a crucial aid in studying transient response systems, for it insures that the analysis can be performed based on transient signals.

To characterize the network's dependence on initial conditions in multiple dimensions, we computed DLEs across an eight-dimensional grid spanning a wide range of initial species concentrations. Totaling approximately 1.6×10^6 points, the grid points are linearly spaced along each direction. These concentrations were chosen to encompass protein expression across cell populations and under different signaling conditions in Hct-116, HeLa, and HT-29 carcinoma cell lines (10^2-10^5 molecules/cell for XIAP and 10^2-3.5×10^6 molecules/cell for the caspases [S. Gaudet and K. Leitermann, personal communication]). Biochemical intermediates were sampled with coarser resolution because they were not found to contribute to the network behavior (data not shown). To find a separatrix, DLEs were calculated at six hours, by which time Hct-116, HT-29, and HeLa cells would have responded to treatment with death-inducing ligands Tumor Necrosis Factor (TNF) or TNF-related apoptosis-inducing ligand (TRAIL) [B. Aldridge, unpublished observations]. To determine how narrow the time-window of effective separatrix appearance might be, we additionally undertook DLE calculations across the range between two and twelve hours, and found that the separatrix did not move noticeably (data not shown).

Since it is problematic to simultaneously visualize the phase-space in eight-dimensions, in Figure 3-4 we offer more accessible illustrations of the DLEs in three-dimensional slices. Figure 3-4A illustrates the DLEs in the subspace containing XIAP, caspase-8, and active caspase-8, whereas Figure 3-4B shows the DLEs in the subspace containing XIAP, active caspase-8, and active caspase-3. Large DLEs (blue) define a finite-time separatrix that identifies the points at which the balance between XIAP and active caspase-8 shifts so that the overall response changes from pro-apoptotic to anti-

apoptotic signals. We expected the apoptosis regulatory network to have a separatrix because the cell's response is either survival or death – it is not graded (from alive to sick to dead). If a system were to exhibit a more graded response, the DLEs would have been more uniform across phase-space and would not have yielded a discernible separatrix.

The location and shape of the separatrix provide a framework to generate conceptual interpretation of network operation. The separatrix shifts towards higher XIAP concentrations as the amount of active caspase-8 increases (Figure 3-4A). Cells will die if above the separatrix, whereas below the separatrix there is enough XIAP to overcome the conversion of inactive caspase-3 to active caspase-3 by active caspase-8. The separatrix shape is invariant to inactive caspase-8, suggesting that the positive feedback activating caspase-8 by caspase-3 has less influence than the regulation of caspase-3 by active caspase-8 and XIAP. Since XIAP tags active caspase-3 for degradation, more XIAP would be needed to rescue the cell from a death decision if there was a higher initial concentration of active caspase-3 (Figure 3-4B). Figure 3-4C shows perturbations to the separatrix as the ubiquitination rate constant is changed. As the rate increases, so does the slope of the separatrix in the XIAP and active caspase-8 subspace. The slower the ubiquitination rate, the longer the complex of active caspase-3 and XIAP will exist, effectively lowering the concentration of free XIAP. We also observed that the separatrix is not a simple plane – it curves at higher concentrations of active caspase-8 and shifts slope as the ubiquitination rate changes (Figure 3-4C).

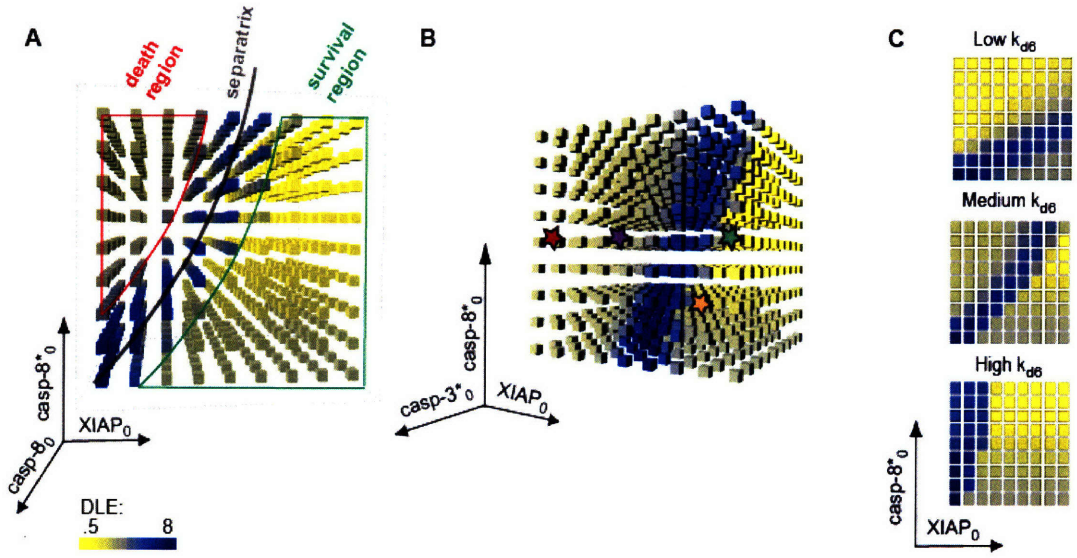

Figure 3-4 The six-hour DLE defines a separatrix separating phase-space into pro- and anti-apoptotic decisions.
Phase-space subplots are shown on a linear scale with initial conditions of XIAP and the active caspases ranging from 1 x 10^2 to 1 x 10^5, and 1 x 10^2 to 3.5 x 10^5 molecules/cell for the inactive caspases. All concentrations refer to initial conditions. The subspaces plotted were chosen to closely match the protein concentrations in untreated HT-29 cells [S. Gaudet and K. Leitermann, personal communication].
(A,B) Large DLEs of the caspase-3 activation network at six hours defines a separatrix. The blue curve is the separatrix which divides the phase-space into regions where cells survive (to the right of the separatrix) or die (to the left of the separatrix). (A) DLEs are shown in a subspace containing XIAP, active caspase-8, and inactive caspase-8 with 2.6 x 10^5 molecules/cell of inactive caspase-3 and 1 x 10^2 molecules/cell of active caspase-3 and the intermediate complexes. The gray curve highlights the separatrix, while the pro- and anti-apoptotic regions are outlined in red and green, respectively. (B) DLEs are shown in the subspace containing XIAP, active caspase-8, and active caspase-3 with 2.6 x 10^5 molecules/cell of inactive caspase-3 and inactive caspase-8, and 1 x 10^2 molecules/cell of the intermediate complexes. The stars indicate reference points (individual cells with different protein levels). The red and purple cells are pro-apoptotic while the green and orange cells are anti-apoptotic.
(C) The separatrix shape is sensitive to rate constants. As the rate of ubiquitination is decreased (k_{d6} increased), the slope of the separatrix increases. The DLEs are shown in the subspace containing XIAP and active caspase-8, with 2.6 x 10^5 molecules/cell of inactive caspase-3 and inactive caspase-8, and 1 x 10^2 molecules/cell of the intermediate complexes and active caspase-3. From low to high, the rate constant k_{d6} has values 3.33 x 10^{-5}, 1.67 x 10^{-4}, and 8.3 x 10^{-4} s^{-1}.

In addition to using the separatrix as a tool to help us interpret the decision-making mechanisms of the network, the separatrix quantitatively identifies the critical ratios of initial conditions around which the cell response changes. By comparing the location of different cells in phase-space to each other and the separatrix, we can evaluate how differences in species concentrations affect differential cell behavior. It is

informative to note that the location of a cell in phase- or concentration-space affects how the network reacts to signals. For example, consider two cells in the pro-apoptotic section of phase-space that have different XIAP concentrations (as indicated in Figure 3-4B). The purple and red starred cells are close to and far from the separatrix, respectively. The red starred cell requires an eight-fold increase in XIAP concentration to cross the separatrix (to reach the green star) while the purple starred cell needs a modest two-fold increase. Alternatively, the red starred cell could move to the separatrix by increasing its XIAP concentration six-fold while decreasing its active caspase-8 concentration by one half (orange star). If the XIAP concentration is increased four-fold in both cells, the cells will behave differently and only the purple starred cell will cross the separatrix to survive. This simple example illustrates that we need to know the cell's state (key species concentrations) before predicting response. The DLE-defined separatrix helps us understand how cells in different states can have disparate responses to the same stimulation or perturbation.

3.3.3 A steady-state analysis cannot distinguish pro- and anti-apoptotic responses across phase-space

Direct analysis of the set of nonlinear algebraic equations representing our model at steady-state showed that the system has four types of equilibria (*i.e.*, four invariant manifolds filled with fixed points, in contrast to four fixed points) with only one type being stable (Figure 3-5A, Appendices Section 6.2). These stable fixed points can have non-zero valued concentrations of caspase-8 and XIAP. However, the concentration of caspase-3 must be zero because any inactive caspase-3 would be activated by caspase-8

and subsequently degraded by XIAP before a steady-state is reached. The phase-space locations of these stable fixed points are dependent on initial conditions.

To investigate whether these stable steady-states segregate into pro- and anti-apoptotic clusters, we plotted the steady-state locations from small subsets of trajectories. Figures 3-5B-D show active and inactive caspase-8 equilibrium concentrations from different small sets of trajectories. Within each set, the initial conditions of inactive caspase-8 were constant and most steady-states cluster into death or survival locales. For example, cells that survive stimulation with a death stimulus generally have low active and high inactive caspase-8 concentrations because caspase-3 was not activated enough to convert most of the inactive caspase-8 to the active form. This suggests that within a small set of initial conditions, a separatrix can be identified by plotting stable fixed points.

However, when we plotted trajectories from a broader range of initial concentrations of caspase-8, the ability to distinguish cell fate based on steady-state locations is lost (Figure 3-5E). In contrast, DLEs can separate the two fates without considering steady-state values. We have seen in Figure 3-4 that large DLEs can define a separatrix over a broad set of initial conditions. For the small sets described above, equilibria between the clusters have large DLEs and separate the groups representing surviving and dying cells (Figure 3-5B-D). We conclude that DLEs are versatile and can be applied regardless of whether or not steady-states cluster by behavior (Figure 3-5F).

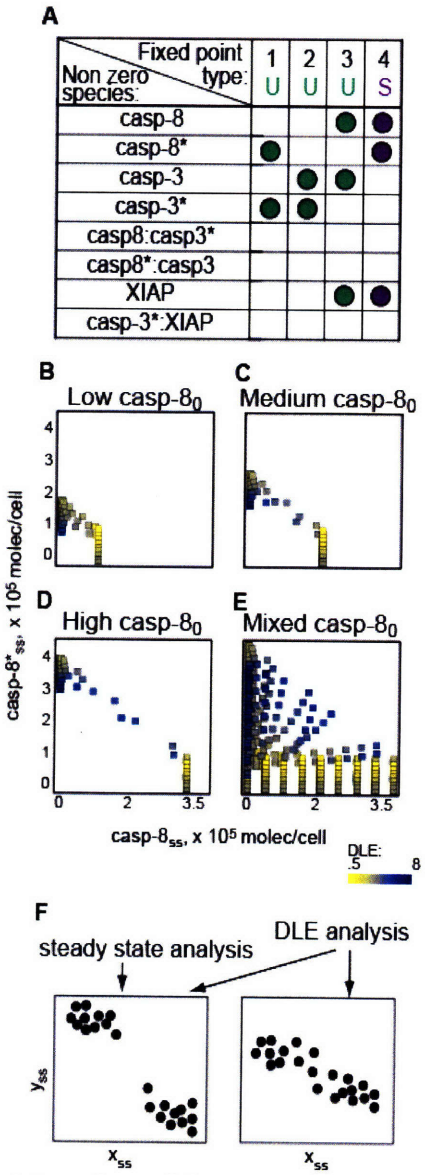

Figure 3-5 Stability and steady-state analyses of the caspase-3 activation network model.
(A) Stability analysis shows one stable (purple) and three unstable (green) types of fixed points (Appendices Section 6.2). Every type of fixed point requires concentrations of zero for the intermediate complexes. For each of the four fixed point types, there are two or three species that can be nonzero. The green (unstable) and purple (stable) circles indicate which species can be nonzero for each type of fixed point.
(B-E) The steady-state locations in the caspase-3 activation network are not globally clustered. The fixed points are plotted in the subspace containing active and inactive caspase-8, with increasing initial concentrations of inactive caspase-8: (B) 8.8 x 10^4, (C) 18 x 10^5, and (D) 3.5 x 10^5 molecules/cell. Other initial conditions were 2.6 x 10^5 molecules/cell of inactive caspase-3, 1 x 10^2 molecules/cell of active caspase-3 and the intermediate complexes, and 1 x 10^2 – 1 x 10^5 molecules/cell for active caspase-8 and XIAP. For each initial concentration of inactive caspase-8 (B-D), the steady-states are moderately clustered and are segregated by large DLEs (blue). However, the fixed points from different inactive caspase-8 initial conditions do not cluster when plotted together (E).
(F) A schematic compares the use of steady-state and DLE analysis methods. In systems where steady-states localize to different regions of phase-space (left), steady-state analysis methods may be used to

characterize the phenotypic behavior of the network. DLE analysis can distinguish between behaviors in networks regardless of fixed point clustering.

3.4 Discussion

Our goal here is to develop an analysis methodology for differential equation models aimed at understanding how transient signals influence phenotypic responses – *i.e.*, to develop signal-response relationships for most transient response networks in higher cells. Many signal transduction networks are transient response networks, meaning that they affect phenotypic cell responses before a steady-state is reached. Therefore, the steady-state and bifurcation analysis methods traditionally used to study differential equation-based models do not find straightforward application to transient response networks. To successfully analyze complex networks, we required that our methodology be applicable to transient signals across multiple dimensions.

Towards this challenging goal, we have described the use of direct finite-time Lyapunov exponents to study differential equation models of transient response networks. DLEs measure the separation between initially nearby trajectories in phase-space. We have used DLEs to identify sensitive regions of phase-space where small changes in the initial concentrations of network species alter cell fate (Figure 3-2). The separation can be calculated at any specific point in time, permitting prior biological knowledge concerning the most relevant experimental measurements to be leveraged. DLEs enable an exhaustive, multidimensional analysis of transient signals because they measure trajectory separation with respect to each dimension across the entire phase-space. As a result, DLEs are capable of identifying both important network interactions and in what context they affect signaling (*i.e.*, at what time or under which sets of initial conditions). By searching phase-space for sensitive initial conditions (those with large

DLEs), we can identify surfaces (separatrices) that separate different classes of signals. A separatrix specifies critical combinations of species concentrations around which signaling changes qualitatively. Because we can visualize the separatrix in different regions of phase-space, DLE analysis enables us to quantitatively interpret complex signaling interactions.

In applying DLE analysis to other biological signaling networks, a few considerations must be explored. DLE analysis is a numerical method which is flexible in the grid resolution and finite-times chosen for evaluation. While this flexibility is an asset for studying biological systems which have different time scales and varying parameter sensitivities, crude choices of time and phase-space grid may not capture all separatrices of interest. Because of the continuous dependence of trajectories on initial conditions, however, the DLE computation is a convergent procedure: refined grids and longer integration times are guaranteed to capture all separatrices. A second consideration is the relative strength of rates at which trajectories diverge at different locations in phase-space. Large rates of divergence will dominate the calculations, possibly obscuring smaller but biologically important trajectory separations. Therefore, it is important to select visualization methods that identify local features of the DLE field efficiently, thereby ensuring that all key behaviors are illuminated.

As a particular example of current biological interest, we applied DLE analysis to a model of caspase-3 activation involving caspase-8 and XIAP. The model responds to a pro-death stimulus with a transient signal leading to either death or survival. This network is an example of a transient response network: it has only one type of stable steady-state and the survival-vs-death decision is made before this steady-state is reached.

This notion of transient response signaling in apoptosis differs from some previously published models, which have cast this phenomenon as a multiple steady-state problem and analyzed it accordingly [132, 133]. Although some insights concerning model parameter effects were gained in those contributions, recent experimental studies focused on dynamic and integrative measurement have demonstrated that the key signals governing the phenotypic outcome of cell death-vs-survival are transient [43, 58]. Before stimulation, this network rests at a basal steady-state. Upon stimulation, a transient signal is produced during which the life-vs-death outcome is decided. Cells that survive return to the basal state. Thus, all key physiological signaling occurs during the transient phase.

While our model describes only a subset of the complex network regulating caspase-3, the model has eight species and is too complex to comprehensively characterize by inspection or parameter sensitivity analysis. Because DLE analysis is time-dependent and multivariate, we were able to gain specific insights about the regulation of caspase-3 that most likely would have been overlooked by inspection, single-parameter sensitivity analysis, or steady-state analysis (Figure 3-5F). Large DLEs defined a separatrix, from which we were able to gain quantitative, multivariate insight into the death-vs-survival decision. The separatrix classified two types of transient signals and defined the conditions leading to apoptosis and survival (Figure 3-4). We observed that the shape of the separatrix is not a simple plane and its shape and slope are dependent on rate constants. This suggests that in cases where reactions rates are hard to measure, the constant could be fit by comparing an experimentally identified separatrix with computationally predicted separatrices.

We envision DLE analysis as a tool for addressing challenging practical problems such as understanding the role of cell population heterogeneity in disease diagnosis and treatment. Others have described how population averages differ from the behavior of single cells by using population heterogeneity [125, 132]. DLE analysis can be used to investigate a key tangential question: How does population heterogeneity of protein expression correlate with different single-cell behaviors in a population of cells? To study the effects of noise and variability in protein expression within a population of cells, we can compare the concentration distributions of key proteins with separatrices. Intersections between these distributions and separatrices should correlate with heterogeneous responses. For example, when cells are treated with a saturating concentration of TNF, a death-inducing ligand, only approximately 60% of a population of HT-29 cells die [58]. While not understood in quantitative terms, the TNF receptor is known to activate both pro-survival and pro-apoptotic pathways. The pre-Death Inducing Signaling Complex (pre-DISC) activates the nuclear factor-κB (NF-κB) pathway (a pro-survival pathway which upregulates XIAP) before activating caspase-8 and the mitochondrial pathway. Activation of the mitochondrial pathway causes the mitochondria to release Smac, a pro-apoptotic protein which inhibits XIAP. It is likely that within a cell population, basal protein expression variation can affect network behavior by changing the concentrations of key regulatory proteins such as XIAP. In the future, the phase-space locations of HT-29 cells could be determined experimentally by measuring the distribution of caspase-3, caspase-8, and XIAP expression levels. By evaluating their proximities to the separatrix, we could determine if the distribution of protein expression levels in a cell population can cause a heterogeneous response to TNF

treatment. Eventually, we anticipate that DLE analysis can help us understand the transformation of a cell from a healthy to diseased state, and identify what changes in species concentrations are required to move the diseased cell across the separatrix to a healthier condition.

4 Quantitative Analysis of the Mitochondrial-pathway Requirement for Receptor-mediated Apoptosis

4.1 Introduction

It is generally thought that cells undergoing apoptosis can be classified into two cell types based on their dependency on the mitochondrial pathway: Type I cells are mitochondria-independent and Type II are mitochondria-dependent, Figure 4-1. The initial classification found that cell death occurred in both cell types at similar times after treatment with Fas but the activation of initiator and effector caspase was slower in Type II cells [16]. The control point that distinguishes the use of the two pathways is understood to be at the level of differential DISC formation triggering initiator caspase activation [139]. Type II cells are most commonly identified by protection from death-ligand induced apoptosis by Bcl2 overexpression or similar impairment of MOMP. Several additional descriptors to classify cells have been reported and include strong activation of death receptors and caspase-8 in Type I cells, differential sensitivity to different Fas ligand forms, and dependency on F-actin in Type I cells for receptor internalization [139, 140]. Recently, a panel of 58 tumor cell lines from the National Cancer Institute's libraries were classified, and Type I and Type II cells were found to have different gene expression patterns, though the molecular mechanism driving these changes have yet to be established [141].

While HeLa cells have been described as Type II because they are resistant to receptor-induced apoptosis when MOMP is impaired, we have observed partial caspase

activation in Bcl2 overexpressing HeLa cells that were partially depleted of XIAP [142]. Because XIAP depletion diminished the protection by Bcl2 overexpression to TRAIL-induced apoptosis, making them intermediate between Type I and Type II cells, we hypothesized that control of Type I vs. Type II may also occur at the level of effector caspases.

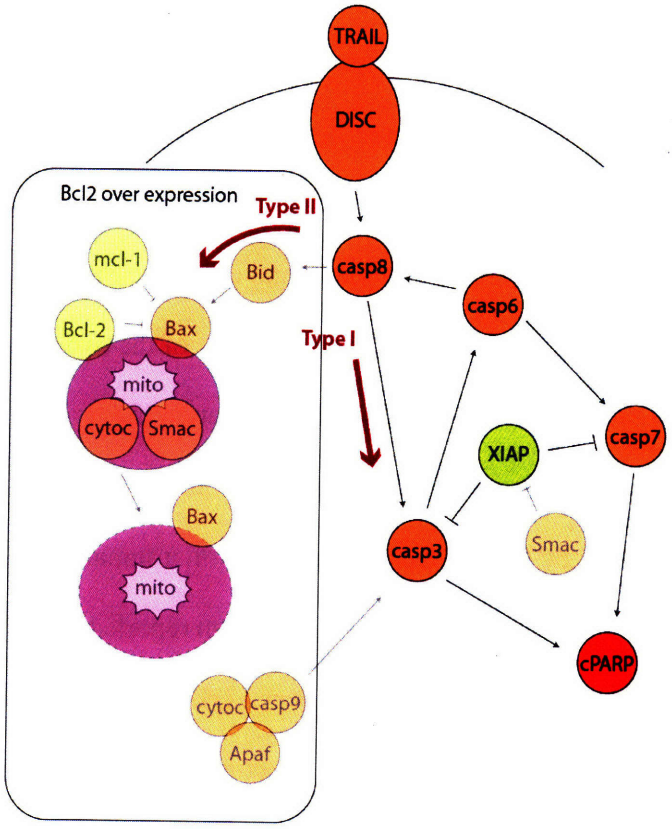

Figure 4-1 Pathways used in in Type I and Type II cells
Type I and Type II cells are distinguished by their dependence on the mitochondrial pathway to undergo apoptosis. Type II cells require the mitochondrial pathways and Bcl2 expression protects Type II cells from apoptosis. Type I cells do not require the mitochondrial pathway and activation of caspase-3 by caspase-8 is sufficient to trigger cell death. Proteins blocked by Bcl2 overexpression are faded.

To investigate the basis for Type I or Type II behaviors, we use a systems approach that combines kinetic modeling and detailed dynamic analysis with quantitative data of the concentrations and kinetics of proteins involved in this cell-decision network.

We perturb the ratios of caspase-3 to XIAP (and ubiquitin-ligase-mutant XIAP) and observe in single cells the kinetics of caspase-3 activity with flow cytometry and FRET-based reporters in live-cell microscopy. We combine our single-cell data with a Lyapunov exponent–based analysis of a physicochemical model of receptor-mediated apoptosis. We show that Type II cells behave as Type I cells following depletion of XIAP in Hct116 colon carcinoma cells. This supports our hypothesis that the control of Type I/Type II pathway usage can be controlled at the level of effector caspase activation. We use our data and computational modeling to define network conditions that yield Type I, Type II, and Type I/II intermediate behaviors. This characterization may provide a framework to identify characteristics of tumor types that will be susceptible to IAP-targeted cancer therapeutics.

4.2 Results

4.2.1 Modeling Type I vs. Type II responses

To explore the factors that differentiate Type I from Type II cells, a mathematical model of the signaling network that regulates caspase activity was analyzed (Figure 4-1). The differential equation model was built using mass-action kinetics to describe elementary reactions between network species (proteins, complexes, etc.) as described in the Section 4.4.1 and [77]. Our model was adapted from a 58-species model developed to describe apoptotic signaling events in HeLa human carcinoma cells following treatment with TRAIL and CHX [142, 143]. Because our experimental studies are based on Hct116, not HeLa cells, and focus on effector caspase activation, we updated several parameters in the model. We replaced the kinetic rate parameters used to describe

caspase-3 and XIAP interactions to the rates used in our smaller model of caspase-3 activation (Chapter 3). These association and dissociation rates were determined experimentally [21], and the ubiquitination rate was estimated (as discussed in Chapter 3). Futhermore, in the original model, active caspase-3 is actively degraded by XIAP-mediated ubiquitination. However, it has been recently reported that active caspase-3 is also targeted for degradation by other mechanisms [144]. In preliminary studies, we observed that about 80% of cleaved caspase-3 degradation is XIAP- or proteasome-independent in Hct116 cells (results not shown). We therefore increased the constitutive degradation rate of active caspase-3 by 5-fold. To match protein concentration estimates in Hct116 cells, the initial concentration for XIAP was reduced by 70% to 30,000 molecules per cell and that of caspase-3 was increased by 10-fold to 100,000 molecules per cell [K. Leitermann, S. Gaudet, and P. Sorger, unpublished observation].

With the model adapted for Hct116 cells, we next tested whether it could be used to exhibit both Type I and Type II behaviors. Simulation of the baseline model shows that PARP was cleaved with the characteristic all-or-nothing response (Figure 4-2). When the initial concentration of Bcl2 was increased 10-fold to simulate the experimental case of Bcl-2 overexpression, PARP cleavage was severely diminished. Because an increase in Bcl-2 initial condition protected PARP from being cleaved, the baseline model, like Hct116 cells, behaves in a Type II manner [141]. To test whether a Type I behavior could be observed with the same model, we increased the rates regulating DISC formation and activation of caspase-8 by the DISC by 10-fold (Figure 4-2 and Section 4.4.1, [145]). When the Hct116 model was simulated with both baseline and 10x Bcl2 initial concentrations, PARP was rapidly cleaved and the model therefore behaved as a

classical Type I network, in which increased DISC and initiator caspase activity can bypass the requirement for the mitochondrial pathway.

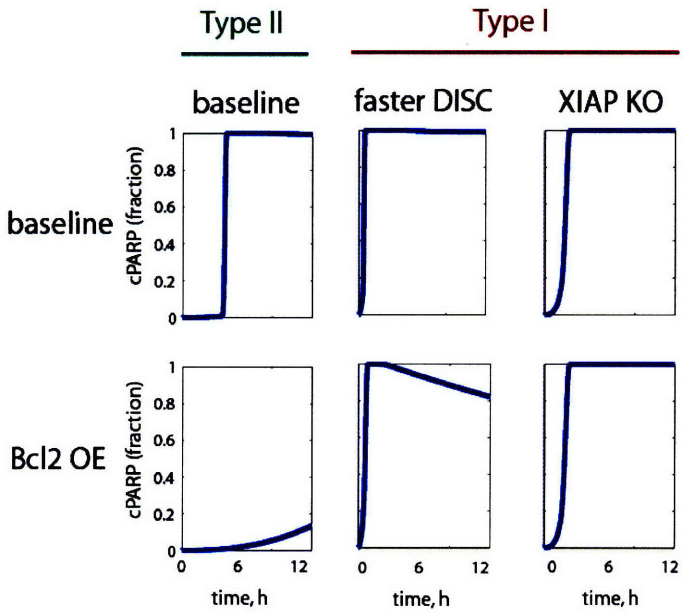

Figure 4-2 Predicted Type I and Type II behavior
Simulations of PARP cleavage are plotted under different network conditions for 50 ng/mL of TRAIL stimulation. The baseline case models Hct116 cells. Bcl2 over expression (modeled as a 10-fold increase in Bcl2 initial concentration) is protective against PARP cleavage for the Hct116 model, predicting Type II behavior in agreement with experimental data [141]. The model behaves as a Type I cell when parameterized for faster DISC activation (10-fold increases in rates of DISC assembly and activation of caspase-8 at the DISC, see Methods) or with XIAP KO (modeled with XIAP's initial concentration set to zero).

4.2.2 XIAP depletion converts Type II cells into Type I cells

Based on the observation that an intermediate Type I/Type II behavior was seen in XIAP knockdown HeLa cells, we next investigated whether XIAP plays a role in determining mitochondrial dependency in apoptosis. The significance of XIAP and its ubiquitinase activity in the apoptotic decision has been debated in the literature [146-150]. On one hand, XIAP has been shown to inhibit and ubiquitinate caspase-3 and caspase-9 in vitro and inhibition of XIAP by Smac mimetic small molecules has been shown to potentiate TRAIL-induced apoptosis [26, 150, 151]. On the other hand, XIAP

knockout mice survive to adulthood and exhibit no disease, arguing that it has little influence on the cell death decision [146]. We have previously observed that XIAP is critical in the death decision when the mitochondrial pathway is blocked; we observed a "partial death" phenotype in Bcl-2 overexpressing HeLa cells (Type II) that were partially depleted of XIAP by RNAi. These cells do not exhibit the characteristic snap-action caspase-activation, and some but not all of the PARP is cleaved in each cell [142]. Under Bcl-2 overexpression, caspase-3 is inhibited by XIAP and release of Smac from the mitochondria in blocked, eliminating an inhibitory mechanism of XIAP [151, 152]. From this, we believe that the conflict in the literature whether or not XIAP is key to cell death decision is likely due to the fact that the role of XIAP is context dependent. Together, our RNAi experiments and model analysis suggested that sensitivity to XIAP is dependent on both MOMP and XIAP [77, 142].

This is important because it implies that control of Type I vs. Type II may not occur only at the level of DISC formation and caspase-8 activation as described classically, but also at the level of *effector* caspase regulation. Because high concentrations of XIAP can hold the activity of caspase-3 in-check prior to MOMP, we predicted that XIAP depletion in some Type II cells should reverse the protection against apoptosis under Bcl-2 overexpression (similar to the observed behavior of Hct116 cells treated with Smac mimics and NSAIDs [152]). Simulations support this notion and demonstrate that depletion of XIAP converts the model from a Type II to a Type I behavior (Figure 4-2).

Another point of controversy surrounding the role of XIAP in apoptosis regulation is whether its ubiquitin ligase function is important. To establish whether the

apoptotic response in Type II cells was dependent on ubiquitination, we assayed caspase-3 cleavage and PARP cleave in Hct116 cells using flow cytometry at 2, 4, and 6 hours after treatment with CHX, TRAIL, and with and without the proteasome inhibitor MG132 (Figure 4-3A, Section 4.4). We used caspase-3 cleavage as a proxy for initiator caspase activity because caspase-3 is a substrate of the initiator caspase. Similarly, we used cleaved PARP as a proxy for effector caspase activation. The apoptotic state cells can be evaluated by plotting the two-color FACS data. In the lower left quadrant (little cleaved caspase-3 or PARP), cells were alive and did not have active caspases (Figure 4-3F). They progressed towards the death state of fully activated initiator and effector caspases (upper right quadrant in Figure 4-3F) through a transition state characterized by active initiator and inactive effector caspase activity (cells in the lower right quadrants in Figure 4-3F). In Hct116 cells, apoptosis progressed through the transition state as caspase-8 was activated between 2 and 4 hours following CHX+TRAIL treatment, and caspase-3 was activated in most cells by 4 hours. When co-treated with MG132, the dynamics of caspase-8 activation were unchanged but caspase-3 activation occurred much more rapidly (it is complete after 4 hours) and the transition state was not observed. This implied that caspase-3 activation was contemporaneous with caspase-8 activation. Hct116 Bax KO cells had similar patterns of caspase-8 activation to the parental line, but caspase-3 was inactive and the cells arrested in the transition state (Figure 4-3C). Confirming that Hct116s are Type II, blocking MOMP with Bax KO or Bcl2 OE protected the cells from receptor-induced apoptosis (Figure 4-3B). Protection against apoptosis was lost in Bax KO cells in the presence of MG132, and caspase-3 activation followed caspase-8 activity quickly (no transition state was observed, Figure 4-3B-C).

Significantly, these data suggest that Bcl2 protection against apoptosis in Type II cells is proteasome-dependent.

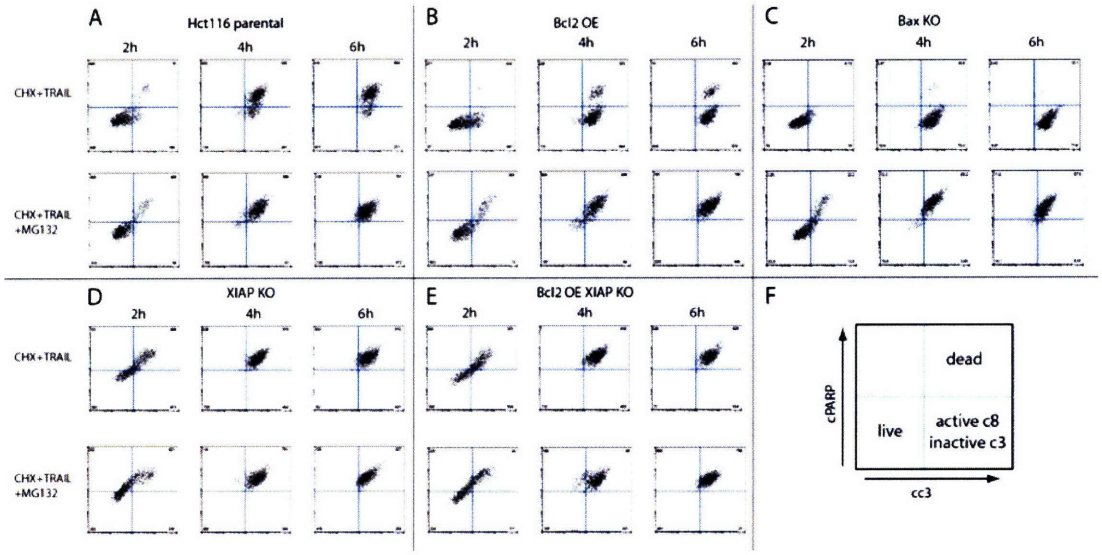

Figure 4-3 Single cell responses to CHX, TRAIL, and MG132
Hct116 derived cells were treated with 2.5 μg/mL of CHX + 50 ng/mL of TRAIL and 10 μM MG132, a proteasome inhibitor. A two-color FACs assay for cleaved caspase-3 and cleaved PARP measure initiator and effector caspase activity, respectively, in Hct116 (A) parental cells, (B) Bcl2 OE cells, (C) Bax KO cells, (D) XIAP KO cells, and (E) Bcl2 OE XIAP KO cells. (F) A schematic shows the two-colored FACS assay for initiator caspase activity (cc3) and effector caspase activity (cPARP). Bcl2 OE cells are from a pool and not from a single clone of 10x OE (as is shown in the rest of this chapter). Impairing MOMP through Bcl2 OE or Bax KO blocks death with TRAIL but not in the presence of MG132. Therefore, the Type II behavior is lost with MG-132 treatment. XIAP KO cells are not protected by Bcl2 OE and the response to CHX+TRAIL treatment is similar to MG132 treatment in XIAP +/+ cells.

Because MG132 treatment accelerated effector but not initiator caspase activation, we speculated that MG132 blocked the ability of XIAP to tag active caspase-3 for ubiquitination and subsequent degradation; XIAP is specific for effector caspases and not initiator caspases. To experimentally validate the influence our hypothesis on Type I vs Type II behavior, we produced Hct116 parental and XIAP KO cell lines that stably overexpress Bcl2 (Section 4.4.2). At a 10-fold overexpression level of Bcl2, MOMP was fully blocked (data not shown). When treated with CHX and TRAIL, the Bcl2 OE parental cells activated caspase-8 but PARP was not cleaved (Figure 4-3B). MG132

treatment in XIAP KO cells had mild effects, introducing a small population of cells that appeared to die with relatively low caspase-8 activity (Figure 4-3 bottom). Finally, the Bcl2 OE XIAP KO cells were unable to survive the CHX/TRAIL treatment and exhibited a Type I behavior, again showing the role of XIAP protein on the determination of Type I/II behavior (Figure 4-3E, [16]).

While flow cytometry analysis provides a picture of the state of many cells at different time points, it is difficult to derive precise information about signaling dynamics from these data. To further characterize the effects of MG132 and XIAP knockout on the dynamics of caspase-3 activity, we used a FRET-based reporter that measures effector caspase activity in live cells (described in Section 4.4.5). Briefly, with this reporter, higher FRET ratios indicate greater accumulation of cleaved product from effector caspase activity. The FRET ratios of individual cells were tracked and plotted in Figure 4-4. We observed that effector caspases in Bcl2 OE XIAP KO cells were activated suddenly with a very steep increase in FRET ratio ~75 minutes after treatment with either CHX+TRAIL or CHX+TRAIL+MG132. By contrast, Hct116 Bcl2 OE cells treated with CHX+TRAIL exhibited a slow and steady rate of effector caspase activity. Notably, the rate of caspase-3 activation was variable, which may be dependent on XIAP concentration; we speculate that Bcl2 OE cells with higher rates of caspase-3 activation have less XIAP than neighboring cells displaying less caspase-3 activity. Finally, the rapid increase in effector caspase activity was restored in Bcl2 OE cells with MG132 treatment, confirming the results obtained by flow cytometry showing that proteasome activity is required for Type II behavior.

To ensure that the switch from Type II to Type I behavior in XIAP KO cells was not an effect of compensation or adaptation to the knockout, we performed a complementation assay by transient transfection of mCherry-XIAP into 10x Bcl2 OE parental and XIAP KO Hct116 cells (Section 4.4.4). In Figure 4-5, the mCherry positive cells (in green) survived in the transition (active initiator caspase, inactive effector caspase) state while the mCherry negative cells died, confirming that change in XIAP concentration was solely responsible for the switch between Type I and Type II behaviors. In a parallel assay, we transfected the same cells with a ubiquitin ligase defective form of XIAP (mCherry-XIAPH467A). Because more ubiquitin ligase-deficient XIAP was needed to rescue the Bcl2 OE phenotype in XIAP KO cells (as compared to mCherry-XIAP, Figure 4-5, Section 4.4), we conclude that the mechanism of inhibition of caspase-3 by XIAP requires both competitive inhibition of substrate binding and ubiquitination.

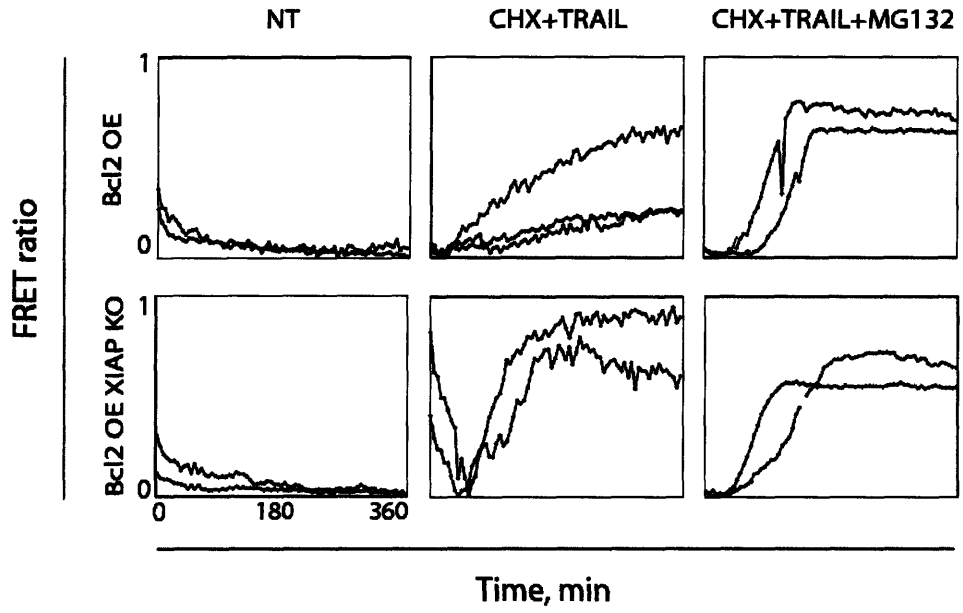

Figure 4-4 Dynamics of caspsae-3 activity
Live-cell microscopy with a FRET-based reporter for effector caspase activity was used to measure the dynamics of caspase-3 activity in response to NT (no treatment) or 2.5 μg/mL of CHX + 50 ng/mL of TRAIL with or without 10 μM MG132. The FRET ratio increases as caspase-3 is activated (Section 4.4). The Bcl2 OE cells are derived from a pool of selected transfectants and not a single clone and therefore the level of everexpression between cells is variable. Two cells are shown for each cell type and condition, except for Bcl2 OE cells treated with CHX+TRAIL for which three cells are shown. These cells lost the snap-action activation of caspase-3 compared to the parental line, but the rate of caspase-3 activation was variable, probably due to variation in protein concentrations of XIAP. Hct116 cells are highly motile and each curve is the time course of a tracked representative cell.

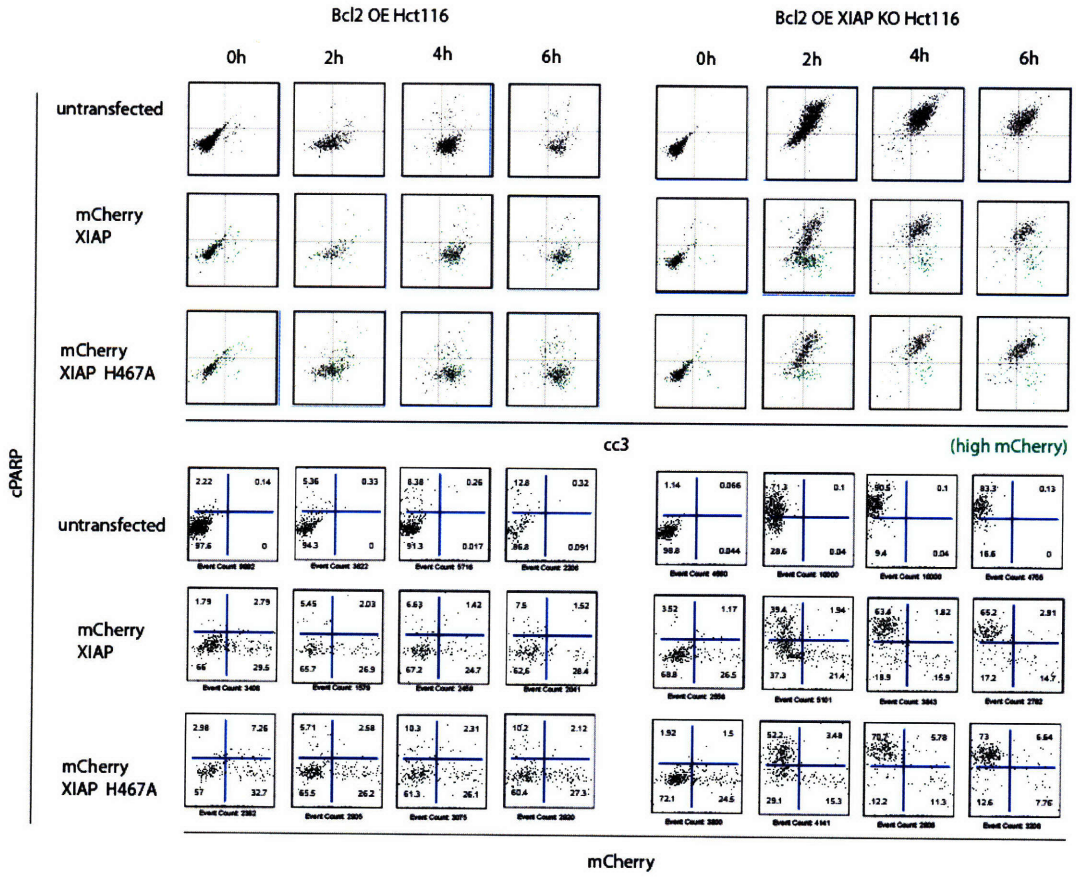

Figure 4-5 XIAP KO converts Type II Hct116 cells into Type I cells
The single cell response to CHX+TRAIL treatment is plotted for Bcl2 OE Hct116 and Bcl2 OE XIAP Hct116 cells. The cells were transiently transfected with mCherry-tagged XIAP or XIAP H467A (a RING-domain mutation that abolishes the E3 ubiquitintin ligase activity of XIAP). mCherry, initiator caspase activity (cc3), and effector caspase activity (cPARP) were measured by FACs and are plotted as cc3 vs cPARP (top) and mCherry vs cPARP (bottom). Cells expressing mCherry are were gates as shown in the bottom figures and labeled green in the top figures. XIAP KO cells are not protected by Bcl2 OE and therefore behave as Type I cells. Complementation with mCherry-XIAP restores the protection by Bcl2 OE (green). More XIAP H467A is required to restore Bcl2 OE protection than XIAP.

4.2.3 Continuum of Type I and Type II doses responses to TRAIL

Having identified two ways in which cells can become mitochondria independent or Type I, we next investigated whether the cell types could be differentiated based on their dose responses. Figure 4-6A depicts our initial prediction that all cells should behave similarly when treated with low concentrations of TRAIL, but the responses will gradually diverge at medium and high concentrations of TRAIL with MOMP-impaired

(such as Bcl2 OE) Type II cells dying only when stimulated with very high concentrations of TRAIL. The Hct116 model's dose response to 0, .0032, .016, .08, 0.4, 2, 10, 50, and 250 ng/mL of TRAIL at 8h shows no PARP cleavage in any cell type at low TRAIL concentrations. The model predicts that Type II (baseline) and Type I (XIAP KO and Bcl2 OE XIAP KO) cells die when confronted with moderate concentrations of TRAIL. These dose-responses were sigmoidal with a lower threshold for TRAIL sensitivity for XIAP KO cells (0.08 ng/mL) compared to the baseline case (2 ng/mL).

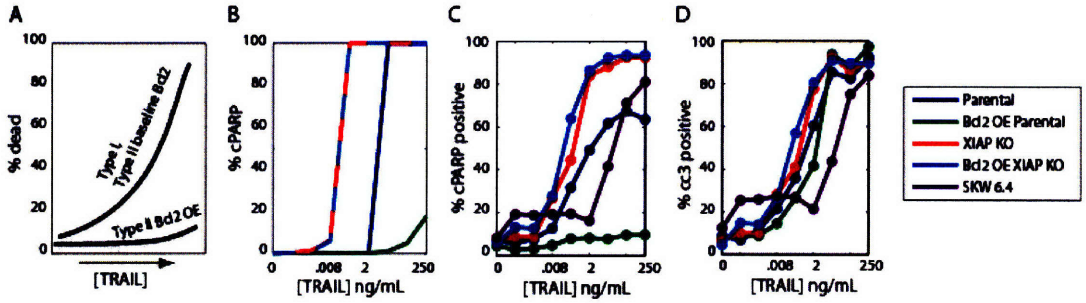

Figure 4-6 TRAIL dose response in Type I and Type II cells
(A) Hypothetical dose responses for Type I and Type II cells are depicted with MOMP-impaired Type II cells as outliers. (B-D) Dose responses to 0, 0.0032, 0.016, 0.08, 0.4, 2, 10, 50, 250 ng/mL of TRAIL + 2.5 μg/mL CHX at 8h. (B) Simulated cPARP dose responses for the Hct116-derived cell lines. (C-D) Dose responses for Type I and Type II Hct116 and SKW 6.4 (Type I) cells at 8h cell lines using a two-color FACS assay for initiator (D) and effector (C) caspase activity (see Methods). % positive is calculated by gating. The FACS plots with gating and dose response curves for all five cells at .5, 2, 4, and 8h with and without CHX can be found in the Appendix (Section 6.3.1). The dose responses were measured in two experiments and data from overlapping experiments were averaged in the curves above (see Appendix Section 6.3.1).

Initiator and effector caspase-activity was measured by FACS in response to varying doses responses of TRAIL in the four Hct116 cell lines (parental, Bcl2 OE, XIAP KO, and Bcl2 OE XIAP KO) and in SKW 6.4 cells, B lymphocytes that are prototypical Type I cells (Section 4.4,[16]). The FACS dot plots and derived dose response curves following 30m, 2h, 4h, and 8h treatments can be found in the Appendix (Section 6.3.1). Figure 4-6C shows the dose response curves as the percent of cells that have undergone PARP cleavage at 8 hours. However, the dose responses matched the model prediction

with XIAP and Bcl2 OE XIAP KO cells dying above TRAIL concentrations of 0.08 ng/mL. Similarly, the threshold for sensitivity of TRAIL was higher, ~2ng/mL, in parental Hct116 cells as predicted by the model. The dose response in the parental cells was also less sigmoidal, and fewer than 75% of the cells were cPARP positive at 8 hours after treatment with 250 ng/mL of TRAIL. As expected, the Bcl2 OE Hct116s were resistant to even high concentrations of TRAIL despite high caspase-8 activity (Figure 4-6D).

We predicted that the dose response for Type I cells would be easily distinguishable from the response of MOMP-impaired Type II cells. However, the SKW 6.4 dose response curve was dissimilar to curves from both Hct116 parental and XIAP KO cells. At TRAIL concentrations below 0.4 ng/mL, all five cell types were relatively insensitive to apoptosis, and Type I and Type II cells were indistinguishable. However, at moderate doses, it was evident that SKW 6.4 cells tolerated higher doses of TRAIL, dying above 10 ng/mL (Figure 4-6C). SKW6.4 cells thereby exhibited a dose response that fell in-between the expected dose responses predicted in Figure 4-6A-B and measured for Hct116-derived cells in Figure 4-6C (see also Figure 6-9). We conclude that Type I vs. Type II apoptotic behaviors cannot be simply categorized as Type I or Type II; instead, pathway-usage may be continuous with some cell types exhibiting intermediate behaviors that are difficult to classify distinctly as Type I or Type II.

Finally, because high caspase-8 activity at the DISC in Type I cells has been suggested to be the distinguishing factor between Type I and Type II cells [139, 141], we also measured the dose-response of total caspase-8 activity (not just at the DISC, Figure 4-6D). SKW 6.4 cells actually had a higher TRAIL threshold for caspase-8 activation as

compared to the Hct116-derived cells although DISC activation has been measured to be higher in SKW 6.4 cells [141]. Because we observed Type I behaviors in cells with lower thresholds for caspase-8 activity (XIAP KO Hct116 cells), measuring caspase-8 activation at the DISC may be insufficient for classifying cells, as caspase-8 does not have to be localized to the DISC to activate caspase-3. We also conclude that because SKW 6.4 and XIAP KO Hct116 cells are Type I yet exhibit different caspase-8 dynamics, increased activation of caspase-8 at the DISC is not a necessary condition for all Type I cells.

4.2.4 DLE analysis demarcates Type I, Type II, and variable regions in phase-space

To understand the multivariate conditions leading to Type I, Type II, or intermediate Type I/Type II behaviors, we analyzed the model using direct Lyapunov exponents ([77], Chapter 3, Section 4.4.6). DLEs measure local sensitivity to initial conditions relative to a finite time. High DLEs define a separatrix, which segregate phase-space into regions of different qualitative behavior, similar to a bifurcation diagram for steady-state systems. The model was subjected to a partial DLE analysis, varying initial conditions of caspsae-8, caspase-6, caspase-3, XIAP, and PARP (Section 4.4.6). The DLE analysis was performed with a 10-fold increase in Bcl2 concentration to isolate MOMP-impaired conditions (under baseline Bcl-2 conditions, there is no separatrix because all "cells" die, not shown). Figure 4-7 (top) shows the 6, 8, and 12h DLEs as a function of XIAP and caspase-3 concentrations. A clear separatrix (black) separates the phase-space into two regions based on XIAP and caspase-3 concentration. Above the separatrix (high caspase-3 and low XIAP concentrations) PARP was cleaved and these

cells were predicted to die despite the Bcl2 OE and are therefore Type I. Below the separatrix (low caspase-3 and high XIAP concentrations) PARP was not cleaved and these cells were predicted to be Type II. The separatrix tilted towards the XIAP axis with time (cells with a higher XIAP/caspase-3 ratio take longer to "die"). Because the separatrix moved with time, the area between the 6 and 12 hour separatrices defines a region in which the timing of apoptosis is variable and highly sensitive to initial concentrations of the network components. The stars indicate the phase-space locations of Bcl2 OE Hct116 (right) and Bcl2 OE XIAP KO Hct116 (left) cells. The Bcl2 OE cells are in the Type II region and the XIAP KO cells are near the separatrix but in the Type I region, as expected by our experimental observations.

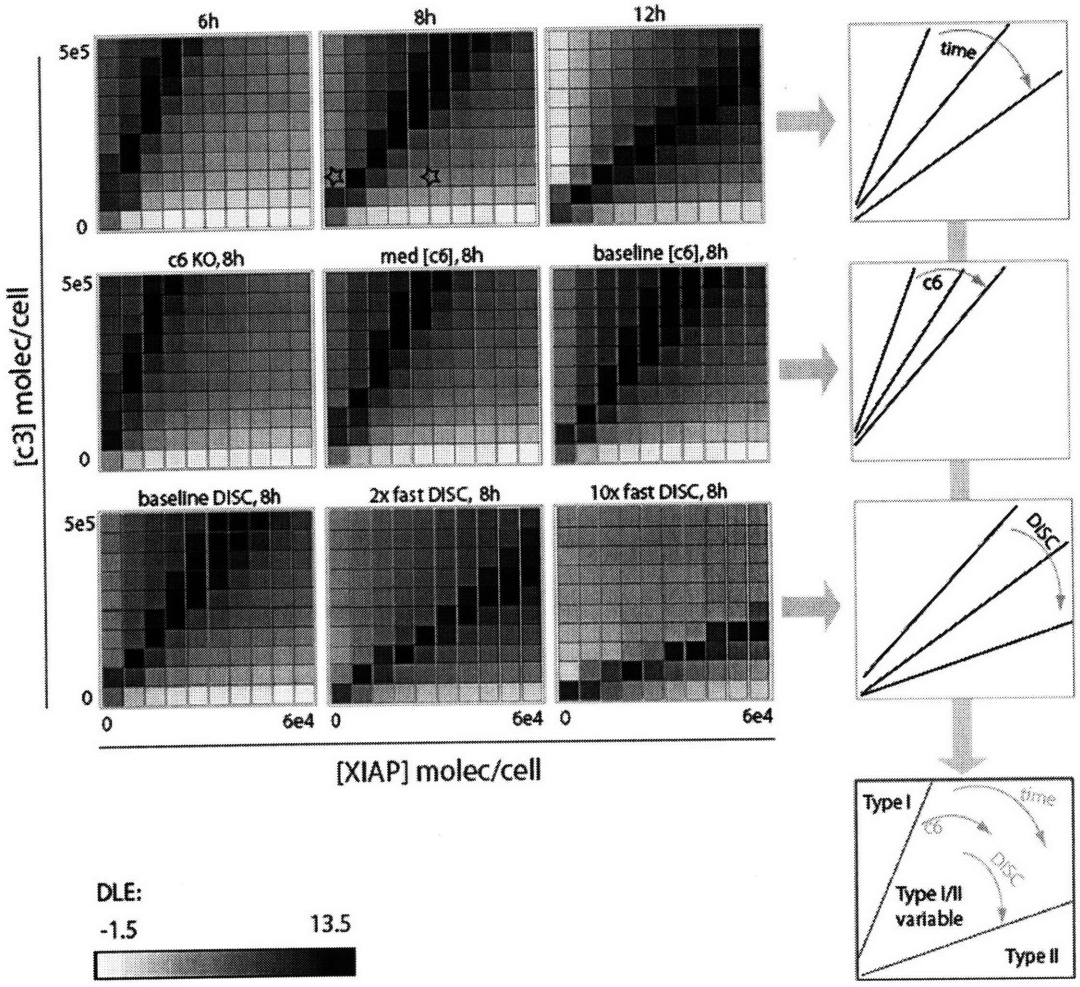

Figure 4-7 DLE analysis defines Type I ,Type II , and Type I/II variable conditions
A partial DLE analysis of the model shows a separatrix with Bcl2 OE (10-fold increase in Bcl2 initial concentration). Sensitive regions of phase-space have high DLEs (black) that form a separatrix, separating phase-space (plotted here in relation to XIAP and caspase-3 concentrations) into two regions. Above the separatrix, cells die and are Type I. Below the separatrix, cells die and are Type II. The two stars represent the phase-space locations of Bcl2 OE Hct116 cells (right) and Bcl2 OE XIAP KO cells (left). The separatrix tilts towards the XIAP axis with increasing time, caspase-6 concentration, and DISC activation rates, indicating that as these factors increase, a larger XIAP/caspase-3 ratio is tolerated for Type I cells. Together, the separatrices outline a variable Type I/II region which is sensitive to time, caspase-6 concentration, and DISC activation rates. In this variable region, cells are more likely to undergo partial PARP cleavage.

Caspase-6 amplifies activity in the caspase cascade as an intermediary in the positive feedback loop that activates caspase-8 via caspase-3 (Figure 4-1). Because apoptosis in Type I cells is dependent on caspase-3 activation by caspase-8, these cells are expected to be sensitive to caspase-6 expression. The DLE at different concentrations

of caspase-6 show that Type I cells with higher XIAP/caspase-3 ratios need more caspase-6 to remain Type I (Figure 4-7, middle). Accordingly, the separatrix tilted towards the XIAP axis as caspase-6 concentration was increased. As caspase-6 was increased, more phase-space was assigned to the Type I region and it became "easier" to be Type I. This analysis predicts that Type I cells are more sensitive to caspase-6 concentration than Type II cells but caspase-6 expression or activity is not necessary for all Type I cells.

The rate of DISC formation has been implicated as a distinguishing factor between Type I and Type II cells. In agreement, our model behaved as a Type I cell when the rates involved in DISC formation and caspase-8 activation at the DISC were increased 10-fold (Figure 4-2). To evaluate the role of the rate of DISC activation across a spectrum of initial concentrations, we computed DLEs at three rates of DISC formation and activation (Figure 4-7, bottom). As the rate increased, the separatrix swung towards the XIAP axis, expanding the Type I region at the expense of the Type II region, allowing cells with low XIAP/caspase-3 ratios to become Type I. As a corollary, high DISC activation rates were only necessary to achieve Type I behaviors when the XIAP/caspase was high. At moderate and high rates of DISC formation and activation, simulations at or near the separatrix stabilized with partial PARP cleavage and the separatrix location did not shift with time (not shown).

When collated together, the separatrices highlighted three regions: Type I, Type II, and a Type I/II variable region (Figure 4-7). In the variable region, cells are predicted to be more sensitive to network and stimulation conditions and have more variable death times. While caspase-8 activity is necessary for receptor-mediated apoptosis, DLE

analysis of the model did not show separatrix sensitivity to caspase-8. Instead, the separatrix sliced the phase-space into two regions according to caspase-3 and XIAP concentrations, consistent with our data showing that XIAP depletion can convert Type II cells into Type I cells. The existence of a variable region implies that Type I/Type II classifications are continuous, not discrete, and that the ratio of initial conditions of XIAP to caspase-3 is key in determining which pathways a cell requires for apoptosis. Consistent with the partial PARP cleavage arising in Bcl2 OE HeLa cells treated with RNAi against XIAP [142], we observed examples of partial caspase activation (and PARP cleavage) at initial conditions on separatricies defined by caspase-3 to XIAP ratios. The mapping of initial concentrations and caspase-8 activation rates at DISC to apoptotic responses using DLEs enables us to quantitatively evaluate the effects of network proteins for different cell lines that could be helpful in determining use-cases and combination therapeutics for TRAIL, Bcl2, and XIAP-targeted cancer drugs.

4.3 Discussion

To understand the regulation of Type I/Type II behavior, we used a systems approach that combines kinetic modeling and detailed dynamic analysis with quantitative data of the concentrations and activation kinetics of key proteins. In single cells, we perturbed the ratios of caspase-3 to XIAP (and ubiquitin-ligase-mutant XIAP) and observed the kinetics of caspase-3 activity with flow cytometry and FRET-based reporters in live cell microscopy. We measured the dose response of Hct116-derived cell lines and SKW 6.4 cells and found that loss of XIAP transformed Type II Hct116 cells into Type I cells that displayed caspase-8 and caspase-3 dynamics which differed in response to varying doses of TRAIL.

We combined our single-cell data with a Lyapunov exponent–based analysis of a physicochemical model of caspase-3 regulation to help understand this dynamical system. Our data and modeling suggest that there is a continuum of Type I/Type II behaviors and that control of Type I/II apoptosis can occur not only at the level of initiator caspase activation but at the regulation of effector caspase-activation. We identified three regions of phase-space that classify cell types within those regions as Type I, Type II, or Type I/II variable. Cell populations that are in the variable region are more likely to mixed apoptotic responses, varying with the strength of the pro-death cue (TRAIL concentration) and the population distributions of XIAP, caspase-3, caspase-6, and caspase-8 as well as the rate of caspase-8 activation.

By using a systems approach, our study identified a new control point for pathway usage in apoptosis. Because many tumor cells are sensitive to TRAIL treatment, understanding the multivariate conditions that confer TRAIL sensitivity and resistance has clinical relevance [153]. A quantitative identification of the conditions that lead to Type I or Type II behaviors could be used to identify appropriate therapies for different tumor types. Our analysis suggests that XIAP-inhibiting drugs (including Smac mimetics) should more broadly sensitize tumor cells to TRAIL as compared to Bcl2-targeted drugs (such as ABT-737) which affect only MOMP-protected Type II cells. [150, 152, 154, 155].

Apoptosis is typically characterized by activation of effector caspases which make a binary die-or-survive decision. A key feature of apoptosis is the rapid "all-or-nothing" activation of the caspases. Without this, cells with partial caspase activation may suffer DNA double strand breaks or other genomic instabilities, potentially leading to

oncogenesis. If caspases do not become fully active and the cell survives, these genomic instabilities can potentially lead to oncogenesis. Studies in Albeck et al. [142] and in this thesis bring light to how this switch-like mechanism operates and breaks down. XIAP is clearly an important regulator of caspase-3 activity, though the extent and mechanism of its interactions with caspase-3 and impact on apoptosis is under debate [26, 146, 156, 157]. Our study addresses the effect of XIAP/caspase-3 ratios on the extent of partial caspase activation. We observed different rates of effector caspase activation in Bcl2 OE Hct116 cells – it will be interesting to quantitatively investigate the relationship between XIAP concentration and caspase-3 activation. We found partial PARP cleavage in model simulations of initial conditions that map directly on the separatrix. Therefore, the separatrix not only delineates conditions leading to Type I and Type II behaviors, but also defines ratios of caspase-3 to XIAP that may result in partial caspase-activation. The Type I/II variable phase-space region is the most susceptible to partial-caspase activation because cells lying in this region are close to separatrix. Because it is rare to find cells that exhibit this "partial" death behavior, we hypothesize that most cell types tend to regulate their protein concentrations so that they are squarely in the Type I or Type II region and far from the variable region and the separatrix.

Interestingly, in the course of building the molecular tools to study the effects of XIAP expression levels and ubiquitinase activity, we have noticed that XIAP is extremely difficult to express and therefore appears to be under tight post-transcriptional regulation. We were surprisingly unable to express untagged-XIAP in cells other than 293T cells. Furthermore, the literature notably lacks documented examples of untagged XIAP expression in cells other than 293T cells. We observed that large tags at the N-

terminus of XIAP offered the best protection against XIAP degradation. Similar tight regulation of other key pro- and anti-apoptotic proteins to preserve set-points may play an important role in ensuring that cells make the correct apoptotic decision. It remains to be established whether the reported differential gene regulation in Type I and Type II cells contributes to stable differences in protein concentration between Type I and Type II cells [141]. Mapping the locations of several tumor and primary cell lines to the phase-space may help us to understand if cells gravitate away from the variable regions and to identify the proteins that are most tightly regulated in this process.

4.4 Materials and Methods

4.4.1 Physicochemical modeling of the apoptosis pathway

The apoptosis signaling model was built and run in Matlab 2007b using the ode15s solver. This model is a variant of a published model [142] and includes the major features of both the intrinsic and extrinsic pathways downstream of death receptor activation. DISC formation is modeled as an activated receptor following ligand binding. Caspase-8 is activated both at the DISC and by positive feedback from caspase-8 via caspase-6. Caspase-3 is activated by binding to active caspase-8 but its activity is inhibited by binding and ubiquitination by XIAP. Attenuation of caspase-8 activity occurs by competitive binding of FLIP to the DISC and binding of active caspase-8 with Bar. Crosstalk between the intrinsic and extrinsic pathways first occurs by cleavage of Bid (to tBid) by active caspase-8. tBid activates Bax and sequesters Bcl2, thereby changing the ratio of pro- and anti-apoptotic Bcl-2-family proteins at the mitochondria. Complexes of activated Bax at the mitochondrial outer membrane trigger MOMP and

subsequent release of cytochrome c and Smac. Cytochrome c forms the apoptosome in complex with Apaf-1 to activate caspase-9 and Smac then binds to XIAP and. The intrinsic and extrinsic pathways intersect again at the level of caspase-3 activation by both caspase-8 and caspase-9. The model contains PARP, a cleavage substrate of caspase-3. The model includes constitutive synthesis and degradation of all protein species. Because the model is compared to experiments performed in cells treated with CHX, the rate of protein synthesis is defined to be low. While the model does not account for spatial distribution of the species, transport reactions move species between the cell surface, cytoplasm, and mitochondrial outer-membrane space. We assume well mixed species within each compartment, see also [44].

The model was reparameterized from the version published for HeLa cells [142] to parameters better suited for Hct116 cells, as described in Section 4.2.1. The kinetic rate parameters for XIAP binding and ubiquitination of active caspase-3 are described in Chapter 3.2.1 and [77]. The constitutive degradation rate of active caspase-3 was increased 5-fold, consistent with experimental data (not shown). To match protein concentration estimates in Hct116 cells, the initial concentration for XIAP was reduced by 70% to 30,000 molecules per cell and for caspase-3 was increased 10-fold to 100,000 molecules per cell [K. Leitermann, S. Gaudet, P. Sorger, unpublished results].

4.4.2 Cell line derivation and maintenance

Hct116 Parental, Bax KO, and XIAP KO cells were gifts from B. Vogelstein and F. Bunz. Infection with a retrovirus containing puromycin resistant pBabe Bcl2 (a gift from Joan Brugge's lab) was used to generate Bcl2 OE. The cells were selected with 5 ug/mL of puromycin. For each cell line, a single colony that expressed 10-fold OE of

Bcl2 was expanded and used unless noted otherwise. Hct116-derived cell lines were maintained in McCoy's media supplemented with 50 units/mL penicillin/streptomycin, 2 mM L-glutamine, and 10% bovine calf serum. SKW 6.4 cells were obtained from ATCC and were maintained in RPMI supplemented with 50 units/mL penicillin/streptomycin, 2 mM L-glutamine, and 10% bovine calf serum. Three days prior to treatment, Hct116 cells were plated at 20,000 cells per well in a 24-well plate. Transient transfection of mCherry-XIAP and the FRET reporter was performed by standard methods with Fugene 6 (Roche) two days prior to treatment and the media was changed the next day. Treatments with TRAIL (SuperKiller TRAIL, Alexis Biochemicals), CHX (Sigma-Aldrich), and MG-132 (Calbiochem) were spiked into wells at a 20x concentrated mixture. SKW 6.4 cells were plated at a density of 400,000 cells/mL one day before the time course.

4.4.3 Flow cytometry assay for initiator and effector caspase activity

Following treatment, the floating cells were collected and adherent cells were trypsinized before undergoing a fixation first in 4% paraformaldehyde in PBS, followed by methanol. The cells were stored in methanol at -20°C for up to a week. Cells were washed with PBS + .1% Tween-20 and stained for 1 hour with custom Alexa Fluor 488-conjugated Anti-cleaved PARP (Asp214) monoclonal antibody (BD 624020) and PE-conjugated anti-cleaved caspase-3 antibody (BD 550914). Single antibody stained compensation controls were used to establish that compensation was not needed to distinguish gating for cleaved PARP and caspase-3 (not shown). FACS analysis was performed using the High Throughput Sampler on a BD LSRII instrument.

4.4.4 mCherry-XIAP constructs

pExchange-1-mCherry-XIAP and pExchange-1-mCherry-XIAPH467A were constructed by PCR (with the TaqPlus® Precision PCR System, Stratagene) of XIAP and XIAPH467 from pEBB-XIAP and pEBB-XIAPH467 obtained from Jon Ashwell (via Addgene.org). mCherry and the XIAPs were ligated into pExchange-1's multiple cloning site with Not1 (5'GCGGCGGCCGCGCCGCCATGGTGAGCAAGGGCGAGGAGGATAACATGGC C3') and BamH1 (5'GCGGGATCCGCCGCCATGGTGAGCAAGGGCGAGGAGGATAACATGGCC3') restriction sites used for mCherry and BamH1 (5'GGCCGGATCCGCCGCCATGACTTTTAACAGTTTTGAAGGATCTAAAACTTG TGTACCTGC3') and EcoRI (5'GGCCGAATTCTTAAGACATAAAAATTTTTTGCTTGAAAGTAATGACTGTGT AGCACATGGG 3') for XIAP.

4.4.5 Effector caspase FRET reporter

Construction and use of the effector caspase FRET reporter is described in Section 6.4. Cells were tracked by preprocessing the movies in ImageJ to generate a mask used by a tracking program in Matlab written by Khuloud Jaqaman and Gaudenz Danuser that was reparameterized to optimally track our Hct116 cells. Post-processing of the movies and tracking was performed in Matlab 2007a.

4.4.6 DLE computation

The partial DLE analysis was performed as described in chapter 3 but the phase-space region searched was limited to caspase3, caspase8, caspase-6, PARP, and XIAP. Bcl2 and the DISC activation rates (on-rate of DISC formation, on-rate of DISC activation, and the on-rate of caspase-8 binding to the active DISC) were variable as indicated in the text. Initial concentrations for PARP were explored only for 1,000,000 and 1,000,001 because we wanted to include PARP cleavage as a readout for death but did not intend to evaluate the model sensitivity to PARP concentration. The simulations and DLEs were computed in Matlab 2007b and were visualized in Spotfire. The code is available upon request.

5 Conclusions and Future Directions

5.1 Measuring and modeling intermediate signaling behaviors

The goal of this thesis was to arrive at a more complete understanding of the cell's death-vs-survival decision by combining quantitative measurement with mathematical modeling. In attempting both the experiments and the computational modeling and analysis, it became apparent that our current tools were insufficient to investigate the "intermediates" (in time and intensity) that pervade cell signaling. We therefore complemented our study of the cell death decision with the development of methods that enable us to study these "intermediates".

5.2 Fuzzy logic

A data compendium was gathered by my labmates that documents the multivariate signaling response in HT-29 colon carcinoma cells to combinations of saturating, intermediate, and low concentrations of TNF, EGF, and insulin. To interpret this complex dataset in the context of the vast knowledge of the pathways documented in the literature, we turned to logic-based modeling, which enables interpretable documentation of interactions when the network is too large (and unspecified) for ODE-based modeling. We found that while the literature was rife with "black and white" descriptions of pathway logic (e.g. activation vs inhibition, on vs off, high or low, apoptotic or pro-survival, etc.), our data was many shades of "gray". We therefore modeled the data using fuzzy logic, a mathematical formalism that enabled us to document and simulate the intermediate "gray" data. Because intermediates levels could be modeled, we were able to explore kinase pathway crosstalk downstream of three

cytokines and generate testable predictions about the co-regulation of MEK and MK2 and the inhibition of IKK signaling from EGF.

The next important step forward will be developing algorithms that can be used to automatically fit rule weights and membership functions. To do so, a metric must be designed that measures the goodness of fit between a model and data with penalties for model complexity. For example, is it preferable to use a discrete three-state model or a fuzzy two-state model? Measuring model complexity is also challenging and the difficulties in developing a metric that fairly penalizes different types of parameters is an open research question. Comparing discrete and fuzzy logic models may provide a powerful platform to address these questions as the problem contains a variety of parameters with very different scopes (membership thresholds, rule weights, degrees of fuzziness, number of memberships, etc.).

5.3 Transient signals and control of the apoptosis decision

We found that transient, intermediate signals played a key role in the apoptotic signaling network. To quantitatively investigate these pathways experimentally, we designed single cell assays to measure initiator and effector caspase activation in fixed cells and a FRET-reporter to measure effector caspase activity by live-cell microscopy. By using these assays, we found that the classification of cells as Type I or Type II based on their response to death ligand was not as clear-cut as is currently documented in the literature. We observed that knockout of XIAP from Type II cells converted the cells to Type I behavior. Our data contradicts the notion that the difference between Type I and Type II cells lies in rate of DISC formation. Instead, our data suggest that the dependency of cells on the mitochondrial pathway for apoptosis also relies on

downstream components in the signaling network, particularly on the ratio of effector caspases to XIAP.

We combined our experiments with physicochemical modeling of the apoptotic signaling network. We found that conventional methods for analyzing the model were insufficient because the relevant signals were transient, not steady-state. We developed a new methodology to study transient signals in physicochemical models using direct finite-time Lyapunov exponents (DLEs). The DLE analysis can identify separatrices which separate the phase-space into regions having common transient behaviors. Using this analysis, we outlined regions in phase-space for Type I, Type II, and Type I/II variable cells depending on the initial concentrations of XIAP, caspase-3, and caspase-6, and the DISC activation rate. In the Type I/II variable region, increasing caspase-6 concentration and DISC activation rates shifts the separatrix so that higher XIAP:caspase-3 ratios are permissible for Type I cells. Several improvements over the DLE analysis methodology can be made and include extending the analysis to rate parameters (perhaps by introducing place-holding state variables that are proportional to rates), visualizing not only the DLE values but the identity of the network species that contributes the most to the change, and scaling the gradients (used to compute the DLE) relative to the magnitude of each network species.

Our analysis, combined with dose response data in five cell lines, suggests that rather than discrete distinction between pathways, there is a continuum in the use of pathways in apoptosis and that there exists a "gray" area where cells sit near the boundary between Type I and Type II behaviors. In the gray region, cells are expected to be more likely to undergo partial caspase activation and are highly sensitive to small

changes in protein concentration in XIAP, caspase-3, and caspase-8. Our quantitative characterization of determinants of Type I/II behavior may be used to evaluate cases in which cancer therapeutics involving XIAP, TRAIL, and Bcl2 will be effective.

In searching for determining factors of Type I vs Type II apoptosis, we not only found that there was a continuum of "typeness" instead of a discrete classification, but that altering XIAP could convert Type II cells into Type I cells. DLE analysis of the model revealed that the ratio of XIAP and caspase-3 concentrations is key in determining whether a MOMP-impaired cell will undergo apoptosis after treatment with TRAIL. We are currently investigating this ratiometric control experimentally in the Bcl2 OE cells by measuring the dynamics of caspase-3 activation at different concentrations of XIAP, XIAPΔRING, and TRAIL.

5.4 Outlook

In this work, we developed new tools to explore signals in the key "gray" regions which have been overlooked in conventional studies. By applying these tools to the survival-vs-death decision, we elucidated crosstalk between kinase pathways and alternative control mechanisms in apoptotic pathway usage. Our studies highlight the need to further develop methodology to study intermediate levels of activity and time in protein signaling. We expect that the success of the systems biology approach will depend on its ability not only to handle dynamic, multivariate data but to interpret "gray" signals that act in concert to affect cell behavior.

6 Appendices

6.1 Supplementary materials for chapter 2

6.1.1 Regulation of IRS-1

IRS-1 is the canonical adapter protein downstream of the insulin receptor, though some of its many phosphorylation sites are also substrates of other receptor kinases, including EGFR [94]. In modeling IRS-1 phosphorylation at two sites, tyrosine 896 (IRS(Y)) and serine 636 (IRS(S)), we found that both were regulated by TNF and EGF but not by insulin (Figure 2-3F and 2-3J). While the FL gates for IRS(S) and IRS(Y) had the same input variables, the dissimilarity in logic rules revealed differential regulation of the two phosphorylation sites. Both TNF and EGF treatment positively affect S636 phosphorylation while TNF inhibits EGF-induced phosphorylation at Y896. As outlined previously [58], serine phosphorylation at 636 is understood to be downstream of insulin-Akt-mTOR signaling [158, 159]. Surprisingly, our model predicts that IRS(S) is unaffected by insulin treatment in HT-29 cells. Our prediction supports the hypothesis of Gaudet et al.: TNF and EGF induce serine 636 phosphorylation through mTOR, independent of insulin [58]. Further, Gaudet et al. hypothesize that TNF-mediated IRS phosphorylation at serine 636 inhibits EGF-mediated phosphorylation at tyrosine 896 [58]. In the FL gate for IRS(Y), TNF inhibits EGF-induced IRS(Y) activation, supporting this prediction.

6.1.2 ERK and Akt crosstalk

During the formulation of the Akt gate, we included inhibitory crosstalk from ERK to Akt because it has been observed in several experimental systems [95-97]. The introduction of crosstalk greatly simplified the rule-base of the Akt gate, suggesting that this crosstalk exists in the HT-29 cells (Figure 2-3I). The mechanism for this crosstalk is not understood in the literature, and our most effective model includes a short time delay from ERK to the Akt gate input. Negative crosstalk from the ERK to Akt pathways may be the mechanism by which TNF inhibits Akt phosphorylation upon insulin treatment, as observed by Gaudet et al. [58].

6.1.3 Supplementary figures

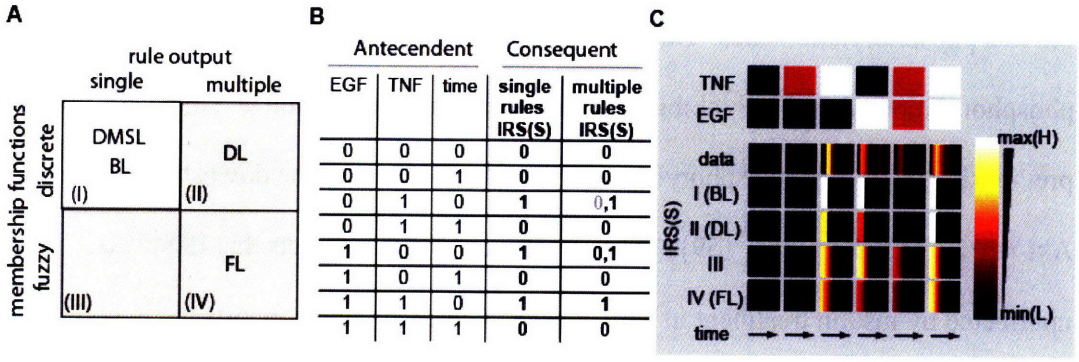

Figure 6-1 Differences between logic models
(A) A grid differentiates logic models based on differences in uniqueness of rules and degree of fuzziness in membership functions. Fuzzy logic (FL) models differ from Boolean logic (BL) and discrete multi-state logic (DMSL) models because the membership functions are fuzzy and the rule based need not be unique (e.g. more than one rule can fire for a given input state, even when membership to the input states is discrete). Discrete models (DL) and DMSL models both use discrete membership function but are different in that DL rule bases allow multiple rules to fire (rules are not unique). Roman numerals I-IV map the logic rules to figure (C). (B) The truth table for the IRS(S) gate described in Figure 2-2 is expanded to show the case where multiple rules can fire (DL and FL). IRS(S) output values are in bold. One value is gray to reflect its rule weight of 0.25. Where more than one output value is shown, both values result from conflicting firing rules and must be defuzzified. In this case, multiple rule firing results from non-unique rules (overlapping antecedents), not fuzziness in the membership functions. (C) Simulations of the IRS(S) across the spectrum of logic gate-types shown and labeled in (A) are shown with the experimental data (see Figure 2-5A for cytokine conditions).

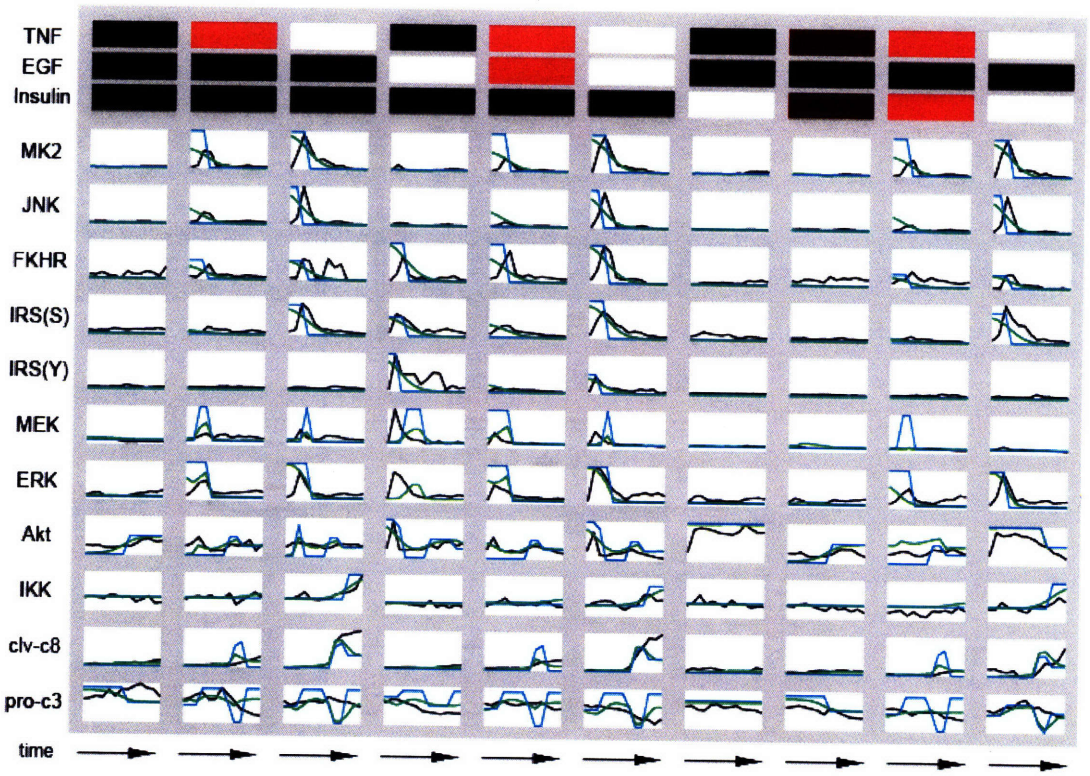

Figure 6-2 Non-heatmap representation of the data, FL, and DL models
Simulations from the FL model (green) and DL model (blue) are superimposed on the data (black). The layout and conditions are identical to Figure 2-5A.

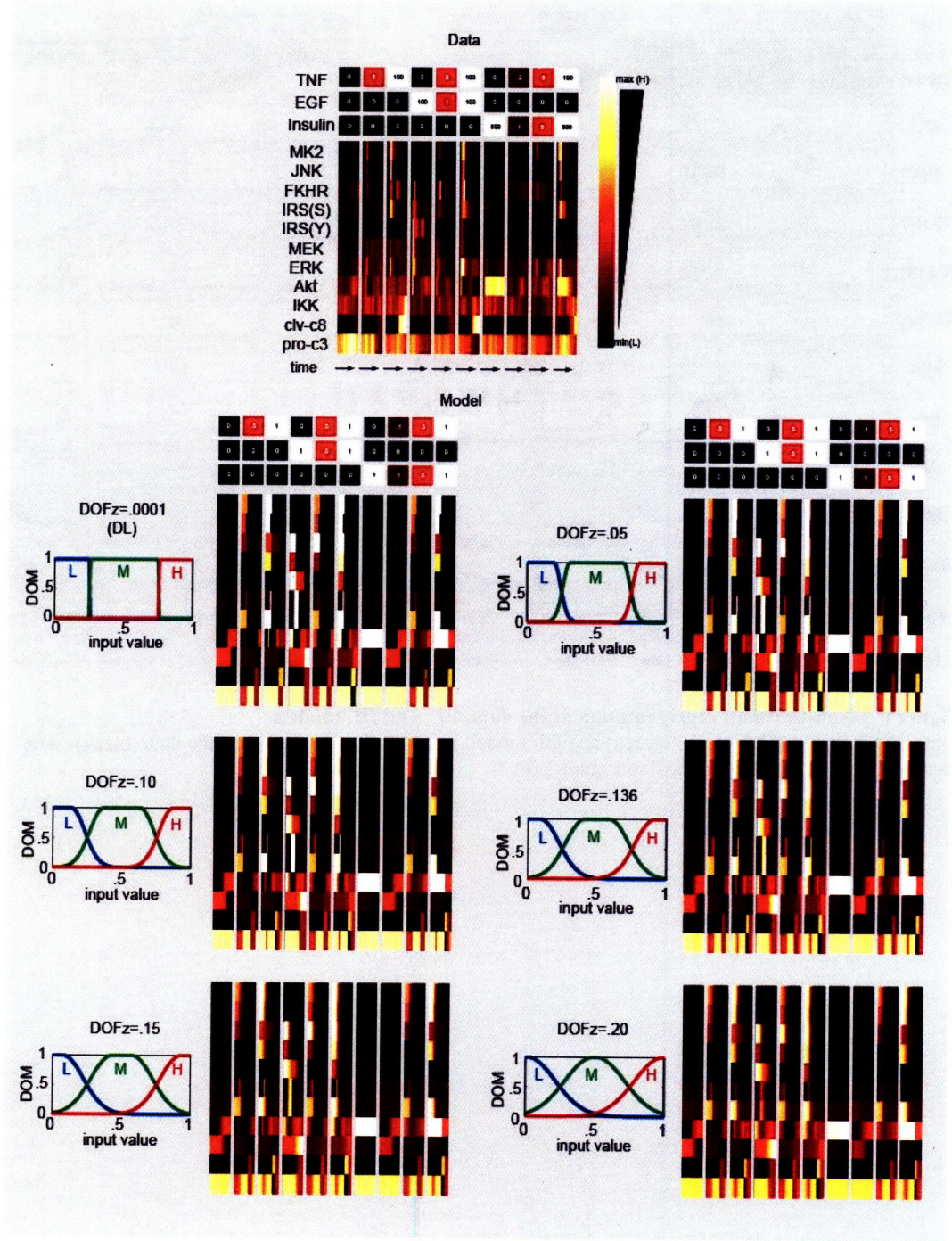

Figure 6-3 Degree of fuzziness in a default 3-state FL model

The FL gates described in the main text were built so that only 2-states (2 MFs) were used when possible. Here, the FL model was built by preferring 3-states per variable. Simulations from 3-state model are plotted (as compared to the data as shown in Figure 2-5A) for differing degrees of fuzziness [DOFz]. The discrete 3-state model is more able to reproduce the major feature of the data than the DL 2-state model (Figure 2-5A).

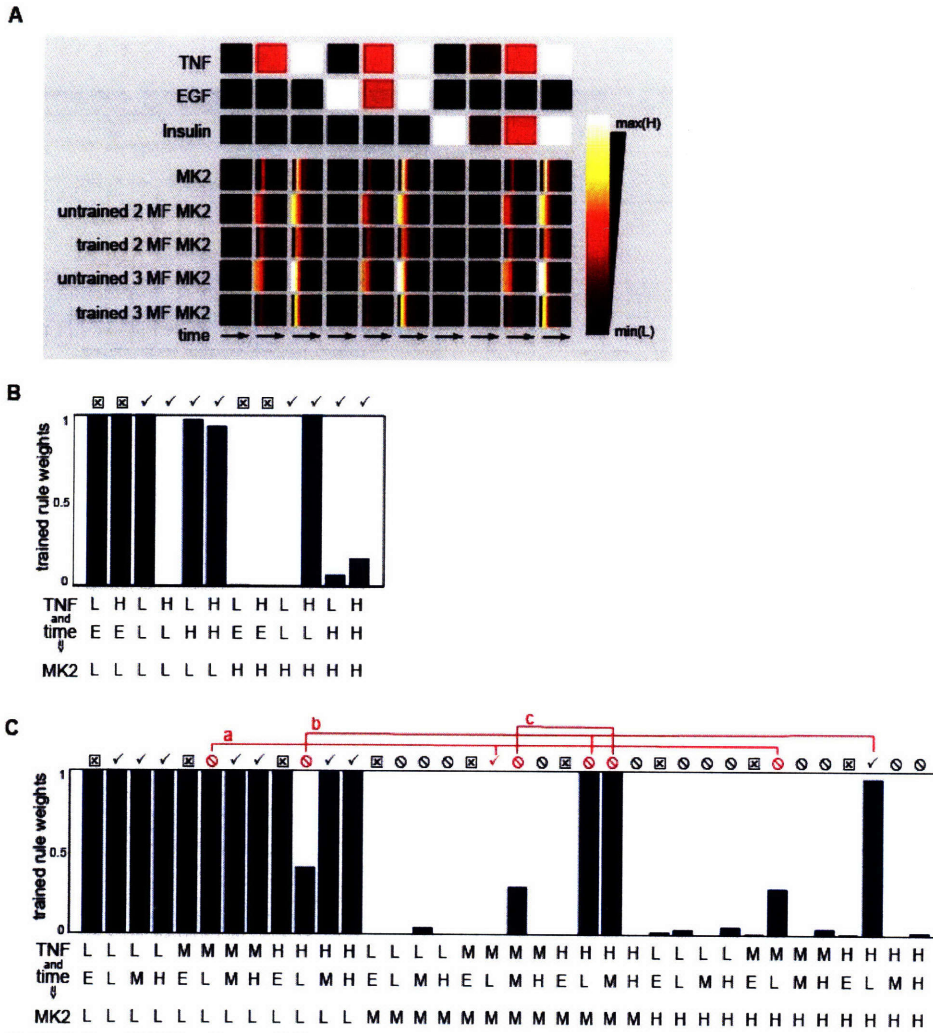

Figure 6-4 Fitting MK2 rules weights

(A) A heatmap depicts the data, trained and untrained model with 2 MFs (as described in the main text and Figure 2-6), and trained and untrained model with 3 MFs for MK2. (B) The fitted rule weights are plotted for the model with 2 MFs (see Figure 2-6). (C) The regressed rule weights are plotted for the 36 candidate rules. The rules are indicated in tabular format; the first two rows describe the state of the inputs, TNF and time, and the last row is the output MK2 state. L, M, and H represent low, medium, and high states, and E is the state describing the early response lag. Symbols above the plot show whether the rules were present (✓), absent (⊘), or not applicable (☒) in the untrained model. Rules that are different in the trained and the untrained model have red symbols.

To compare the optimized rule set with our empirically determined set, the bar graph of rule weights was annotated to indicate discrepancies (red symbols). Seven rules were found to be different, though the differences are easiest understood when grouped into three sets. The first set of rules ("a") involve the antecedent case "If TNF is M and time is L". In the untrained model, the output was M while in the trained model, the output was L and H (partial). Therefore, the logic for the trained and untrained model was essentially the same and yielded relatively similar results. In the second set of rules ("b") for the case "If TNF is H and time if L", the trained model includes additional outputs of M and L (partial) in addition to H, which is the only rule of the set in the untrained model. The third set of rules ("c"), "If TNF is H or M (partial) and time is M, then MK2 is M", was missed when the untrained model was built. In comparing the heatmaps of the trained to the untrained model when TNF is H or M and time is M, it is apparent that the untrained model erroneously omitted these rules (A) and the trained model's rules are improvements over the untrained model.

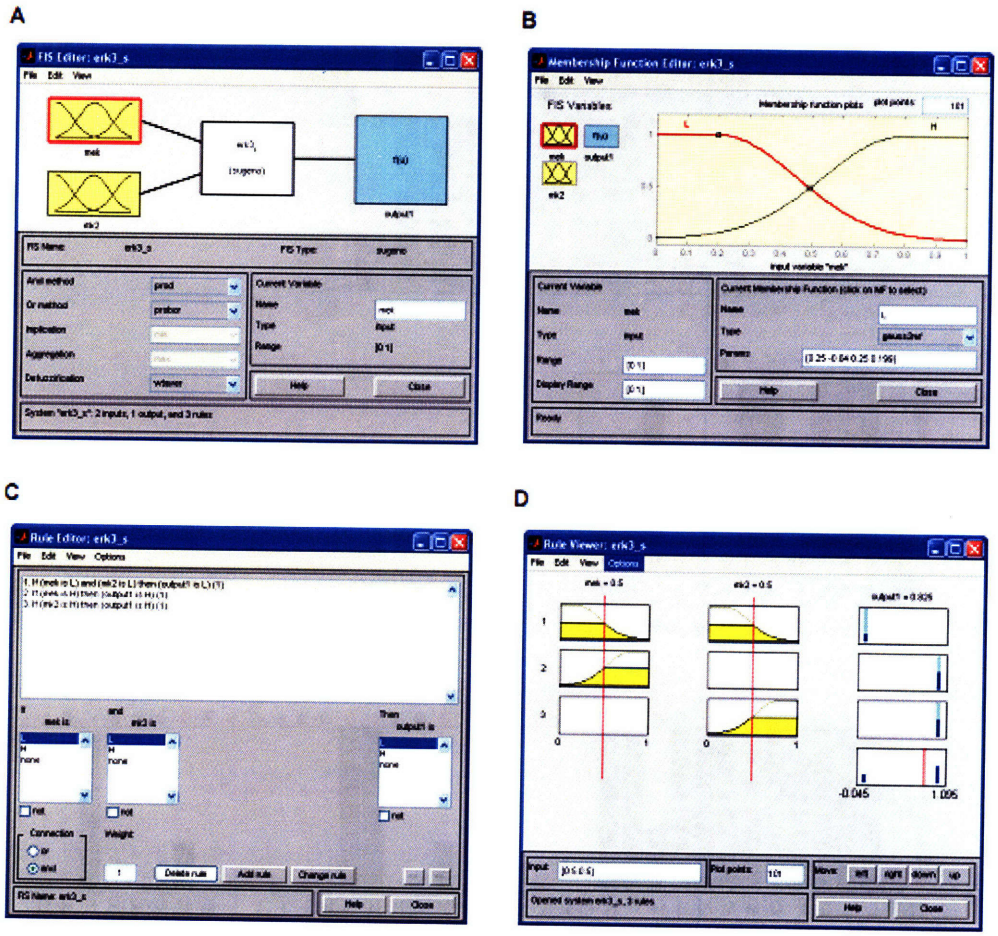

Figure 6-5 Screen shots illustrating FL gate construction
Screen shots depict the simple graphical user interface used to build the model in the Matlab Fuzzy Logic Toolbox. (A) In the gate set up window, input and output variables are declared. (B) The MFs can be changed graphically by choosing different shapes and altering the MF location and slope. (C-D) The rule editor and viewer is used to write and evaluate rules.

6.2 Supplementary materials for chapter 3

6.2.1 Fixed point criterion

To solve for the fixed points, we note that the listed rate parameters are nonzero. By definition of a fixed point, we set derivates of each species to zero:

$$0 = -k_1 x_4 x_1 + k_{d1} x_5 \quad (17)$$

$$0 = k_{d2} x_5 - k_3 x_2 x_3 + k_{d3} x_6 + k_{d4} x_6 \quad (18)$$

$$0 = -k_3 x_2 x_3 + k_{d3} x_6 \quad (19)$$

$$0 = k_{d4} x_6 - k_1 x_4 x_1 + k_{d1} x_5 - k_5 x_7 x_4 + k_{d5} x_8 + k_{d2} x_5 \quad (20)$$

$$0 = -k_{d2} x_5 + k_1 x_4 x_1 - k_{d1} x_5 \quad (21)$$

$$0 = -k_{d4} x_6 + k_3 x_2 x_3 - k_{d3} x_6 \quad (22)$$

$$0 = -k_5 x_7 x_4 + k_{d5} x_8 + k_{d6} x_8 \quad (23)$$

$$0 = k_5 x_7 x_4 - k_{d5} x_8 - k_{d6} x_8 \quad (24)$$

Substituting (17) into (21):

$$k_{d2} x_5 = 0 \Rightarrow x_5 = 0. \quad (25)$$

Substituting (19) and (25) into (18):

$$k_{d4} x_6 = 0 \Rightarrow x_6 = 0. \quad (26)$$

Substituting (25) into (17):

$$x_4 x_1 = 0. \quad (27)$$

Substituting (25), (26), and (27) into (20):

$$k_5 x_7 x_4 = k_{d5} x_8 \quad (28)$$

Rewriting (24):

$$k_5 x_7 x_4 = (k_{d5} + k_{d6}) x_8. \quad (29)$$

Comparing (28) and (29),

$$(k_{d5} + k_{d6}) x_8 = k_{d5} x_8 . \quad (30)$$

Because we have assumed that the rate constants are nonzero,

$$x_8 = 0 \quad (31)$$

Substituting (15) into (12)

$$x_7 x_4 = 0 \quad (32)$$

From equations (9), (10), (11), (15), and (16) we can derive steady-state conditions:

$$x_5 = x_6 = x_8 = 0 \quad (33)$$

$$x_4 OR(x_1 AND x_7) = 0, \quad (34)$$

$$x_2 OR x_3 = 0 \quad (35)$$

Together, these define conditions for the four types of fixed points in the system (Figure 3-5A).

6.2.2 Determination of stability

The stability of each type of fixed point (listed in Figure 3-5A) was deduced using conservation relations and type-specific steady state conditions (equations 33-35). This is convenient since traditional stability analysis would have been extremely difficult for this 8-dimensional system. At each fixed point, there are 2-4 zero eigenvalues, making stability analysis methods based on linearization inconclusive. The number of zero eigenvalues was determined symbolically using Maple 9 (Waterloo Maple Inc., Ontario, Canada).

- Fixed point type 1: All species must have zero concentrations except active caspse-8 and active caspase-3. Since XIAP concentration is zero (there is no turnover of XIAP in the model and XIAP is not initially present), active caspase-3 cannot form complexes with XIAP. Therefore, the concentration of caspase-3 and caspase-8 will not change. These fixed points are unstable because perturbations of XIAP concentrations to nonzero values send these trajectories to fixed point type 4.

  Biologically, these fixed points would represent cells signaling for death because all of the caspases are active. These fixed points are attracting in some directions because the pulse peaks approach these fixed points before declining towards fixed point type 4 (Figure 3-3). In comparing trajectories from above and below the

separatrix, we noticed that the peak of caspase-3 activation corresponds to this type of unstable fixed point. The height of the pulse corresponds with its width. For example, in Figure 3-3C, the active caspase-3 pulse is tall and wide while in Figure 3-3D, the pulse is short and narrow. The unstable fixed point is attracting in some directions; therefore, the closer the trajectory moves towards this unstable fixed point, the stronger the pro-apoptotic pull. This attraction to the unstable fixed point is what resulted in higher and wider active caspase-3 pulses.

We therefore defined a pulse metric to explore the relationship between the pulse and the network outcome. Since we hypothesized that the pulse magnitude and width corresponded with its proximity to these unstable fixed points, we defined a pulse metric as the shortest distance between the trajectory and fixed point 1. For the time courses shown in Figures 3-3A-B, the pulse metrics are 1.3×10^4 and 1.4×10^5 for low and high initial conditions of XIAP, respectively. In Figure 6-6, the pulse metric is plotted in the same phase-space slice displayed for the DLEs in Figure 3-4A. This metric divides the phase space similar to the separatrix defined by high DLEs. Above the separatrix, the pulse metric is small, indicating that those trajectories are strongly attracted to these fixed points. In being so strongly pulled away from the steady state by this unstable fixed point, these systems have made a death decision. For the initial conditions where the pulse metric is large (under the separatrix), the trajectories are far enough away from the unstable fixed point to avoid being pulled away from the steady state. As a result, caspase-3 is not strongly activated and these systems avoid apoptosis.

- Fixed point type 2: All species must have zero concentrations except caspase-3 and active caspase-3. Since there is no synthesis of caspase-8 and XIAP in this model any species containing a form of caspase-8 or XIAP (including all intermediates complexes) will be absent. These fixed points are unstable because perturbations of caspase-8 and XIAP concentrations to nonzero values send these trajectories to fixed point type 4. This type of fixed point would represent an extremely rare (or knock-out) cell with no caspase-8 or XIAP.
- Fixed point type 3: All species have zero concentrations except caspase-3, caspase-8, and XIAP. Since there are no active caspases, intermediate complexes cannot be formed. These fixed points are unstable because perturbations in the active caspases or intermediate complexes to nonzero values send these trajectories to fixed point type 4. Biologically, this type of fixed point represents a cell that has not received a death signal.
- Fixed point type 4: All species have zero concentrations except caspase-8, active caspase-8, and XIAP. This fixed point is the most general, and almost all biologically significant initial conditions will fall under this scenario: caspase-8 is converted into active caspase-8 while caspase-3 is converted into active caspase-3 until XIAP causes all of the active caspase-3 to be degraded. Given ample time, all of the caspase-3 in the system is degraded and nonzero concentrations for caspase-8, active caspase-8, and XIAP may remain. This type of fixed point is stable because under perturbations to the caspases, intermediate complexes, or XIAP, the network will return to this type of fixed point. Biologically, this type is fixed point would represent the state of the

network after it is responded (with a transient behavior) to a death-signal before the system is reset (not modeled here).

6.2.3 Caspase-3 activation model with protein turnover

Our model was simplified to by omitting protein synthesis and degradation. A similar analysis was performed with a model extended to include turnover and cleavage of XIAP by active caspase-3. This extended model yielded similar results to the simplified model (Figures 6-7 and 6-8). A constitutive degradation rate, k_{deg}, was assumed for all species; it was estimated as 4.63×10^{-5} (s^{-1}) using the half-life of pro-caspase-3 [160]. The synthesis rate was assumed to be the product of k_{deg} and the initial concentration of the protein for pro-caspase-3, pro-caspase-9, and XIAP. The model is specified below (equations 36-43). The rate of XIAP cleavage by active caspase-3, k_{clv}, is 5×10^{-6} (s^{-1}) [132]. Species numbers and non-turnover parameters are identical to the basic model described in Figure 3-1 and Table 3-1.

$$\dot{x}_1 = -k_1 x_4 x_1 + k_{d1} x_5 - k_{deg} x_1 + k_{deg} x_1(t=0) \quad (36)$$

$$\dot{x}_2 = k_{d2} x_5 - k_3 x_2 x_3 + k_{d3} x_6 + k_{d4} x_6 - k_{deg} x_2 \quad (37)$$

$$\dot{x}_3 = -k_3 x_2 x_3 + k_{d3} x_6 - k_{deg} * x_3 + k_{deg} x_3(t=0) \quad (38)$$

$$\dot{x}_4 = k_{d4} x_6 - k_1 x_4 x_1 + k_{d1} x_5 - k_5 x_7 x_4 + k_{d5} x_8 + k_{d2} x_5 - k_{deg} x_4 \quad (39)$$

$$\dot{x}_5 = -k_{d2} x_5 + k_1 x_4 x_1 - k_{d1} x_5 - k_{deg} x_5 \quad (40)$$

$$\dot{x}_6 = -k_{d4} x_6 + k_3 x_2 x_3 - k_{d3} x_6 - k_{deg} x_6 \quad (41)$$

$$\dot{x}_7 = -k_5 x_7 x_4 + k_{d5} x_8 + k_{d6} x_8 - k_{deg} x_7 - k_{clv} x_7 x_4 + k_{deg} x_7(t=0) \quad (42)$$

$$\dot{x}_8 = k_5 x_7 x_4 - k_{d5} x_8 - k_{d6} x_8 - k_{deg} x_8 \quad (43)$$

6.2.4 Supplementary figures

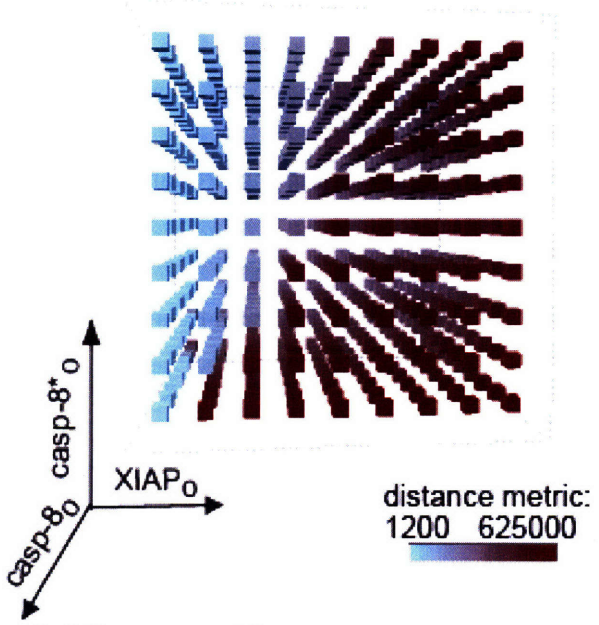

Figure 6-6 A distance metric defines a separatrix
A phase-space subplot of the distance metric (shortest distance to type 1 fixed points) is shown on a linear scale under the conditions shown for the DLE-defined separatrix in Figure 3-4A The separatrix matching the DLE-defined separatrix is between small (blue) and large (red) distances. The distance is large below the separatrix (survival) and small above the separatrix (death).

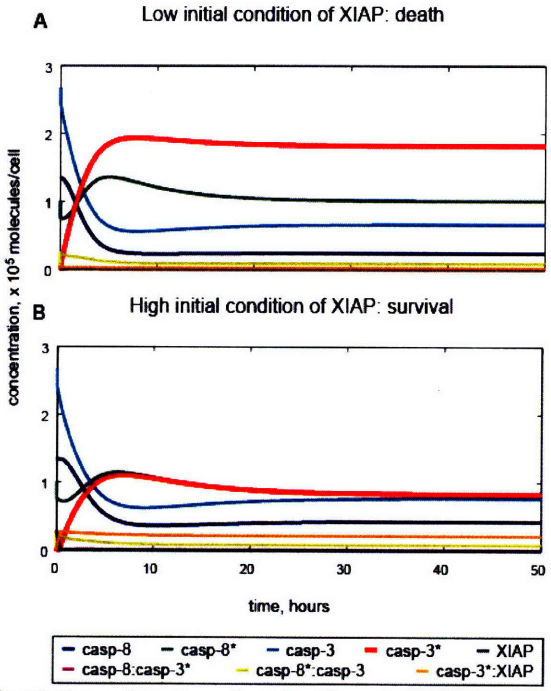

Figure 6-7 Time-course simulations show transient death and survival responses under two different initial conditions of XIAP when turnover is introduced to the model.
In these time courses, the initial conditions matched those in Figure 3-3A-B, respectively. Under a low initial concentration of XIAP (A), the transient caspase-3 pulse is taller and wider than the pulse under a higher initial concentration of XIAP.

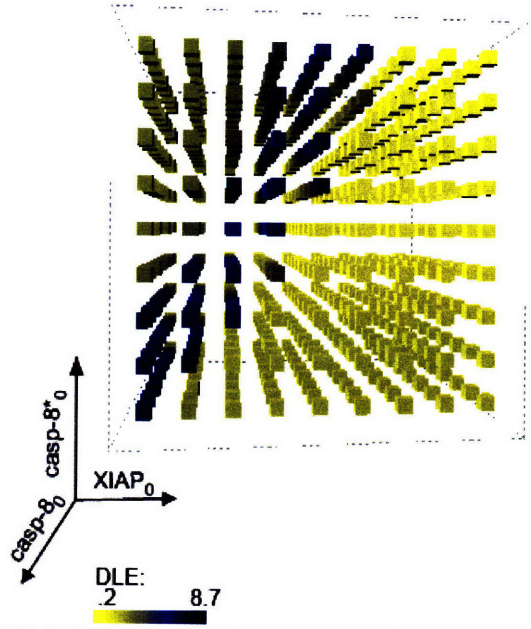

Figure 6-8 The six-hour DLE defines a separatrix separating phase-space into pro- and anti-apoptotic decisions in a model including turnover
The six-hour DLEs are plotted under the conditions in Figure 3-4A. The introduction of protein turnover to the caspase-3 activation model did not significantly change the shape or the location of the separatrix.

6.3 *Supplementary materials for chapter 4*

6.3.1 Supplementary figures

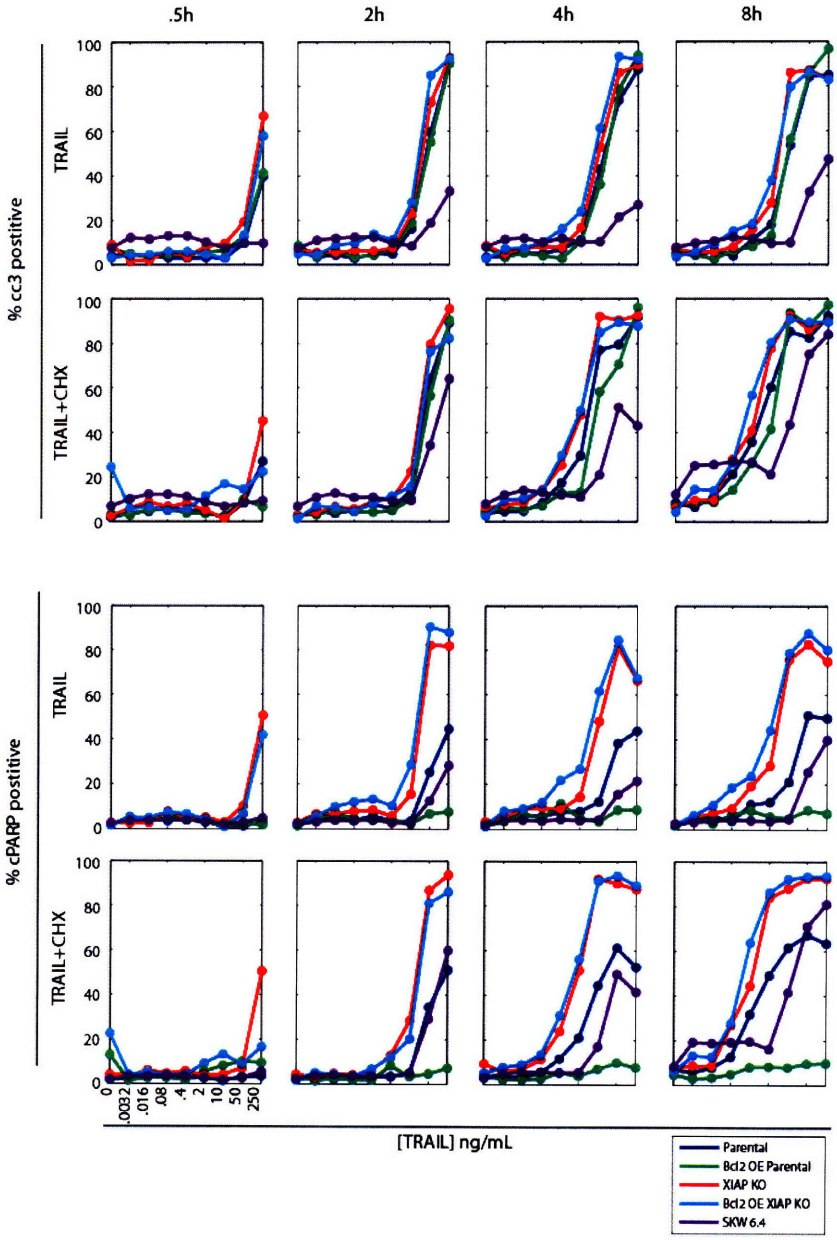

Figure 6-9 Dose response curves for cleaved caspase-3 and cleaved PARP at .5, 2, 4, and 8 h
Dose responses to 0, 0.0032, 0.016, 0.08, 0.4, 2, 10, 50, 250 ng/mL of TRAIL (and 2.5 μg/mL CHX as indicated) are plotted for the four Hct116 cell lines and SKW 6.4 as measured with the two-colored FACS assay for initiator and effector caspase activity (see Section 4.4.3). % positive cleaved caspase-3 (measuring initiator caspase activity) and cleaved PARP (measuring effector caspase activity) is calculated by gating (see Figures 6-10, 6-11, 6-12, 6-13, and 6-14). The dose responses were measured in two experiments (the sets are colored by dose in black and gray in Figures 6-10, 6-11, 6-12, 6-13, and 6-14) and data from overlapping experiments (2 and 50 ng/mL of TRAIL) were averaged in the curves above.

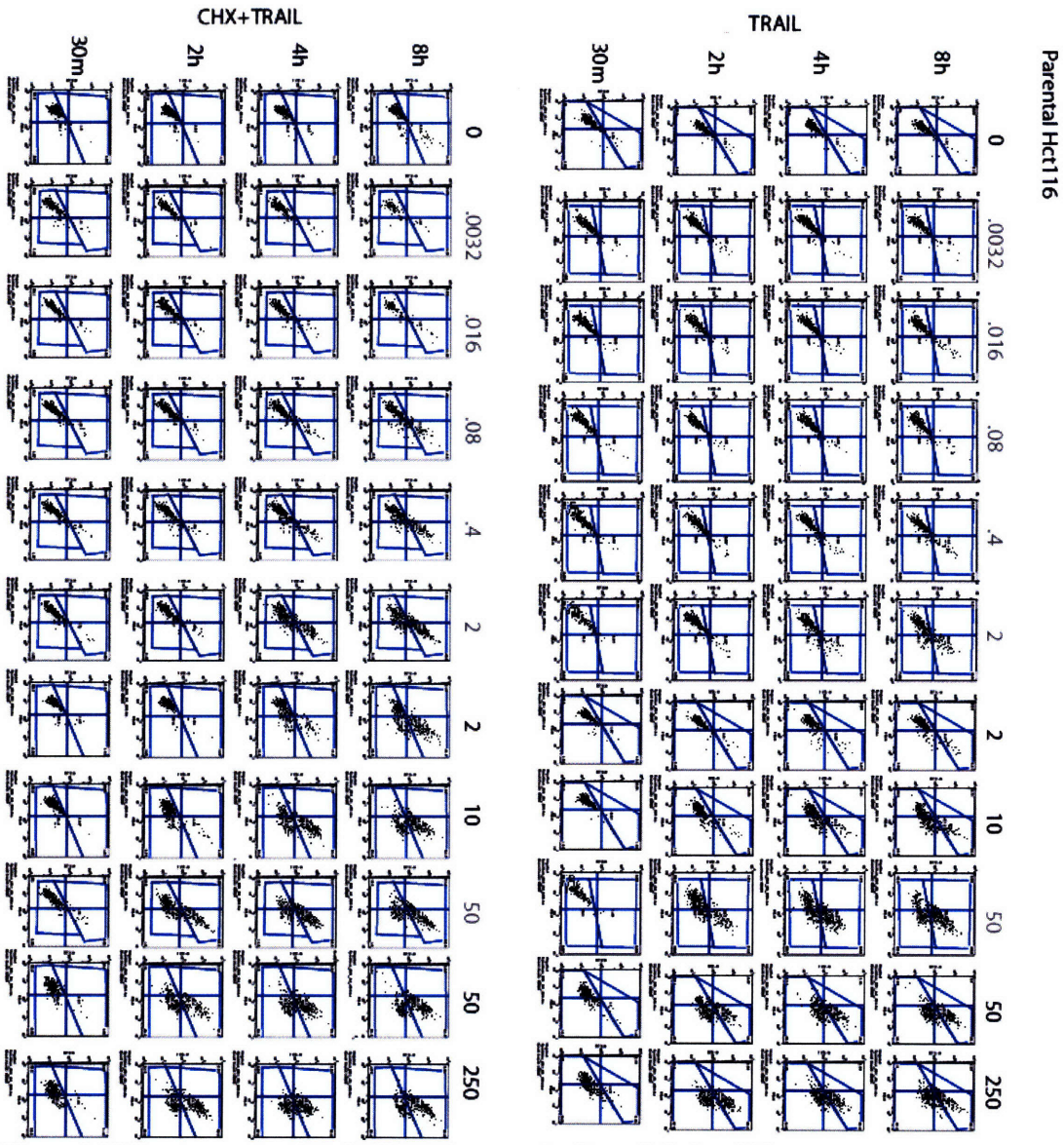

Figure 6-10 Dose response plots for Hct116 parental cells at .5, 2, 4 and 8h

Dose responses to 0, 0.0032, 0.016, 0.08, 0.4, 2, 10, 50, 250 ng/mL of TRAIL (and 2.5 μg/mL CHX as indicated) are plotted with the two-colored FACS assay for initiator and effector caspase activity (see Section 4.4.3). The measurements were made in two experiments (the sets are colored by dose in black and gray).

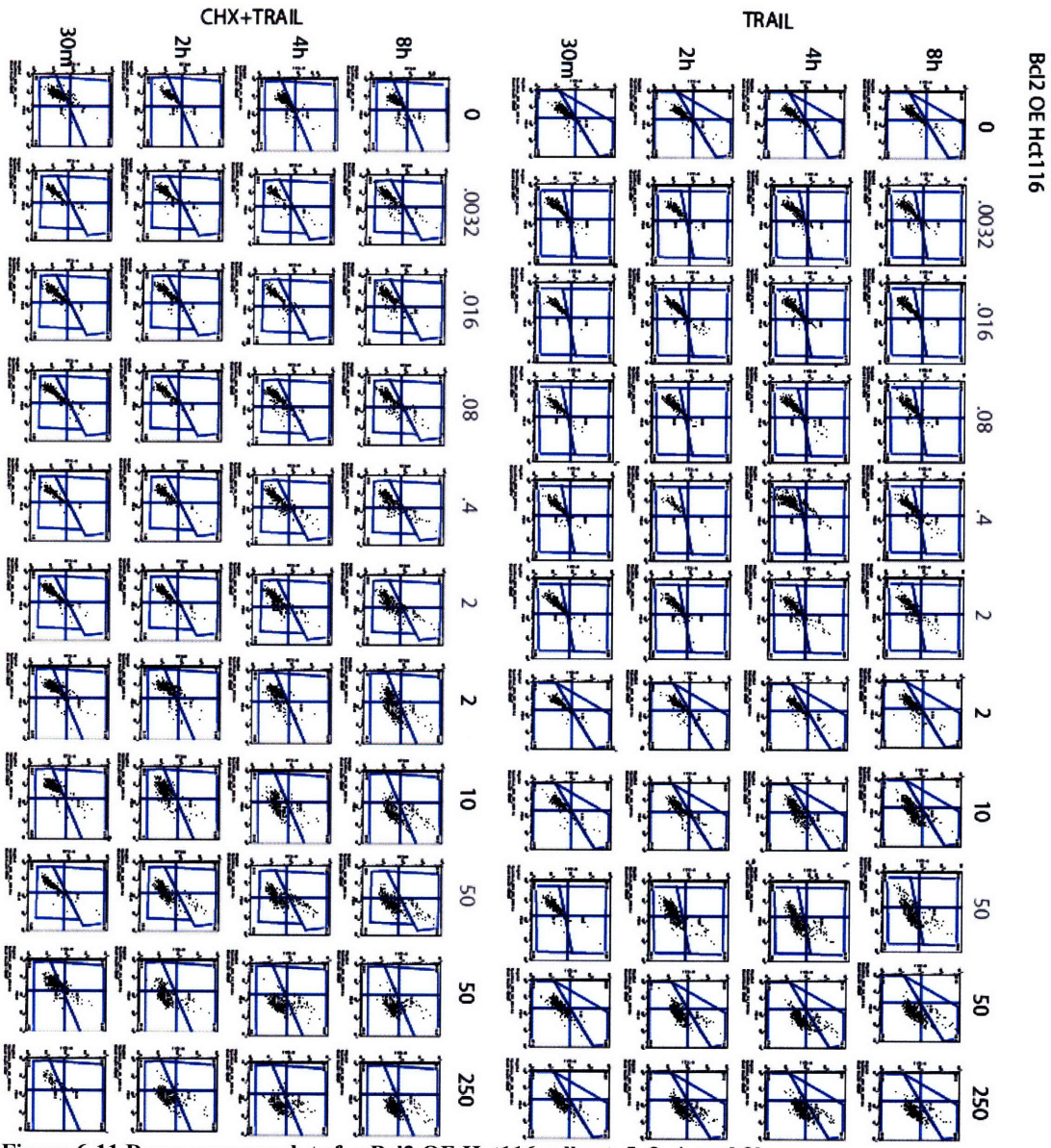

Figure 6-11 Dose response plots for Bcl2 OE Hct116 cells at .5, 2, 4, and 8h

Dose responses to 0, 0.0032, 0.016, 0.08, 0.4, 2, 10, 50, 250 ng/mL of TRAIL (and 2.5 μg/mL CHX as indicated) are plotted with the two-colored FACS assay for initiator and effector caspase activity (see Section 4.4.3). The measurements were made in two experiments (the sets are colored by dose in black and gray).

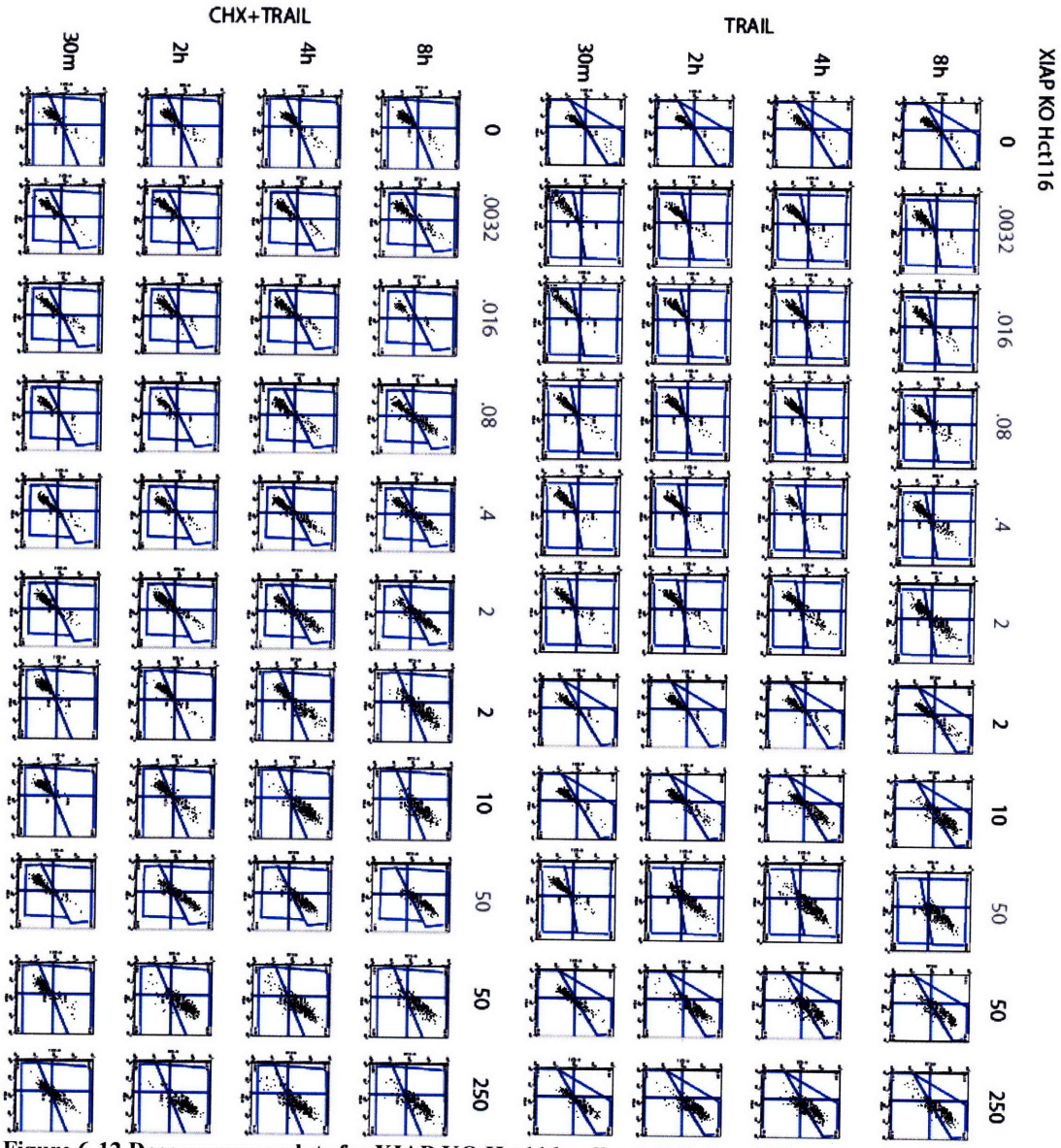

Figure 6-12 Dose response plots for XIAP KO Hct116 cells at .5, 2, 4 and 8h
Dose responses to 0, 0.0032, 0.016, 0.08, 0.4, 2, 10, 50, 250 ng/mL of TRAIL (and 2.5 μg/mL CHX as indicated) are plotted with the two-colored FACS assay for initiator and effector caspase activity (see Section 4.4.3). The measurements were made in two experiments (the sets are colored by dose in black and gray).

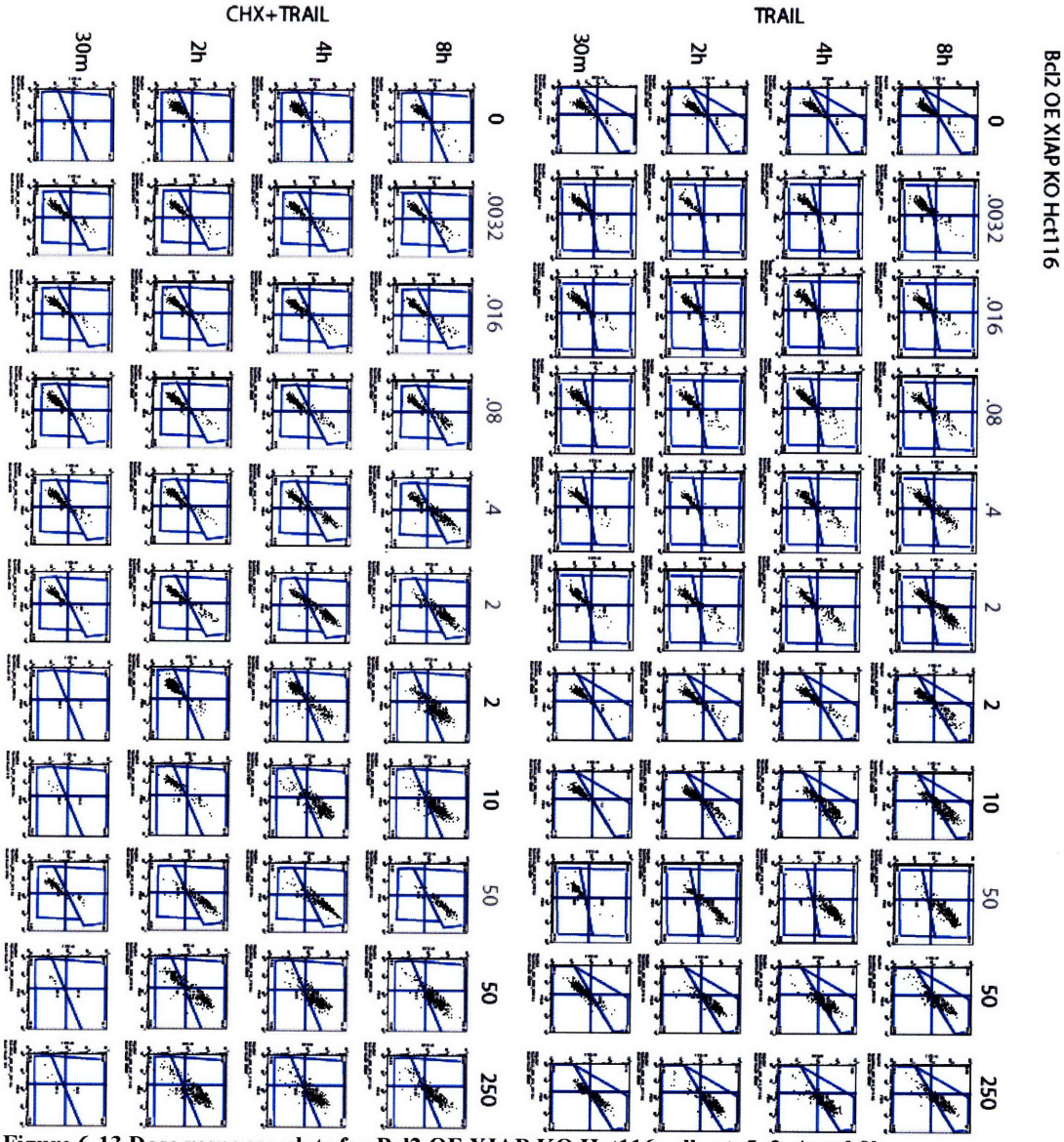

Figure 6-13 Dose response plots for Bcl2 OE XIAP KO Hct116 cells at .5, 2, 4 and 8h

Dose responses to 0, 0.0032, 0.016, 0.08, 0.4, 2, 10, 50, 250 ng/mL of TRAIL (and 2.5 μg/mL CHX as indicated) are plotted with the two-colored FACS assay for initiator and effector caspase activity (see Section 4.4.3). The measurements were made in two experiments (the sets are colored by dose in black and gray).

Figure 6-14 Dose response plots for SKW 6.4 cells at .5, 2, 4 and 8h
Dose responses to 0, 0.0032, 0.016, 0.08, 0.4, 2, 10, 50, 250 ng/mL of TRAIL (and 2.5 μg/mL CHX as indicated) are plotted with the two-colored FACS assay for initiator and effector caspase activity (see Section 4.4.3). The measurements were made in two experiments (the sets are colored by dose in black and gray).

6.4 Quantitative, dynamic measurement of effector caspase activation in single cells using FRET[4]

6.4.1 Preface

The all-or-nothing activation of effector caspases, primarily caspase-3, is key in ensuring that cells make a clear decision to survive or die. To understand the signaling network regulating this characteristic fast activation which is preceeded by a variable delay following DISC activation, we require single cell studies that track MOMP, and initiator and effector caspase activation under different network perturbations. This section contains excerpts from [142] that pertain to my work building and testing the effector caspase FRET-based reporter.

6.4.2 Study Abstract

Apoptosis in response to TRAIL or TNF requires the activation of initiator caspases, which then activate the effector caspases that dismantle cells and cause death. However, little is known about the dynamics and regulatory logic linking initiators and effectors. Using a combination of live-cell reporters, flow cytometry, and immunoblotting, we find that initiator caspases are active during the long and variable delay that precedes mitochondrial outer membrane permeabilization (MOMP) and effector caspase activation. When combined with a mathematical model of core apoptosis pathways, experimental perturbation of regulatory links between initiator and effector caspases reveals that XIAP and proteasome-dependent degradation of effector caspases are important in restraining activity during the pre-MOMP delay. We identify

[4] This section contains excerpts and figures from 142. Albeck, J.G., et al., *Quantitative analysis of pathways controlling extrinsic apoptosis in single cells.* Mol Cell, 2008. **30**(1): p. 11-25.

conditions in which restraint is impaired, creating a physiologically indeterminate state of partial cell death with the potential to generate genomic instability. Together, these findings provide a quantitative picture of caspase regulatory networks and their failure modes.

6.4.3 Selective live-cell reporters for initiator and effector caspases

To monitor caspase regulation in single living cells, we constructed three fluorescent protein (FP) fusions (Figure 6-15A, B). The first, effector caspase reporter protein (EC-RP), monitors caspase-3 activity (and, to a lesser extent, caspase-7 activity) and is composed of a Förster resonance energy transfer (FRET) donor-acceptor pair (CFP and YFP) connected via a flexible linker that contains the caspase cleavage sequence DEVDR (Figure 6-15B). When the linker is cleaved, energy transfer is lost and the CFP signal increases, an event that can be monitored by live-cell microscopy. The DEVDR linker in EC-RP is expected to have 20-fold greater selectivity for caspase-3 relative to caspase-8 than the DEVDG linker used in previously published caspase reporters [20, 161, 162], based on *in vitro* data showing DEVDR to reduce k_{cat}/K_m for caspase-8 ~300-fold, but k_{cat}/K_m for caspase-3 only ~14-fold relative to DEVDG [163].

Initiator caspase reporter protein (IC-RP) carries tandem copies of IETD in its linker, a sequence that is efficiently cleaved by caspase-8 [164], but poorly by caspases-3,7 [165]. IETD constitutes the site in procaspase-3 for initiator caspase cleavage, and IC-RP cleavage is therefore a good readout of procaspase-3 activation. Finally, a reporter for MOMP that localizes to the inter-membrane space (IMS-RP) was created by fusing RFP to the mitochondrial import sequence of Smac (residues 1- 59) [166]. FP fusions to full-length cytochrome c and Smac have been described previously [7, 167, 168], but

IMS-RP differs from these fusions in lacking an IAP-binding motif, and it is therefore biochemically inactive.

To validate the properties of EC-RP, IC-RP, and IMS-RP *in vivo,* HeLa cells stably expressing the reporter proteins were treated with TRAIL and cycloheximide (CHX) and fluorescence signals monitored every 3 min over an 8-12 hr period. IMS-RP distribution was monitored using an image-processing algorithm that detects shifts from punctuate mitochondrial to diffuse cytosolic fluorescence. When cells were treated with varying doses of TRAIL, IMS-RP relocalized at the same time as a co-expressed Smac-CFP fusion [169] and ~6-9 min prior to the appearance of apoptotic cellular morphology (Figure 6-15C). IMS-RP translocation was blocked in TRAIL-treated cells by RNAi-mediated depletion of caspase-8 and Bid, upstream components of the extrinsic cell death pathway, but not by RNAi of downstream components such as Smac (Figure 6-15D). Thus, IMS-RP appears to be a faithful reporter of protein translocation at MOMP, a process whose dynamics differs from that of falling mitochondrial membrane potential as measured using dyes [167].

Caspase-mediated proteolysis of EC-RP and IC-RP was monitored by calculating the ratio of CFP and YFP emission, with suitable correction for background (see Section 6.4.4). Due to spectral overlap, it was not possible to monitor EC-RP, IC-RP, and IMS-RP fluorescence simultaneously in single cells, and we therefore expressed the reporters in pairs. When cells co-expressing EC-RP and IMS-RP were treated with TRAIL, increases in the CFP/YFP ratio resulting from reporter cleavage were sudden and took place only after IMS-RP translocation (Figure 6-15E; note that EC-RP signals were typically lost when cells detached from the slide subsequent to the appearance of

apoptotic morphology). EC-RP cleavage was reduced 20-fold by RNAi of caspase-8 and 5-fold by RNAi of Bid, consistent with a requirement for MOMP in caspase-3 activation. Control experiments also established that changes in EC-RP fluorescence required TRAIL (CHX alone had no effect) and were sequence-specific (being absent with a non-cleavable DEVG-carrying reporter). However, changes in cell in morphology did alter apparent FRET signals and were therefore taken into account during image analysis.

Cells co-expressing IC-RP and IMS-RP exhibited gradual increases in IC-RP signal subsequent to TRAIL treatment, and rapid increases subsequent to MOMP (IMS-RP release; Figure 6-15F). The early, gradual phase of IC-RP cleavage was insensitive to Bid depletion but the fast post-MOMP phase was eliminated by it; both were blocked by depletion of caspase-8. Rapid IC-RP cleavage post-MOMP probably reflects either elevated caspase-8 activity resulting from feedback via caspase-6 or cleavage by caspase-9 (RNAi experiments were ambiguous with respect to these possibilities but the IETD sequence in IC-RP is known to be a good caspase-9 substrate). We therefore conclude that IC-RP is a selective readout of caspase-8 activity prior to MOMP but is unlikely to retain this selectivity later on; however, it is complemented by EC-RP, which is the key readout of the post-MOMP state. Direct comparison with a traditional reporter carrying a DEVDG caspase-3 recognition sequence further demonstrates the utility of the new EC-RP reporter: unlike EC-RP, or endogenous caspase substrates (see below), cleavage of the traditional reporter occurred prior to MOMP (as monitored by IMS-RP release) and was only partially blocked by Bid depletion (Figure 6-15G).

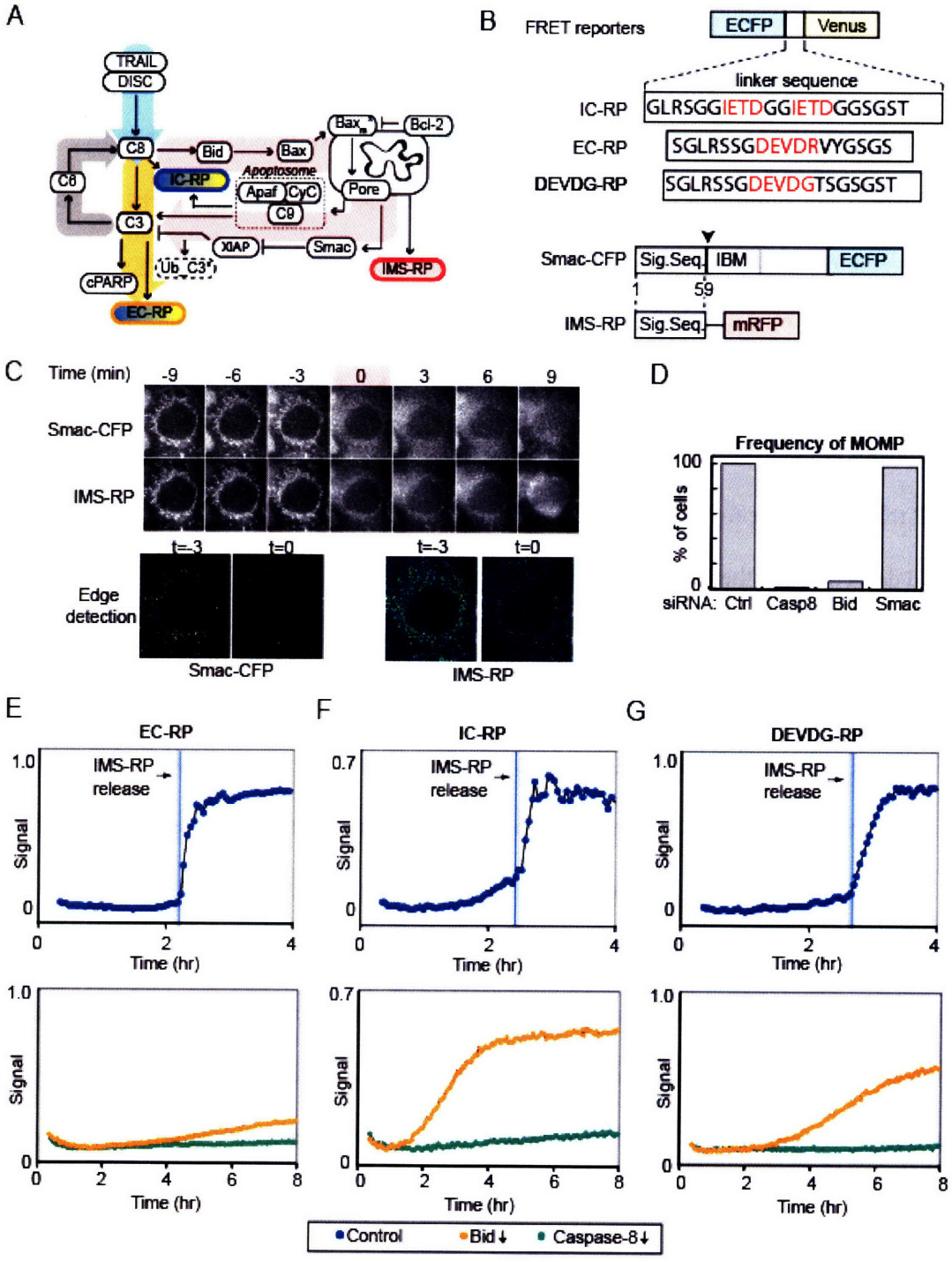

Figure 6-15 Live-cell reporters for monitoring extrinsic cell death
In all cases, cells were treated with 50 ng/ml TRAIL+2.5 µg/ml CHX. A,B. Schematic diagram of TRAIL-induced apoptotic pathways and reporter proteins. Abbreviations: ECFP - enhanced cyan fluorescent protein; Venus - venus yellow fluorescent protein; Sig. seq.- mitochondrial import signal sequence; IBM - IAP-binding motif; mRFP – monomeric red fluorescent protein. C. Kinetics of IMS-RP and Smac-CFP release from mitochondria. Top: Images from an individual cell expressing both IMS-RP and Smac-CFP and treated with TRAIL+CHX, at 3 min intervals. Time is relative to the first frame in which IMS-RP and

Smac-CFP translocation was visible (t=0, pink bar). Bottom: Comparison of IMS-RP and Smac-CFP localization immediately preceding (t=-3 min) and following (t=0 min) MOMP using an edge detection filter (see Materials and Methods). D. Percentage of cells exhibiting IMS-RP release when transfected with control, Bid, caspase-8, or Smac siRNAs and treated for 12 hours with TRAIL+CHX. E,F,G. Timecourses of cleavage for EC-RP (E), IC-RP (F), or DEVDG-RP (G) imaged in single siRNA-transfected cells treated with TRAIL+CHX. In cells treated with control siRNA, vertical lines indicate the time of IMS-RP release; release did not occur in the Bid- and caspase-8-depleted cells.

6.4.4 Materials and Methods

6.4.4.1 Reporter construct

DEVDG-RP was constructed by ligating Venus YFP between BamHI and EcoRI sites in pECFP-C1, and ligating linkers encoding cleavage sequences as BspEI-BamHI fragments between ECFP and Venus. Multiple serine and glycine residues flanking the cleavage sequences were added to increase linker flexibility and substrate accessibility. *Cell lines and materials* HeLa cells were obtained from the ATCC and cultured in DMEM supplemented with 10% calf serum and L-glutamine; Bcl-2-overexpressing cells were obtained from Dr. Fei Hua and Dr. Michael Cardone. HeLa cells stably expressing combinations of EC-RP, IC-RP, and IMS-RP were derived by transfection with Fugene 6 (Roche) and isolation of puromycin and geneticin-resistant colonies. SuperKiller TRAIL was obtained from Alexis Biochemicals and CHX from Sigma-Aldrich.

6.4.4.2 Live-cell microscopy and image analysis

Time-lapse movies were recorded using a Deltavision-modified Spectris IX71 fluorescence microscope equipped with an environmental chamber (Olympus, Applied Precision) at 10x or 60x magnification with frames every 3 min. Cells grown in 8-well chambered cover glass slides (Nunc) were shifted into phenol red-free CO_2-independent medium (Invitrogen) supplemented with 1% fetal bovine serum and L-glutamine for imaging. For FRET analysis, background-subtracted CFP and YFP images were divided

to create a ratiometric image using ImageJ and custom plug-ins (available on request). Signals were normalized by subtracting the minimum value across all time points from each single-cell time course.

6.4.5 Conclusions

We use live-cell imaging, flow cytometry and mathematical modeling to examine the states of the core apoptotic network, comprising caspases and their immediate regulators, in HeLa cells exposed to TRAIL. Single-cell data show that cells treated with TRAIL enter a state of delay lasting many hours, during which initiator caspases are active. Because procaspase-3 is a direct substrate of initiator caspases, the enzymatically active form of caspase-3 is generated steadily throughout the delay state, but its activity is held fully in check. Previous single-cell experiments examining the dynamics of initiator and effector caspase activation by death ligands have been contradictory, with the most recent reports concluding that the two are simultaneous [164, 170, 171]. Our data, based on improved reporters and quantitative analysis of a large number of cells, demonstrate that this is not the case. If MOMP is blocked by Bcl-2 overexpression or Bid depletion, or if TRAIL is added at very low doses, the pre-MOMP delay state can persist with initiator caspases on and effector caspases off for many hours.

Experiments with proteasome inhibitors strongly suggest that ubiquitin-dependent degradation of caspase-3 is essential for effective inhibition of its enzymatic activity. Modeling reveals why this is true: were caspase-3 inhibition dependent solely on XIAP's activity as a nanomolar competitive inhibitor (K_d ~1 nM) [172], a >100-fold molar excess of XIAP over caspase-3 would be required to ensure the highly efficient inhibition of proteolytic activity observed experimentally in pre-MOMP cells. This arises

because a competitive inhibitor of an irreversible enzymatic reaction must be present in large excess to block access of abundant substrates to the enzyme active site [172]. However, XIAP is not present in large molar excess over caspase-3, and available data suggest that the proteins are present in HeLa cells at roughly similar levels [173]. Conversely, if caspase-3 is modeled as being unstable with a $t_{1/2}$ of ~20 min, active caspase never accumulates to a high level, and the need for a vast excess of XIAP levels is reduced. XIAP has an E3 activity, and it is therefore reasonable to model it as having two activities, one as a competitive inhibitor of caspase-3 catalytic activity and the other as a mediator of XIAP ubiquitination (although other possibilities can be imagined, and direct tests with mutant XIAPs remain necessary). It should be noted that even when both the competitive inhibitory and E3 ligase activities of XIAP are included in our model, the degree of caspase-3 inhibition observed in pre-MOMP cells is achieved only with XIAP levels higher than those we estimate by semiquantitative Western blotting (data not shown). Thus, additional mechanisms of caspase-3 inhibition are required, among which ubiquitin-independent caspase-3 degradation with a $t_{1/2}$ ~70 min is one [144]. Our working model is that three (and possibly more) distinct processes are involved in restraining caspase-3 catalytic activity during the pre-MOMP delay: competitive inhibition by XIAP, XIAP E3-mediated destruction by the proteasome, and ubiquitin-independent proteolysis. Several developmental processes are associated with procaspase-3 cleavage in the absence of cell death and it will be interesting to ascertain if similarly complex mechanisms of caspase-3 regulation are involved [174].

6.5 *Quantification of orderliness of kinetochore-kinetochore pairs*[5]

6.5.1 Preface

I have heard more than one applied mathematician joke that the answer to all problems lies in the singular value decomposition (SVD). The SVD has been extremely useful in reducing the apparent dimensionality from complex datasets to reveal similarities and differences amongst data points. This section contains excerpts from [175] that pertain to my work quantifying orderliness in kinetochore-kinetochore pairs using the SVD and Shannon entropy. This work highlights the flexibility of SVD in teasing out dominant trends in data that changes orientation (and number) at each time step. The Shannon entropy was used to characterize the spread of the singular values arising from the decomposition. Together, these seemingly irrelevant tools from mathematical and information theory have enabled us to develop a novel quantification method for variable, orientation- and point- changing data in cell biology. Without this methodology, the observed phenotype could not be quantified and critically evaluated. Because kinetochore biology has not been introduced in this thesis, the introductory section from the paper is included.

6.5.2 Study Abstract

The correct formation of stable but dynamic links between chromosomes and spindle microtubules (MTs) is essential for accurate chromosome segregation. However, the molecular mechanisms by which kinetochores bind MTs and checkpoints monitor this

[5] This section contains excerpts and figures from 175. Draviam, V.M., et al., *Misorientation and reduced stretching of aligned sister kinetochores promote chromosome missegregation in EB1- or APC-depleted cells.* Embo J, 2006. **25**(12): p. 2814-27.

binding remain poorly understood. In this paper we analyze the functions of six kinetochore-bound microtubule-associated proteins (kMAPs) using RNAi, live-cell microscopy and quantitative image analysis. We find that RNAi-mediated depletion of two kMAPs, the Adenomatous Polyposis Coli protein (APC) and its binding partner, EB1 are unusual in affecting the movement and orientation of paired sister chromatids at the metaphase plate without perturbing kinetochore-MT attachment *per se*. Quantitative analysis shows that misorientation phenotypes in metaphase are uniform across chromatid pairs even though chromosomal loss (CIN) during anaphase is sporadic. However, errors in kinetochore function generated by APC or EB1 depletion are detected poorly if at all by the spindle checkpoint, even though they cause chromosome missegregation. We propose that impaired EB1 or APC function generates lesions invisible to the spindle checkpoint and thereby promotes low levels of CIN expected to fuel aneuploidy and possibly tumorigenesis.

6.5.3 Introduction

Kinetochores are multi-protein structures that assemble on centromeric DNA and mediate the attachment of chromosomes to microtubules (MTs). During metaphase, pairs of sister kinetochores undergo a complex series of movements in which they capture the plus ends of MTs emanating from centrosomes and also nucleate the formation of MTs that are guided toward the poles, so as to form stable bipolar attachments to the mitotic spindle [176]. Following the completion of bipolar attachment by all chromatid pairs, and the consequent silencing of the Mad and Bub-dependent spindle checkpoint, sister chromatids disjoin and move towards poles, around which daughter cells form [177]. In many MT-based processes, motors and MT associated proteins (MAPs) work together to

regulate MT dynamics in a spatially controlled fashion and to generate forces necessary for directed movement [178]. Thus, the establishment of bipolarity is thought to depend on the capture of MTs by kinetochores and the subsequent regulation of MT +end polymer dynamics by MAPs and motors.

A critical question in the study of mitosis is determining why CIN and aneuploidy are more frequent in tumor cells than in normal cells [179]. The process of MT capture by kinetochores is stochastic and therefore takes different lengths of time in different cells. The function of the spindle checkpoint is to monitor the capture process in each cell and ensure that anaphase is not initiated until all sister kinetochore pairs are correctly MT-bound. Thus one possible cause of CIN is that checkpoint pathways are not functional in tumor cells. However, while CIN is observed in yeast carrying mutations in either checkpoint or kinetochore genes [180] analogous mutations in human cells cause mitotic catastrophe and cell death [181]. Thus, it is not surprising that only few human tumors have been found to harbor mutations in Mad and Bub spindle checkpoint genes [182, 183]. In contrast to checkpoint and inner kinetochore proteins, outer kinetochore components are attractive as genes whose disruption might impair chromosome-MT attachment while leaving the checkpoint intact [184, 185]; VMD and PKS, unpublished results). Chronic disregulation of kMAP function might have similar effects as low doses of anti-MT drugs such as taxol and the vinca alkaloids, which cause CIN in some cells [186].

Previous work in a variety of eukaryotes has identified many MAPs that localize to kinetochores [187]. The Dynein-Dynactin motor complex and the +end binding proteins CLIP170 and LIS1 accumulate on kinetochores that are unattached to MTs [188,

189]. In contrast, EB1 is recruited selectively to kinetochores that are associated with growing MTs [190] and Adenomatous Polyposis Coli protein (APC), an EB1 binding protein is enriched on kinetochores bound to MTs [191, 192]. Finally, CLASP1 localizes to kinetochores regardless of MT-attachment status [193]. CLASP1 and CLIP170 regulate kinetochore-MT binding in distinct ways: CLASP1 controls MT dynamics at attached kinetochores [194, 195] while CLIP170 is involved in MT capture [196]. As expected, depletion of CLIP170 or CLASP1 interferes with bipolar MT binding and causes cells to arrest in mitosis in a checkpoint-dependent fashion [195, 196]. In the case of Dynein or LIS1, published data are contradictory with respect to function in mitosis and MT binding [189, 197-200]. Depletion of the EB1 or APC kMAPs has been reported to cause chromosome misalignment and missegregation[192, 200], implying a defect in the checkpoint response, but it is unknown why APC and EB1 depleted cells divide rather than arrest when misaligned chromosomes are present.

In this paper, we study the effects of disrupting proteins at the kinetochore-MT interface on the generation of CIN in human cells. We use live-cell microscopy and quantitative image analysis to compare directly the fates of mitotic cells that have been depleted of one of six kMAPs by RNAi. We find that depletion of CLIP170, Dynein heavy chain (DHC), LIS1 or chTOG1 prevents normal chromosome congression and results in prolonged checkpoint-dependent mitotic arrest, eventually leading to cell death. In contrast, depletion of EB1 or APC does not significantly interfere with congression but prevents the formation of an ordered metaphase plate. This leads to sporadic chromosome missegregation at anaphase. The lesions induced by EB1 or APC loss are sensed poorly if at all by the spindle checkpoint but the checkpoint itself is still functional. We speculate

that sporadic missegregation of chromosomes in EB1- or APC-depleted cells represents a type of CIN that might fuel tumorigenesis.

6.5.4 Disordered metaphase plate in EB1- and APC-depleted cells

Although chromosomes congressed to the spindle equator in EB1- or APC-depleted cells, metaphase plates were less compact than in control cells. To quantify the degree of order in the metaphase plate, the rotational angles of k-k axes (line connecting sister kinetochores defining kinetochore orientation) was determined for multiple kinetochores per spindle by examining 3D images of cells expressing the kinetochore marker CENPB-GFP. Typically, 12-18 k-k axes could be distinguished clearly per cell per time point in the 6min preceding anaphase. The angles describing each set of k-k axes ($\alpha_1,\beta_1,\gamma_1; \alpha_2,\beta_2,\gamma_2; ...$) were then transformed by singular value decomposition (SVD) into a new set of optimal angles ($\alpha_1',\beta_1',\gamma_1'; \alpha_2',\beta_2',\gamma_2';...$) and singular values (SVs; $\sigma_1,\sigma_2,\sigma_3$) (Figure 6-16A). Under normal circumstances, MTs exert pulling forces on bioriented kinetochore pairs causing them to line up in an ordered metaphase with their k-k axes oriented parallel to each other and to the spindle axis (Figure 6-16B). A set of ordered k-k axes has one high, and two low SVs (Figure 6-16A, left) whereas a set of disordered axes has more than one high SV (Figure 6-16A, right). The overall extent of disorder can be captured by the Shannon entropy, which varies from 0, representing perfect order, to 1, representing complete disorder (Figure 6-16B and see Methods). Importantly, SVD is robust to variability in the number of measurements and is unaffected by large and rapid rotations in the spindle axis, such as those induced by EB1 and APC depletion.

When the Shannon entropy associated with k-k axis orientations was quantified in individual EB1-, APC- or control-depleted cells over a 6min period prior to anaphase

onset, a striking result was obtained. In control cells, the Shannon entropy started out relatively high (0.68 ± 0.15) but fell rapidly (to 0.03 ± 0.07) 1.5min before anaphase onset (Figure 6-16C). In contrast, in EB1- or APC-depleted cells, the Shannon entropy was high throughout the observation period, remaining as high at -1.5min as at -6min (0.6 to 0.7; Figure 6-16C). In principle, high Shannon entropies might reflect severe misorientation of a few sisters or widespread disorder involving many sisters (Figure 6-16A). To distinguish among these two extremes we plotted the SVs for individual k-k axes over time. In control cells, only two or three sisters had axes pointing away from the most probable direction by t= -3min (Figure 6-16D). All of these misorientations were resolved in the minute or two before anaphase onset. In EB1- or APC-depleted cells, in contrast, disorderliness was distributed more or less uniformly across kinetochore pairs and remained high as metaphase proceeded (Figure 6-16E and 6-16F). The difference between control and APC-depleted cells was highly significant (p=0.008 as estimated using K-Annova) as was the difference between control and EB1-depleted cells (p=0.004); however, EB1 and APC depletions (p=0.87) were indistinguishable. We therefore conclude that high Shannon entropy in k-k axes in EB1 and APC depleted cells is due to extensive misorientation involving many sister chromatids.

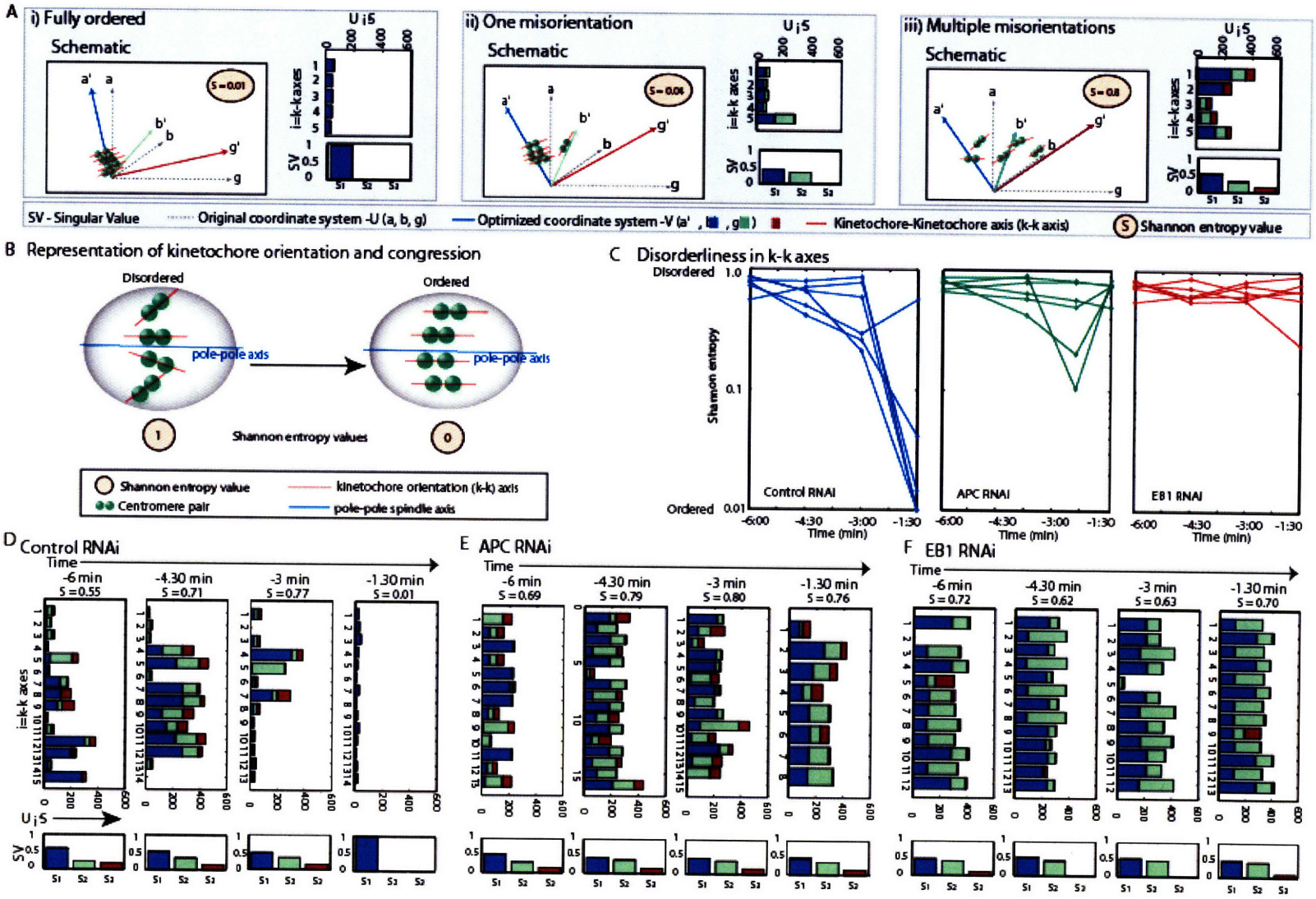
A
i) Fully ordered
Schematic
S = 0.01
ii) One misorientation
Schematic
S = 0.04
iii) Multiple misorientations
Schematic
S = 0.8
U i S
i=k-k axes
SV
SV - Singular Value
Original coordinate system -U (a, b, g)
Optimized coordinate system -V (a' , g')
Kinetochore-Kinetochore axis (k-k axis)
S Shannon entropy value
B Representation of kinetochore orientation and congression
Disordered
Ordered
pole-pole axis
Shannon entropy values
Shannon entropy value
Centromere pair
kinetochore orientation (k-k) axis
pole-pole spindle axis
C Disorderliness in k-k axes
Disordered 1.0
Shannon entropy
0.1
Ordered 0.01
Control RNAi
APC RNAi
EB1 RNAi
-6:00
-4:30
-3:00
-1:30
Time (min)
D Control RNAi
E APC RNAi
F EB1 RNAi
Time
-6 min
-4.30 min
-3 min
-1.30 min
S = 0.55
S = 0.71
S = 0.77
S = 0.01
S = 0.69
S = 0.79
S = 0.80
S = 0.76
S = 0.72
S = 0.62
S = 0.63
S = 0.70

Figure 6-16 EB1 or APC depletions perturb orientation of centromeric pairs
(A) Schematic representation of three distinct states of k-k axes orderliness. Orthogonal lines indicate orientations of the original coordinate system α, β, γ (grey) and new optimized directions α',β',γ' (blue, green, red). Bar graphs show the contribution of each of the five k-k axes to the optimized directions. Plots below indicate singular values (SV) in three directions (σ_1,σ_2,σ_3). (B) Schematic representation of disorderliness in k-k axes of congressed kinetochores. Shannon entropy values for a state of complete disorderliness =1 and orderliness =0 (C) Shannon entropy of 10-15 k-k axes calculated in each of 5 cells for a 6min period prior to anaphase onset. Cells were transfected with control, EB1 or APC siRNA oligos as indicated. (D-F) Graphs indicate contribution of individual k-k axes to optimized direction in cells treated with siRNA against control (D), APC (E) or EB1 (F) calculated from 3D-images taken every 90sec for a 6min period prior to anaphase. Upper panel indicate $U_i\Sigma$ for individual k-k axis. Lower panels indicate SV (σ_1,σ_2,σ_3). S indicates Shannon entropy value.

6.5.5 Chromosome missegregation following EB1 and APC depletion

When the Shannon entropy associated with k-k axes was plotted against the number of lagging chromosomes on a cell-to-cell basis, a strong positive correlation was observed (Figure 6-17A): the greater the entropy, the larger the number of lagging chromosomes. Thus, disorder in the alignment of kinetochore pairs on the metaphase plate was closely associated with chromosome missegregation in anaphase. It was striking, however, that most sister kinetochores were unstretched and misoriented following EB1 or APC depletion but only a few subsequently missegregated in anaphase. To investigate the relationship between disorder in the metaphase plate and non-disjunction we attempted to follow individual kinetochore pairs immediately before and after anaphase. In HeLa cells, chromosomes are crowded at the spindle equator and tracking individual kinetochores is technically challenging. However, in four EB1-depleted cells and five APC-depleted cells from four independent experiments, it was possible to trace the kinetochores of lagging chromosomes in anaphase to kinetochore pairs displaying a high degree of k-k axis misorientation late in metaphase (Figure 6-17B and 6-17C). When lagging kinetochores were followed through to telophase, it was also apparent that laggards were incorrectly assorted among daughter cells; unseparated kinetochore pairs were segregated as a set into one daughter cell (Figure 6-17D). Despite

a strong association between metaphase misalignment and lagging kinetochores and between lagging kinetochores and non-disjunction, it is significant that many sister kinetochores with misoriented k-k axes disjoined normally. Thus, EB1 and APC depletion cause highly penetrant problems with orientation and stretching of kinetochore pairs but a particular kinetochore pair in a single cell still has only a low probability of being missegregated.

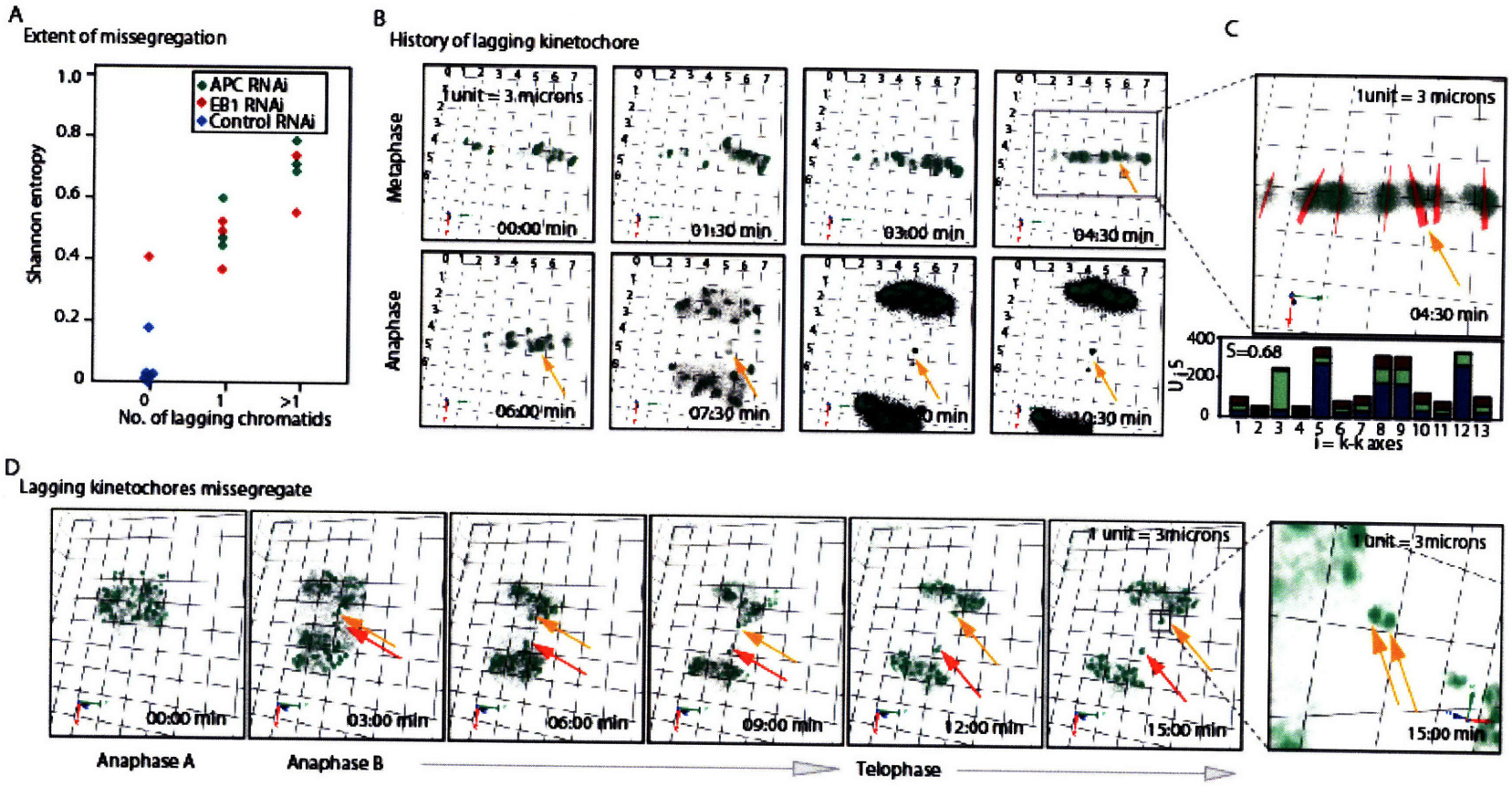
A
Extent of missegregation
APC RNAi
EB1 RNAi
Control RNAi
Shannon entropy
1.0
0.8
0.6
0.4
0.2
0
0
1
>1
No. of lagging chromatids
B
History of lagging kinetochore
Metaphase
Anaphase
1unit = 3 microns
00:00 min
01:30 min
03:00 min
04:30 min
06:00 min
07:30 min
C
1unit = 3 microns
04:30 min
S=0.68
400
200
0
1 2 3 4 5 6 7 8 9 10 11 12 13
i = k-k axes
D
Lagging kinetochores missegregate
00:00 min
03:00 min
06:00 min
09:00 min
12:00 min
15:00 min
1 unit = 3microns
Anaphase A
Anaphase B
Telophase

Figure 6-17 Misoriented centromeres lag in anaphase and undergo missegregation
(A) Plot of Shannon entropy values associated with k-k axis orientation in single siRNA-treated cells 90sec prior to anaphase and the number of lagging chromosomes that appeared subsequently in anaphase. (B) Rendered images of 5μm thick section acquired every 90sec in a CENPB-GFP expressing cell treated with EB1 siRNA. Orange arrows mark lagging centromeres. (C) 3X-enlarged image details k-k axes (red) with bold lines projected out of plane and thin lines parallel to plane. Bar graph shows the contribution of individual k-k axis to optimized direction at t=4:30min; S indicates Shannon entropy value. (D) Rendered images of 5μm thick section acquired every 3min in a CENPB-GFP expressing cell treated with EB1 siRNA (orange and red arrows mark lagging kinetochores). Far right panel is 0:6:82 -rotated and 8X enlarged; arrows mark unseparated pair. 1unit=3μm.

6.5.6 Methods: Quantification of k-k axes disorderliness

Rotation angles (α,β,γ) of k-k axes were obtained from each cell at discrete times using SoftWorx. Sets of angles for n k-k axes were arranged into matrix $\mathbf{A}$ (nx3). *svd* function in MATLAB was used to compute singular value decomposition (SVD) of $\mathbf{A}=\mathbf{U}\Sigma\mathbf{V}^T$ where $\mathbf{U}$ and $\mathbf{V}$ are orthogonal and Σ is diagonal of singular values ($\sigma_1,\sigma_2,\sigma_3$). SV describes degree of variation in the angles along each direction in $\mathbf{V}$ (α',β',γ'). Shannon entropy of the SV [201] is defined as

$$S = \frac{-1}{\log(L)} \sum_{i=1}^{3} p_i \log(p_i)$$

where

$$p_i = \frac{\sigma_i^{\,2}}{\sum_{j=1}^{3} \sigma_j^{\,2}}.$$

6.5.7 Conclusions: Defects in metaphase plate dynamics caused by EB1 or APC depletion

Although chromosomes in EB1- or APC-depleted cells congressed to the spindle equator, two defects in the resulting metaphase plate were evident: kinetochore pairs did not orient in an orderly fashion and they were not fully stretched. In control cells, most

kinetochore pairs aligned early in metaphase perpendicular to the spindle equator and oriented parallel to each other. The completion of congression manifested itself as a decrease in the entropy of k-k axis orientations. Concomitantly, inter-kinetochore stretching increased such that all centromere pairs were stretched by the time anaphase was initiated. The ordered orientation and stretching of centromeres are almost certainly linked: stretching reflects the imposition of pulling forces on pairs of sisters following bi-orientation and causes k-k axes to align parallel to the spindle axis, and thus to each other. In EB1- or APC-depleted cells, in contrast, centromeres do not stretch normally and k-k axes point in different directions. The similarity between EB1 and APC depletion phenotypes suggests that interaction of the two proteins might be important. EB1 C-terminus contains APC-binding site and also the sites for binding to other k-MAPs, including p150Glued, CLIP-170 and CLASP1. However, p150Glued, CLIP-170 whereas EB1 and APC are present until anaphase ([188, 193]; VMD and PKS, unpublished data). EB1 and APC localize in a MT-dependent fashion whereas CLASP1 associates early on with kinetochore in a MT-independent fashion [193]. Thus, anaphase defects observed in cells expressing an EB1 C-terminal deletion mutant probably reflect a dominant negative effect on APC -EB1 binding.

What prevents kinetochore from becoming stretched and ordered at the metaphase plate in EB1- and APC-depleted cells? One possibility is kMT +end dynamics are disrupted. EB1 is shown to stabilize MT +ends and to accumulate on kinetochores attached to growing MTs [190]. Mutations in APC that disrupt APC-EB1 interaction are reported to increase the frequency of pausing between periods of MT +end growth and shrinkage [200]. In EB1- or APC-depleted cells, an increased incidence of +end pausing

would perturb the oscillation of sisters along the spindle axis and potentially cause kinetochores to remain unstretched. Reduced stretching would then interfere with the establishment of a preferred k-k orientation. Finally, errors in orientation would give rise to a less compact and staggered metaphase plate, subsequently predisposing cells to missegregation.

6.6 Abbreviations

AIF – apoptosis inducing factor

APC – Adenomatous Polyposis Coli

BL – Boolean logic

c3 – caspase-3

c8 – caspase-8

cc3, c3* – cleaved caspase-3, *=active form

cc8, c8* – cleaved caspase-8, * = active form

CIN – chromosomal loss

cPARP – cleaved PARP

CSR – cue-signal-response

DISC – death-inducing signaling complex

DL – discrete logic

DLE – direct finite-time Lyapunov exponent

DOF – degree of firing

DOM – degree of membership

EGF – epidermal growth factor

ERK – extracellular signal-regulated kinase

FACS – fluorescence-activated cell sorting

FKHR – Forkhead transcription facto

FL – fuzzy logic

FRET – Förster (or fluorescence) resonance energy transfer

IKB – inhibitor of NF-κB

IKK - IκB kinase

IL-1α – interleukin-1α

IRS-1– insulin receptor substrate-1

JNK – c-jun N-terminal kinase

KO – knockout

MAPs – microtubules associated proteins

MAPK – mitogen-activated protein kinase

MAPKK – mitogen-activated protein kinase kinase

MAPKKK – mitogen-activated protein kinase kinase kinase

MEK – MAP extracellular signal-regulated kinase kinase

MF – membership function

MK – MAPK-activated protein kinase

MK2 – mitogen-activated protein kinase-activated protein kinase 2

MOMP – mitochondrial outer membrane permeabilization

mTOR – mammalian target of rapamycin

MTs – microtubules

NF-κB – nuclear factor κ B

NSAID – non-steroidal anti-inflammatory drug

ODE – ordinary differential equation

OE – overexpressing

PARP – Poly ADP ribose polymerase

PCA – principal component analysis

PDE – partial differential equation

PLSR – partial least-squares regression

ProC3 – pro-caspase-3

SVD – singular value decomposition

TGF α – transforming growth factor α

TNF – tumor necrosis factor α

TRAIL – tumor necrosis factor-related apoptosis-inducing ligand

XIAP – X-linked inhibitor of apoptosis

7 References

1. Danial, N.N. and S.J. Korsmeyer, *Cell death: critical control points.* Cell, 2004. **116**(2): p. 205-19.
2. Alberts, B., et al., *Molecular Biology of the Cell.* 2002, New York: Garland Science.
3. Cory, S. and J.M. Adams, *The Bcl2 family: regulators of the cellular life-or-death switch.* Nat Rev Cancer, 2002. **2**(9): p. 647-56.
4. Cory, S., D.C. Huang, and J.M. Adams, *The Bcl-2 family: roles in cell survival and oncogenesis.* Oncogene, 2003. **22**(53): p. 8590-607.
5. Kim, H., et al., *Hierarchical regulation of mitochondrion-dependent apoptosis by BCL-2 subfamilies.* Nat Cell Biol, 2006. **8**(12): p. 1348-58.
6. Ravagnan, L., T. Roumier, and G. Kroemer, *Mitochondria, the killer organelles and their weapons.* J Cell Physiol, 2002. **192**(2): p. 131-7.
7. Goldstein, J.C., et al., *The coordinate release of cytochrome c during apoptosis is rapid, complete and kinetically invariant.* Nat Cell Biol, 2000. **2**(3): p. 156-62.
8. Rich, T., R.L. Allen, and A.H. Wyllie, *Defying death after DNA damage.* Nature, 2000. **407**(6805): p. 777-83.
9. Aggarwal, B.B., *Signalling pathways of the TNF superfamily: a double-edged sword.* Nat Rev Immunol, 2003. **3**(9): p. 745-56.
10. Pfeffer, K., *Biological functions of tumor necrosis factor cytokines and their receptors.* Cytokine Growth Factor Rev, 2003. **14**(3-4): p. 185-91.
11. Wajant, H., K. Pfizenmaier, and P. Scheurich, *Tumor necrosis factor signaling.* Cell Death Differ, 2003. **10**(1): p. 45-65.
12. Legler, D.F., et al., *Recruitment of TNF receptor 1 to lipid rafts is essential for TNFalpha-mediated NF-kappaB activation.* Immunity, 2003. **18**(5): p. 655-64.
13. Micheau, O. and J. Tschopp, *Induction of TNF receptor I-mediated apoptosis via two sequential signaling complexes.* Cell, 2003. **114**(2): p. 181-90.
14. Kischkel, F.C., et al., *Cytotoxicity-dependent APO-1 (Fas/CD95)-associated proteins form a death-inducing signaling complex (DISC) with the receptor.* Embo J, 1995. **14**(22): p. 5579-88.
15. Cowling, V. and J. Downward, *Caspase-6 is the direct activator of caspase-8 in the cytochrome c-induced apoptosis pathway: absolute requirement for removal of caspase-6 prodomain.* Cell Death Differ, 2002. **9**(10): p. 1046-56.
16. Scaffidi, C., et al., *Two CD95 (APO-1/Fas) signaling pathways.* Embo J, 1998. **17**(6): p. 1675-87.
17. Hengartner, M.O., *The biochemistry of apoptosis.* Nature, 2000. **407**(6805): p. 770-6.

18. Boatright, K.M., et al., *A unified model for apical caspase activation.* Mol Cell, 2003. **11**(2): p. 529-41.

19. Han, Z., et al., *A sequential two-step mechanism for the production of the mature p17:p12 form of caspase-3 in vitro.* J Biol Chem, 1997. **272**(20): p. 13432-6.

20. Stennicke, H.R., et al., *Pro-caspase-3 is a major physiologic target of caspase-8.* J Biol Chem, 1998. **273**(42): p. 27084-90.

21. Deveraux, Q.L., et al., *Cleavage of human inhibitor of apoptosis protein XIAP results in fragments with distinct specificities for caspases.* Embo J, 1999. **18**(19): p. 5242-51.

22. Davis, R.J., *Signal transduction by the JNK group of MAP kinases.* Cell, 2000. **103**(2): p. 239-52.

23. Devin, A., et al., *The distinct roles of TRAF2 and RIP in IKK activation by TNF-R1: TRAF2 recruits IKK to TNF-R1 while RIP mediates IKK activation.* Immunity, 2000. **12**(4): p. 419-29.

24. Ono, K. and J. Han, *The p38 signal transduction pathway: activation and function.* Cell Signal, 2000. **12**(1): p. 1-13.

25. Lawlor, M.A. and D.R. Alessi, *PKB/Akt: a key mediator of cell proliferation, survival and insulin responses?* J Cell Sci, 2001. **114**(Pt 16): p. 2903-10.

26. Suzuki, Y., Y. Nakabayashi, and R. Takahashi, *Ubiquitin-protein ligase activity of X-linked inhibitor of apoptosis protein promotes proteasomal degradation of caspase-3 and enhances its anti-apoptotic effect in Fas-induced cell death.* Proc Natl Acad Sci U S A, 2001. **98**(15): p. 8662-7.

27. Salvesen, G.S. and C.S. Duckett, *IAP proteins: blocking the road to death's door.* Nat Rev Mol Cell Biol, 2002. **3**(6): p. 401-10.

28. Salvesen, G.S. and M. Renatus, *Apoptosome: the seven-spoked death machine.* Dev Cell, 2002. **2**(3): p. 256-7.

29. Shi, Y., *Mechanisms of caspase activation and inhibition during apoptosis.* Mol Cell, 2002. **9**(3): p. 459-70.

30. Allan, L.A., et al., *Inhibition of caspase-9 through phosphorylation at Thr 125 by ERK MAPK.* Nat Cell Biol, 2003. **5**(7): p. 647-54.

31. Dempsey, P.W., et al., *The signaling adaptors and pathways activated by TNF superfamily.* Cytokine Growth Factor Rev, 2003. **14**(3-4): p. 193-209.

32. Deng, Y., et al., *A JNK-dependent pathway is required for TNFalpha-induced apoptosis.* Cell, 2003. **115**(1): p. 61-70.

33. Devin, A., Y. Lin, and Z.G. Liu, *The role of the death-domain kinase RIP in tumour-necrosis-factor-induced activation of mitogen-activated protein kinases.* EMBO Rep, 2003. **4**(6): p. 623-7.

34. Lee, J.C. and M.E. Peter, *Regulation of apoptosis by ubiquitination.* Immunol Rev, 2003. **193**: p. 39-47.

35. Dan, H.C., et al., *Akt phosphorylation and stabilization of X-linked inhibitor of apoptosis protein (XIAP).* J Biol Chem, 2004. **279**(7): p. 5405-12.

36. Roux, P.P. and J. Blenis, *ERK and p38 MAPK-activated protein kinases: a family of protein kinases with diverse biological functions.* Microbiol Mol Biol Rev, 2004. **68**(2): p. 320-44.

37. Lin, A. and B. Dibling, *The true face of JNK activation in apoptosis.* Aging Cell, 2002. **1**(2): p. 112-6.

38. Song, G., G. Ouyang, and S. Bao, *The activation of Akt/PKB signaling pathway and cell survival.* J Cell Mol Med, 2005. **9**(1): p. 59-71.

39. Manning, B.D. and L.C. Cantley, *AKT/PKB signaling: navigating downstream.* Cell, 2007. **129**(7): p. 1261-74.

40. Luo, J., B.D. Manning, and L.C. Cantley, *Targeting the PI3K-Akt pathway in human cancer: rationale and promise.* Cancer Cell, 2003. **4**(4): p. 257-62.

41. Datta, S.R., et al., *Akt phosphorylation of BAD couples survival signals to the cell-intrinsic death machinery.* Cell, 1997. **91**(2): p. 231-41.

42. Hacker, H. and M. Karin, *Regulation and function of IKK and IKK-related kinases.* Sci STKE, 2006. **2006**(357): p. re13.

43. Janes, K.A., et al., *A systems model of signaling identifies a molecular basis set for cytokine-induced apoptosis.* Science, 2005. **310**(5754): p. 1646-53.

44. Aldridge, B.B., et al., *Physicochemical modelling of cell signalling pathways.* Nat Cell Biol, 2006. **8**(11): p. 1195-203.

45. Nurse, P., *A long twentieth century of the cell cycle and beyond.* Cell, 2000. **100**(1): p. 71-8.

46. Huang, C.Y. and J.E. Ferrell, Jr., *Ultrasensitivity in the mitogen-activated protein kinase cascade.* Proc Natl Acad Sci U S A, 1996. **93**(19): p. 10078-83.

47. Bhalla, U.S., P.T. Ram, and R. Iyengar, *MAP kinase phosphatase as a locus of flexibility in a mitogen-activated protein kinase signaling network.* Science, 2002. **297**(5583): p. 1018-23.

48. Hoffmann, A., et al., *The IkappaB-NF-kappaB signaling module: temporal control and selective gene activation.* Science, 2002. **298**(5596): p. 1241-5.

49. Markevich, N.I., J.B. Hoek, and B.N. Kholodenko, *Signaling switches and bistability arising from multisite phosphorylation in protein kinase cascades.* J Cell Biol, 2004. **164**(3): p. 353-9.

50. Schoeberl, B., et al., *Computational modeling of the dynamics of the MAP kinase cascade activated by surface and internalized EGF receptors.* Nat Biotechnol, 2002. **20**(4): p. 370-5.

51. Janes, K. and M. Yaffe, *Data-driven modelling of signal-transduction networks.* Nature Reviews Molecular Cell Biology, 2006. **7**(11): p. 820-828.

52. Oda, K., et al., *A comprehensive pathway map of epidermal growth factor receptor signaling.* Mol Syst Biol, 2005. **1**: p. 2005 0010.

53. Kitano, H., et al., *Using process diagrams for the graphical representation of biological networks.* Nat Biotechnol, 2005. **23**(8): p. 961-6.

54. Alves, R., F. Antunes, and A. Salvador, *Tools for kinetic modeling of biochemical networks.* Nat Biotechnol, 2006. **24**(6): p. 667-72.

55. Farrow, L.A. and D. Edelson, *The steady-state assumption: fact or fiction?* Int. J. Chem. Kin., 1974. **V1**: p. 309-322.

56. Segel, L.A., *On the validity of the steady state assumption of enzyme kinetics.* Bull. Math. Biol., 1988. **50**: p. 579-593.

57. Flach, E.H. and S. Schnell, *Use and abuse of the quasi-steady-state approximation.* IEE Proc.-Syst. Biol., 2006. **153**(4): p. 187-191.

58. Gaudet, S., et al., *A compendium of signals and responses triggered by prodeath and prosurvival cytokines.* Mol Cell Proteomics, 2005. **4**(10): p. 1569-1590.

59. Janes, K.A., et al., *The response of human epithelial cells to TNF involves an inducible autocrine cascade.* Cell, 2006. **124**(6): p. 1225-39.

60. Sachs, K., et al., *Causal Protein-Signaling Networks Derived from Multiparameter Single-Cell Data.* Science, 2005. **308**(5721): p. 523-529.

61. Saez-Rodriguez, J., et al., *A logical model provides insights into T cell receptor signaling.* PLoS Comput Biol, 2007. **3**(8): p. e163.

62. Jaqaman, K. and G. Danuser, *Linking data to models: data regression.* Nat. Rev. Molec. Cell Biol., 2006. 7(11): p. 813-819.

63. Brown, K.S. and J.P. Sethna, *Statistical mechanical approaches to models with many poorly known parameters.* Phys Rev E Stat Nonlin Soft Matter Phys, 2003. **68**(2 Pt 1): p. 021904.

64. van Riel, N.A.W. and E.D. Sontag, *Parametric estimation in models combining signal transduction and metabolic pathways: the dependent input approach.* IEE Proc.-Syst. Biol., 2006. **153**(4): p. 263-274.

65. Conzelmann, H., et al., *A domain-oriented approach to the reduction of combinatorial complexity in signal transduction networks.* BMC Bioinformatics, 2006. 7: p. 34.

66. Blinov, M.L., et al., *A network model of early events in epidermal growth factor receptor signaling that accounts for combinatorial complexity.* Biosystems, 2006. **83**(2-3): p. 136-51.

67. Hlavacek, W.S., et al., *Rules for modeling signal-transduction systems.* Sci STKE, 2006. **2006**(344): p. re6.

68. Tyson, J.J., K.C. Chen, and B. Novak, *Sniffers, buzzers, toggles and blinkers: dynamics of regulatory and signaling pathways in the cell.* Curr Opin Cell Biol, 2003. **15**(2): p. 221-31.

69. Gardner, T.S., C.R. Cantor, and J.J. Collins, *Construction of a genetic toggle switch in Escherichia coli.* Nature, 2000. **403**(6767): p. 339-42.

70. von Dassow, G., et al., *The segment polarity network is a robust developmental module.* Nature, 2000. **406**(6792): p. 188-92.

71. Conrad, E.D. and J.J. Tyson, *Modeling Molecular Interaction Networks with Nonlinear Ordinary Differential Equations*, in *System Modeling in Cellular Biology*, Z. Szallasi, J. Stelling, and V. Periwal, Editors. 2006, MIT Press: Cambridge, Massachusetts. p. 97-123.

72. Balci, O. *Verification validation and accredidation of simulation models.* in *Proceedings of the 29th conference on Winter simulation.* 1997. Atlanta, Georgia, United States.

73. Sargent, R.G. *Verification and validation of simulation models.* in *2005 Proceedings of the Winter Simulation Conference.* 2005.

74. Geva-Zatorsky, N., et al., *Oscillations and variability in the p53 system.* Mol Syst Biol, 2006. **2**: p. 2006 0033.

75. Frey, D. and X. Li. *Evaluating Robust Design Methods Using a Model of Interactions in Complex Systems.* in *Engineering Systems 2004 Symposium.* 2004. Cambridge, MA.

76. Bentele, M., et al., *Mathematical modeling reveals threshold mechanism in CD95-induced apoptosis.* J Cell Biol, 2004. **166**(6): p. 839-51.

77. Aldridge, B.B., et al., *Direct Lyapunov exponent analysis enables parametric study of transient signalling governing cell behaviour.* Syst Biol (Stevenage), 2006. **153**(6): p. 425-432.

78. Moles, C.G., P. Mendes, and J.R. Banga, *Parameter estimation in biochemical pathways: a comparison of global optimization methods.* Genome Res, 2003. **13**(11): p. 2467-74.

79. Alon, U., *Biological Networks: The Tinkerer as an Engineer.* 2003, American Association for the Advancement of Science. p. 1866-1867.

80. Said, M.R., A.V. Oppenheim, and D.A. Lauffenburger, *Modeling cellular signal processing using interacting Markov chains.* Acoustics, Speech, and Signal Processing, 2003. Proceedings.(ICASSP'03). 2003 IEEE International Conference on, 2003. **6**.

81. Weng, G., U.S. Bhalla, and R. Iyengar, *Complexity in Biological Signaling Systems.* Science, 1999. **284**(5411): p. 92-96.

82. Price, N.D. and I. Shmulevich, *Biochemical and Statistical Network Models for Systems Biology.* Curr Opin Biotechnol., 2007. **18**(4): p. 365-370.

83. Li, P., et al., *Comparison of probabilistic Boolean network and dynamic Bayesian network approaches for inferring gene regulatory networks.* BMC Bioinformatics, 2007. **8 Suppl 7**: p. S13.

84. Albert, R. and H.G. Othmer, *The topology of the regulatory interactions predicts the expression pattern of the segment polarity genes in Drosophila melanogaster.* J Theor Biol, 2003. **223**(1): p. 1-18.

85. Chaves, M., R. Albert, and E.D. Sontag, *Robustness and fragility of Boolean models for genetic regulatory networks.* J Theor Biol, 2005. **235**(3): p. 431-49.

86. Huang, S. and D.E. Ingber, *Shape-dependent control of cell growth, differentiation, and apoptosis: switching between attractors in cell regulatory networks.* Exp Cell Res, 2000. **261**(1): p. 91-103.

87. Mendoza, L., D. Thieffry, and E.R. Alvarez-Buylla, *Genetic control of flower morphogenesis in Arabidopsis thaliana: a logical analysis.* Bioinformatics, 1999. **15**(7-8): p. 593-606.

88. Walsh, C.M., K.A. Luhrs, and A.F. Arechiga, *The "fuzzy logic" of the death-inducing signaling complex in lymphocytes.* J Clin Immunol, 2003. **23**(5): p. 333-53.

89. Zadeh, L.A., *Fuzzy logic = computing with words.* IEEE Transaction on Fuzzy Systems, 1996. **4**(3): p. 103-111.

90. Bosl, W.J., *Systems biology by the rules: hybrid intelligent systems for pathway modeling and discovery.* BMC Syst Biol, 2007. **1**: p. 13.

91. Sokhansanj, B.A., et al., *Linear fuzzy gene network models obtained from microarray data by exhaustive search.* BMC Bioinformatics, 2004. **5**: p. 108.

92. Du, P., et al., *Modeling gene expression networks using fuzzy logic.* IEEE Trans Syst Man Cybern B Cybern, 2005. **35**(6): p. 1351-9.

93. Sugeno, M. and T. Yasukawa, *A fuzzy-logic-based approach to qualitative modeling.* IEEE Transaction on Fuzzy Systems, 1993. **1**(1): p. 7-31.

94. Lassarre, C. and J.M. Ricort, *Growth factor-specific regulation of insulin receptor substrate-1 expression in MCF-7 breast carcinoma cells: effects on the insulin-like growth factor signaling pathway.* Endocrinology, 2003. **144**(11): p. 4811-9.

95. Moelling, K., et al., *Regulation of Raf-Akt Cross-talk.* J Biol Chem, 2002. **277**(34): p. 31099-106.

96. Yu, C.F., Z.X. Liu, and L.G. Cantley, *ERK negatively regulates the epidermal growth factor-mediated interaction of Gab1 and the phosphatidylinositol 3-kinase.* J Biol Chem, 2002. **277**(22): p. 19382-8.

97. Kiyatkin, A., et al., *Scaffolding protein Grb2-associated binder 1 sustains epidermal growth factor-induced mitogenic and survival signaling by multiple positive feedback loops.* J Biol Chem, 2006. **281**(29): p. 19925-38.

98. Lam, E.W., R.E. Francis, and M. Petkovic, *FOXO transcription factors: key regulators of cell fate.* Biochem Soc Trans, 2006. **34**(Pt 5): p. 722-6.

99. Ehlting, C., et al., *Regulation of suppressor of cytokine signaling 3 (SOCS3) mRNA stability by TNF-alpha involves activation of the MKK6/p38MAPK/MK2 cascade.* J Immunol, 2007. **178**(5): p. 2813-26.

100. Johansen, C., et al., *Protein expression of TNF-alpha in psoriatic skin is regulated at a posttranscriptional level by MAPK-activated protein kinase 2.* J Immunol, 2006. **176**(3): p. 1431-8.

101. Mahtani, K.R., et al., *Mitogen-activated protein kinase p38 controls the expression and posttranslational modification of tristetraprolin, a regulator of tumor necrosis factor alpha mRNA stability.* Mol Cell Biol, 2001. **21**(19): p. 6461-9.

102. Sousa, A.M., et al., *Smooth muscle alpha-actin expression and myofibroblast differentiation by TGFbeta are dependent upon MK2.* J Cell Biochem, 2007. **100**(6): p. 1581-92.

103. Kelliher, M.A., et al., *The death domain kinase RIP mediates the TNF-induced NF-kappaB signal.* Immunity, 1998. **8**(3): p. 297-303.

104. Karin, M., Y. Yamamoto, and Q.M. Wang, *The IKK NF-kappa B system: a treasure trove for drug development.* Nat Rev Drug Discov, 2004. **3**(1): p. 17-26.

105. Biswas, D.K., et al., *Epidermal growth factor-induced nuclear factor kappa B activation: A major pathway of cell-cycle progression in estrogen-receptor negative breast cancer cells.* Proc Natl Acad Sci U S A, 2000. **97**(15): p. 8542-7.

106. Sorkin, A. and M. von Zastrow, *Signal transduction and endocytosis: close encounters of many kinds.* Nature Reviews Molecular Cell Biology, 2002. **3**: p. 600-614.

107. Vieira, A.V., C. Lamaze, and S.L. Schmid, *Control of EGF receptor signaling by clathrin-mediated endocytosis.* Science, 1996. **274**(5295): p. 2086-9.

108. Linden, R. and A. Bhaya, *Evolving fuzzy rules to model gene expression.* Biosystems, 2007. **88**(1-2): p. 76-91.

109. Ressom, H., R. Reynolds, and R.S. Varghese, *Increasing the efficiency of fuzzy logic-based gene expression data analysis.* Physiol Genomics, 2003. **13**(2): p. 107-17.

110. Kholodenko, B.N., et al., *Quantification of short term signaling by the epidermal growth factor receptor.* J Biol Chem, 1999. **274**(42): p. 30169-81.

111. Bhalla, U.S. and R. Iyengar, *Functional modules in biological signalling networks.* Novartis Found Symp, 2001. **239**: p. 4-13; discussion 13-5, 45-51.

112. Schoeberl, B., Gaudet, S., Albeck, J., Lauffenburger, D., Sorger, P. *A computational model if the TNF signaling netowrk can classify cells based on their kinetics of caspase activation.* in *International Conference on Systems Biology.* 2002. Stokholm, Sweden.

113. Novak, B. and J.J. Tyson, *Modelling the controls of the eukaryotic cell cycle.* Biochem Soc Trans, 2003. **31**(Pt 6): p. 1526-9.

114. Bhalla, U.S., *Models of cell signaling pathways.* Curr Opin Genet Dev, 2004. **14**(4): p. 375-81.

115. Nelson, D.E., et al., *Oscillations in NF-{kappa}B Signaling Control the Dynamics of Gene Expression.* Science, 2004. **306**(5696): p. 704-708.

116. Davidson, E.H., et al., *A provisional regulatory gene network for specification of endomesoderm in the sea urchin embryo.* Dev Biol, 2002. **246**(1): p. 162-90.

117. Kitano, H., *Systems biology: a brief overview.* Science, 2002. **295**(5560): p. 1662-4.

118. Hornberg, J.J., et al., *Control of MAPK signalling: from complexity to what really matters.* Oncogene, 2005. **24**(36): p. 5533-42.

119. Thattai, M. and A. van Oudenaarden, *Attenuation of noise in ultrasensitive signaling cascades.* Biophys J, 2002. **82**(6): p. 2943-50.

120. Rosenfeld, N., et al., *Gene regulation at the single-cell level.* Science, 2005. **307**(5717): p. 1962-5.

121. Lidstrom, M.E. and D.R. Meldrum, *Life-on-a-chip.* Nat Rev Microbiol, 2003. **1**(2): p. 158-64.

122. Chong, H., H.G. Vikis, and K.L. Guan, *Mechanisms of regulating the Raf kinase family.* Cell Signal, 2003. **15**(5): p. 463-9.

123. Resat, H., et al., *An integrated model of epidermal growth factor receptor trafficking and signal transduction.* Biophys J, 2003. **85**(2): p. 730-43.

124. Hatakeyama, M., et al., *A computational model on the modulation of mitogen-activated protein kinase (MAPK) and Akt pathways in heregulin-induced ErbB signalling.* Biochem J, 2003. **373**(Pt 2): p. 451-63.

125. Hua, F., et al., *Effects of Bcl-2 levels on Fas signaling-induced caspase-3 activation: molecular genetic tests of computational model predictions.* J Immunol, 2005. **175**(2): p. 985-995.

126. Sasagawa, S., et al., *Prediction and validation of the distinct dynamics of transient and sustained ERK activation.* Nat Cell Biol, 2005. **7**(4): p. 365-73.

127. Asthagiri, A.R. and D.A. Lauffenburger, *Bioengineering models of cell signaling.* Annu Rev Biomed Eng, 2000. **2**: p. 31-53.

128. Swameye, I., et al., *Identification of nucleocytoplasmic cycling as a remote sensor in cellular signaling by databased modeling.* Proc Natl Acad Sci U S A, 2003. **100**(3): p. 1028-33.

129. Mendes, P. and D. Kell, *Non-linear optimization of biochemical pathways: applications to metabolic engineering and parameter estimation.* Bioinformatics, 1998. **14**(10): p. 869-83.

130. Tyson, J.J., A. Csikasz-Nagy, and B. Novak, *The dynamics of cell cycle regulation.* Bioessays, 2002. **24**(12): p. 1095-109.

131. Pomerening, J.R., S.Y. Kim, and J.E. Ferrell, Jr., *Systems-level dissection of the cell-cycle oscillator: bypassing positive feedback produces damped oscillations.* Cell, 2005. **122**(4): p. 565-78.

132. Eissing, T., et al., *Bistability analyses of a caspase activation model for receptor-induced apoptosis.* J Biol Chem, 2004. **279**(35): p. 36892-7.

133. Bagci, E.Z., et al., *Bistability in Apoptosis: Roles of Bax, Bcl-2 and Mitochondrial Permeability Transition Pores.* Biophys J, 2005.

134. Suzuki, Y., et al., *X-linked inhibitor of apoptosis protein (XIAP) inhibits caspase-3 and -7 in distinct modes.* J Biol Chem, 2001. **276**(29): p. 27058-63.

135. Haller, G., *Distinguished material surfaces and coherent structures in three-dimensional fluid flows.* Physica D, 2001. **149**(4): p. 248-277.

136. Haller, G., *Lagrangian coherent structures from approximate velocity data.* Physics of Fluids, 2002. **14**(6): p. 1851-1861.

137. Wang, Y., et al., *Closed-loop Lagrangian separation control in a bluff body shear flow model.* Physics of Fluids, 2003. **15**(8): p. 2251-2266.

138. El Rifai, K., Bajaj, A. K., Haller, G., *Global dynamics of an autoparametric spring-mass-pendulum system and rigid body dynamics.* submitted to Nonlinear Dynamics, 2005.

139. Barnhart, B.C., E.C. Alappat, and M.E. Peter, *The CD95 type I/type II model.* Semin Immunol, 2003. **15**(3): p. 185-93.

140. Schimmer, A.D., et al., *Identification of small molecules that sensitize resistant tumor cells to tumor necrosis factor-family death receptors.* Cancer Res, 2006. **66**(4): p. 2367-75.

141. Algeciras-Schimnich, A., et al., *Two CD95 tumor classes with different sensitivities to antitumor drugs.* Proc Natl Acad Sci U S A, 2003. **100**(20): p. 11445-50.

142. Albeck, J.G., et al., *Quantitative analysis of pathways controlling extrinsic apoptosis in single cells.* Mol Cell, 2008. **30**(1): p. 11-25.

143. Albeck, J.G., et al., *Modeling a snap-action, variable-delay switch controlling extrinsic cell death.* PLoS Biol, Submitted.

144. Tawa, P., et al., *Catalytic activity of caspase-3 is required for its degradation: stabilization of the active complex by synthetic inhibitors.* Cell Death Differ, 2004. **11**(4): p. 439-47.

145. Barnhart, B.C., et al., *CD95 apoptosis resistance in certain cells can be overcome by noncanonical activation of caspase-8.* Cell Death Differ, 2005. **12**(1): p. 25-37.

146. Harlin, H., et al., *Characterization of XIAP-deficient mice.* Mol Cell Biol, 2001. **21**(10): p. 3604-8.

147. Okada, H., et al., *Generation and characterization of Smac/DIABLO-deficient mice.* Mol Cell Biol, 2002. **22**(10): p. 3509-17.

148. Wilkinson, J.C., et al., *Upstream regulatory role for XIAP in receptor-mediated apoptosis.* Mol Cell Biol, 2004. **24**(16): p. 7003-14.

149. Schimmer, A.D., et al., *Small-molecule antagonists of apoptosis suppressor XIAP exhibit broad antitumor activity.* Cancer Cell, 2004. **5**(1): p. 25-35.

150. Li, L., et al., *A small molecule Smac mimic potentiates TRAIL- and TNFalpha-mediated cell death.* Science, 2004. **305**(5689): p. 1471-4.

151. Li, S., et al., *Relief of extrinsic pathway inhibition by the Bid-dependent mitochondrial release of Smac in Fas-mediated hepatocyte apoptosis.* J Biol Chem, 2002. **277**(30): p. 26912-20.

152. Bank, A., et al., *SMAC mimetics sensitize nonsteroidal anti-inflammatory drug-induced apoptosis by promoting caspase-3-mediated cytochrome c release.* Cancer Res, 2008. **68**(1): p. 276-84.

153. Wang, S. and W.S. El-Deiry, *TRAIL and apoptosis induction by TNF-family death receptors.* Oncogene, 2003. **22**(53): p. 8628-33.

154. Kohli, M., et al., *Facile methods for generating human somatic cell gene knockouts using recombinant adeno-associated viruses.* Nucleic Acids Res, 2004. **32**(1): p. e3.

155. Carter, B.Z., et al., *Small-molecule XIAP inhibitors derepress downstream effector caspases and induce apoptosis of acute myeloid leukemia cells.* Blood, 2005. **105**(10): p. 4043-50.

156. Cummins, J.M., et al., *X-linked inhibitor of apoptosis protein (XIAP) is a nonredundant modulator of tumor necrosis factor-related apoptosis-inducing ligand (TRAIL)-mediated apoptosis in human cancer cells.* Cancer Res, 2004. **64**(9): p. 3006-8.

157. Yang, Y., et al., *Ubiquitin protein ligase activity of IAPs and their degradation in proteasomes in response to apoptotic stimuli.* Science, 2000. **288**(5467): p. 874-7.

158. Harrington, L.S., G.M. Findlay, and R.F. Lamb, *Restraining PI3K: mTOR signalling goes back to the membrane.* Trends Biochem Sci, 2005. **30**(1): p. 35-42.

159. Paz, K., et al., *A molecular basis for insulin resistance. Elevated serine/threonine phosphorylation of IRS-1 and IRS-2 inhibits their binding to the juxtamembrane region of the insulin receptor and impairs their ability to undergo insulin-induced tyrosine phosphorylation.* J Biol Chem, 1997. **272**(47): p. 29911-8.

160. DiPietrantonio, A.M., et al., *Fenretinide-induced caspase 3 activity involves increased protein stability in a mechanism distinct from reactive oxygen species elevation.* Cancer Res, 2000. **60**(16): p. 4331-5.

161. Tyas, L., et al., *Rapid caspase-3 activation during apoptosis revealed using fluorescence-resonance energy transfer.* EMBO Rep, 2000. **1**(3): p. 266-70.

162. Rehm, M., et al., *Single-cell fluorescence resonance energy transfer analysis demonstrates that caspase activation during apoptosis is a rapid process. Role of caspase-3.* J Biol Chem, 2002. **277**(27): p. 24506-14.

163. Stennicke, H.R., et al., *Internally quenched fluorescent peptide substrates disclose the subsite preferences of human caspases 1, 3, 6, 7 and 8.* Biochem J, 2000. **350 Pt 2**: p. 563-8.

164. Luo, K.Q., et al., *Measuring dynamics of caspase-8 activation in a single living HeLa cell during TNFalpha-induced apoptosis.* Biochem Biophys Res Commun, 2003. **304**(2): p. 217-22.

165. Thornberry, N.A., et al., *A combinatorial approach defines specificities of members of the caspase family and granzyme B. Functional relationships established for key mediators of apoptosis.* J Biol Chem, 1997. **272**(29): p. 17907-11.

166. Du, C., et al., *Smac, a mitochondrial protein that promotes cytochrome c-dependent caspase activation by eliminating IAP inhibition.* Cell, 2000. **102**(1): p. 33-42.

167. Munoz-Pinedo, C., et al., *Different mitochondrial intermembrane space proteins are released during apoptosis in a manner that is coordinately initiated but can vary in duration.* Proc Natl Acad Sci U S A, 2006. **103**(31): p. 11573-8.

168. Rehm, M., H. Dussmann, and J.H. Prehn, *Real-time single cell analysis of Smac/DIABLO release during apoptosis.* J Cell Biol, 2003. **162**(6): p. 1031-43.

169. Karbowski, M., et al., *Quantitation of mitochondrial dynamics by photolabeling of individual organelles shows that mitochondrial fusion is blocked during the Bax activation phase of apoptosis.* J Cell Biol, 2004. **164**(4): p. 493-9.

170. Kawai, H., et al., *Simultaneous real-time detection of initiator- and effector-caspase activation by double fluorescence resonance energy transfer analysis.* J Pharmacol Sci, 2005. **97**(3): p. 361-8.

171. Kawai, H., et al., *Simultaneous imaging of initiator/effector caspase activity and mitochondrial membrane potential during cell death in living HeLa cells.* Biochim Biophys Acta, 2004. **1693**(2): p. 101-10.

172. Huang, Y., et al., *Structural basis of caspase inhibition by XIAP: differential roles of the linker versus the BIR domain.* Cell, 2001. **104**(5): p. 781-90.

173. Rehm, M., et al., *Systems analysis of effector caspase activation and its control by X-linked inhibitor of apoptosis protein.* Embo J, 2006. **25**(18): p. 4338-49.

174. Rosado, J.A., et al., *Early caspase-3 activation independent of apoptosis is required for cellular function.* J Cell Physiol, 2006. **209**(1): p. 142-52.

175. Draviam, V.M., et al., *Misorientation and reduced stretching of aligned sister kinetochores promote chromosome missegregation in EB1- or APC-depleted cells.* Embo J, 2006. **25**(12): p. 2814-27.

176. Kapoor, T.M., *Chromosome segregation: correcting improper attachment.* Curr Biol, 2004. **14**(23): p. R1011-3.

177. Musacchio, A. and K.G. Hardwick, *The spindle checkpoint: structural insights into dynamic signalling.* Nat Rev Mol Cell Biol, 2002. **3**(10): p. 731-41.

178. Howard, J. and A.A. Hyman, *Dynamics and mechanics of the microtubule plus end.* Nature, 2003. **422**(6933): p. 753-8.

179. Lengauer, C., K.W. Kinzler, and B. Vogelstein, *Genetic instability in colorectal cancers.* Nature, 1997. **386**(6625): p. 623-7.

180. Spencer, F., et al., *Mitotic chromosome transmission fidelity mutants in Saccharomyces cerevisiae.* Genetics, 1990. **124**(2): p. 237-49.

181. Draviam, V.M., S. Xie, and P.K. Sorger, *Chromosome segregation and genomic stability.* Curr Opin Genet Dev, 2004. **14**(2): p. 120-5.

182. Cahill, D.P., et al., *Mutations of mitotic checkpoint genes in human cancers.* Nature, 1998. **392**(6673): p. 300-3.

183. Yamaguchi, K., et al., *Mutation analysis of hBUB1 in aneuploid HNSCC and lung cancer cell lines.* Cancer Lett, 1999. **139**(2): p. 183-7.

184. Meraldi, P., V.M. Draviam, and P.K. Sorger, *Timing and checkpoints in the regulation of mitotic progression.* Dev Cell, 2004. 7(1): p. 45-60.

185. Gergely, F., V.M. Draviam, and J.W. Raff, *The ch-TOG/XMAP215 protein is essential for spindle pole organization in human somatic cells.* Genes Dev, 2003. **17**(3): p. 336-41.

186. Rieder, C.L. and H. Maiato, *Stuck in division or passing through: what happens when cells cannot satisfy the spindle assembly checkpoint.* Dev Cell, 2004. 7(5): p. 637-51.

187. Akhmanova, A. and C.C. Hoogenraad, *Microtubule plus-end-tracking proteins: mechanisms and functions.* Curr Opin Cell Biol, 2005. **17**(1): p. 47-54.

188. Dujardin, D., et al., *Evidence for a role of CLIP-170 in the establishment of metaphase chromosome alignment.* J Cell Biol, 1998. **141**(4): p. 849-62.

189. Faulkner, N.E., et al., *A role for the lissencephaly gene LIS1 in mitosis and cytoplasmic dynein function.* Nat Cell Biol, 2000. **2**(11): p. 784-91.

190. Tirnauer, J.S., et al., *EB1 targets to kinetochores with attached, polymerizing microtubules.* Mol Biol Cell, 2002. **13**(12): p. 4308-16.

191. Fodde, R., et al., *Mutations in the APC tumour suppressor gene cause chromosomal instability.* Nat Cell Biol, 2001. **3**(4): p. 433-8.

192. Kaplan, K.B., et al., *A role for the Adenomatous Polyposis Coli protein in chromosome segregation.* Nat Cell Biol, 2001. **3**(4): p. 429-32.

193. Maiato, H., et al., *Human CLASP1 is an outer kinetochore component that regulates spindle microtubule dynamics.* Cell, 2003. **113**(7): p. 891-904.

194. Maiato, H., A. Khodjakov, and C.L. Rieder, *Drosophila CLASP is required for the incorporation of microtubule subunits into fluxing kinetochore fibres.* Nat Cell Biol, 2005. 7(1): p. 42-7.

195. Maiato, H., C.L. Rieder, and A. Khodjakov, *Kinetochore-driven formation of kinetochore fibers contributes to spindle assembly during animal mitosis.* J Cell Biol, 2004. **167**(5): p. 831-40.

196. Tanenbaum, M.E., et al., *CLIP-170 facilitates the formation of kinetochore-microtubule attachments.* Embo J, 2006. **25**(1): p. 45-57.

197. Echeverri, C.J., et al., *Molecular characterization of the 50-kD subunit of dynactin reveals function for the complex in chromosome alignment and spindle organization during mitosis.* J Cell Biol, 1996. **132**(4): p. 617-33.

198. Howell, B.J., et al., *Cytoplasmic dynein/dynactin drives kinetochore protein transport to the spindle poles and has a role in mitotic spindle checkpoint inactivation.* J Cell Biol, 2001. **155**(7): p. 1159-72.

199. Rogers, S.L., et al., *Drosophila EB1 is important for proper assembly, dynamics, and positioning of the mitotic spindle.* J Cell Biol, 2002. **158**(5): p. 873-84.

200. Green, R.A., R. Wollman, and K.B. Kaplan, *APC and EB1 function together in mitosis to regulate spindle dynamics and chromosome alignment.* Mol Biol Cell, 2005. **16**(10): p. 4609-22.

201. Alter, O., P.O. Brown, and D. Botstein, *Singular value decomposition for genome-wide expression data processing and modeling.* Proc Natl Acad Sci U S A, 2000. **97**(18): p. 10101-6.